Review article

Controls on the intrinsic flow properties of mudrock fractures: A review of their importance in subsurface storage

Tomos Phillips[a,c,*], Niko Kampman[b], Kevin Bisdom[b], Nathaniel D. Forbes Inskip[a], Sabine A.M. den Hartog[a], Veerle Cnudde[c,d], Andreas Busch[a]

[a] *Institute of GeoEnergy Engineering, The Lyell Centre, Heriot-Watt University, Edinburgh, UK*
[b] *Shell Global Solutions International B.V., Grasweg 31, 1031 HW Amsterdam, The Netherlands*
[c] *Department of Geology, PProGRess/UGCT, Ghent University, Belgium*
[d] *Department of Earth Sciences, Utrecht University, Princetonlaan 8a, 3584, CB, Utrecht, The Netherlands*

ARTICLE INFO

ABSTRACT

Effective storage and containment of injected fluids, over a range of spatial and temporal scales, is reliant upon the sealing capacity of the lithologies overlying geological stores. Low-permeability mudrocks are considered effective candidates to restrict the migration of injected fluids from the host formation, owing to their low matrix permeabilities ($< 10^{-19}$ m^2). Fluid-conductive fault and fracture systems can threaten seal integrity by creating high permeability pathways ($> 10^{-19}$ m^2), potentially compromising subsurface storage operations. To safeguard and expedite the initialisation of storage projects on an impactful scale, rigorous comprehension of the intrinsic flow properties of fractures in mudrocks is key. The distribution of fractures within fracture networks, and the degree to which these configurations promote interconnectivity, is a primary factor influencing fluid transport. At the individual fracture scale, a fractures ability to transmit fluid is a function of the aperture distribution, which is itself governed by a series of hierarchical controls operating across various scales. Accurate understanding, characterisation and quantification of the physical transport mechanisms and fluid flow dynamics prevalent in rock fractures is frustrated by the existence of heterogeneous aperture distribution, caused by fracture surface roughness. Further hindrances to understanding the fundamental transport properties of fractures stem from our limited knowledge of the breadth and complexity of hydromechanical responses that emerge from the coupling of pore pressure, effective stress and multiphase flow. In this review paper, we have collated and analysed the large body of experimental and theoretical literature pertaining to single- and two-phase fluid transport, and the geomechanical properties of single fractures and fracture networks in relation to fluid conductivity. We focus upon naturally occurring fractures in mudrocks and the current understanding of the physical and transport properties which impact the risks to secure containment in geological reservoirs.

1. Introduction

The progress of climate change necessitates a transition to a low-carbon economy (IPCC, 2014). Such an economy requires a diversified energy production infrastructure comprising renewable sources (e.g. wind, wave and solar), nuclear power, geothermal for heat and power and the replacement of carbon-intensive fuels (e.g. coal and oil) with lower carbon intensity natural gas coupled with carbon capture and geological storage (IPCC, 2014). Extraction of hydrocarbons or geothermal energy resources from the Earth's subsurface, or the storage of anthropogenic waste, such as carbon dioxide (CO_2) or nuclear materials, requires a rigorous understanding of the performance and integrity of these geological reservoirs over a period of years to millennia. Successful carbon storage projects, for example, require that the stored CO_2 is retained in the subsurface for millennial timescales to mitigate the impacts of global warming (Metz et al., 2005). The intermittent nature of renewable power sources requires either the temporary storage of energy or conversion of this energy into stable fuels (e.g. H_2 or CH_4) (Bauer et al., 2017). This energy may be stored temporarily in the subsurface in the form of compressed air or as these fuel products (Kabuth et al., 2017; McCartney et al., 2016). Successful energy or CO_2 storage requires the efficient use of storage capacity across a range of spatial and temporal scales, well-characterised geological reservoirs and adherence to regulatory and public acceptance criteria
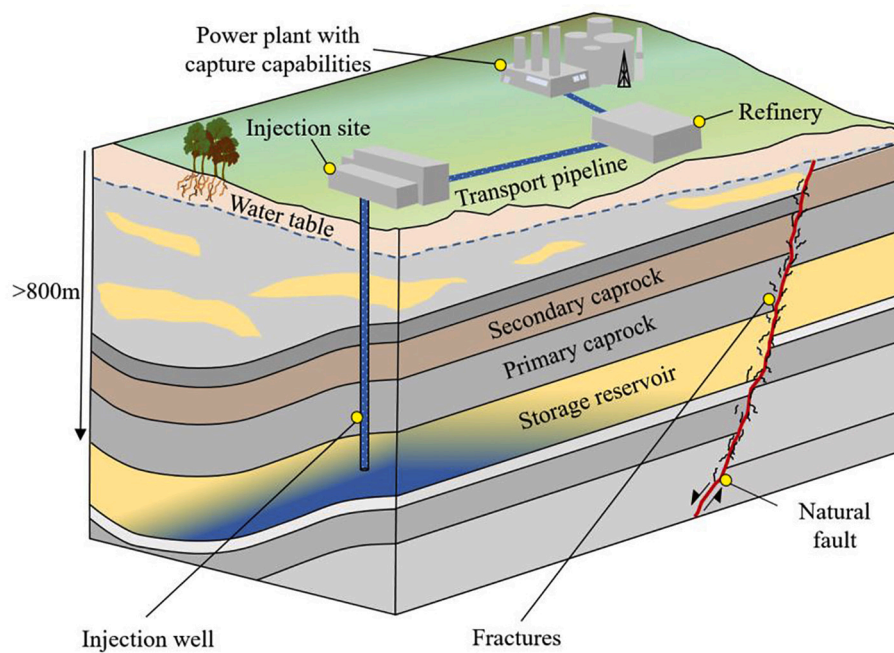
Fig. 1. Diagrammatic illustration of geological CO_2/energy storage into a deep (> 800 m) storage reservoir, overlain by a low-permeability caprock (e.g. mudrock). Vertical migration/leakage from the host formation is dependent upon the sealing integrity of the overlying strata. The presence of naturally occurring faulting (large-scale) and associated fracturing (micro-, macro- & meso-scale) must be risk assessed to identify realistic leakage geometries and determine the storage viability of a particular system.

(Luo et al., 2015; Stewart and Lewis, 2017).

The viability of current and future energy extraction and waste or energy storage projects relies not only upon fluid transport efficiency within geological formations but also on the ability of these formations to effectively contain fluids over stipulated timescales (Busch and Kampman, 2018). Geological caprocks form the principal sealing system and ultimately dictate the efficacy of subsurface storage projects. Prediction of caprock integrity requires a comprehensive understanding of the geomechanical and geochemical properties of these rocks (Bildstein et al., 2010), where fluid-conductive fault and fracture systems represent the primary threat to caprock integrity.

Effective caprocks comprise undisturbed, low-permeability, thick, and laterally extensive formations (Amann-Hildenbrand et al., 2013), with high capillary entry or breakthrough pressures to prevent leakage of injected fluids (Fig. 1) (Ingram and Urai, 1999; Wollenweber et al., 2009). Furthermore, for the storage process to be successful, caprocks must withstand short-term excess injection and long-term buoyancy-driven pressures (Espinoza and Santamarina, 2017). In principle, any low-permeability rock may act as a caprock, with evaporites (e.g. halite and anhydrite) and mudrocks representing the most prolific lithologies securing geological stores (Busch and Amann-Hildenbrand, 2013). Mudrocks comprise very-fine-grained clastic sediments, including shales, siltstones, mudstones, claystones and argillites, forming approximately 65% of the sedimentary record worldwide (Garrels and Mackenzie, 1969). Their effectiveness as caprocks stems from their low matrix permeabilities ($< 10^{-19}$ m^2) resulting from largely disconnected nano-pores that constitute a majority percentage of the cumulative porosity (Amann-Hildenbrand et al., 2012; Hu et al., 2012; Mehmani et al., 2013; Ross and Bustin, 2009). Sealing efficiency is a product of burial history, mechanical compaction and diagenesis, including mineral dehydration, dissolution and precipitation, which all modify porosity and pore structure (Nygard et al., 2004).

Faults and fracture systems represent a significant threat to seal integrity, as they form potentially permeable conduits through which fluids can escape (Barton et al., 1995; Bond et al., 2013; Faulkner et al., 2010; Ferrill and Morris, 2003; Sibson, 1996; Sibson, 1998). These include naturally occurring faults and fractures arising from tectonic deformation, uplift and unloading, and induced fractures resulting from extraction or injection of fluids (e.g. hydraulic fractures) (Bond et al., 2013). Conversely, some faults and fractures may decrease permeability through structural and/or diagenetic processes, producing baffles or barriers, which compartmentalise reservoirs and reduce production or storage volumes (Laubach, 2003; McGinnis et al., 2017). Even in highly permeable ($> 10^{-10}$ m^2) fracture systems the nature of fluid flow is complex, with localised anisotropic flow properties arising from heterogeneities in fracture mode, surface roughness, and effective stress, leading to heterogeneous fluid displacement (Oh et al., 2013). Understanding the distribution and architecture of these geological features, and their transport, geomechanical, and geochemical properties, is critical for accurate assessments of storage security.

In this review, we collate and analyse the large body of experimental and theoretical literature pertaining to single- and two-phase fluid transport, and the geomechanical properties of single fractures and fracture networks. We discuss the various fracture attributes and how their occurrence and severity impact the intrinsic flow properties of a fracture, to ultimately create a high-level point of reference for others by highlighting fundamental considerations and open research questions surrounding fracture transport phenomena. Our primary focus is on naturally occurring faults and fractures in mudrocks, how these features are traditionally modelled and the governing equations which describe fluid transport, and the current understanding of the physical and transport properties which impact the risks to storage containment in geological reservoirs.

To accomplish this, we review the current understanding of the controls on natural fracture formation; the influence of individual fracture properties on fluid transport; the nature of fracture networks, their scaling relationships and controls on fluid flow, and finally hydromechanical coupling in fault-fracture systems. Additionally, we briefly summarise the current state of knowledge pertaining to multiphase flow phenomena in rough fractures, which are a principal control on fluid leakage rates. Based on the amassed literature, open research questions are identified, and future research directions are suggested. In this review, we do not discuss fractures induced by fluid extraction or injection, their associated seismicity (Davies et al., 2013; Grigoli et al., 2017), or their role in unconventional gas extraction/enhanced oil recovery (Jackson et al., 2013) and enhanced geothermal systems (Olasolo et al., 2016). We briefly summarise the role of chemical diagenetic effects on fracture systems, however, for a comprehensive review, see Laubach et al. (2019).
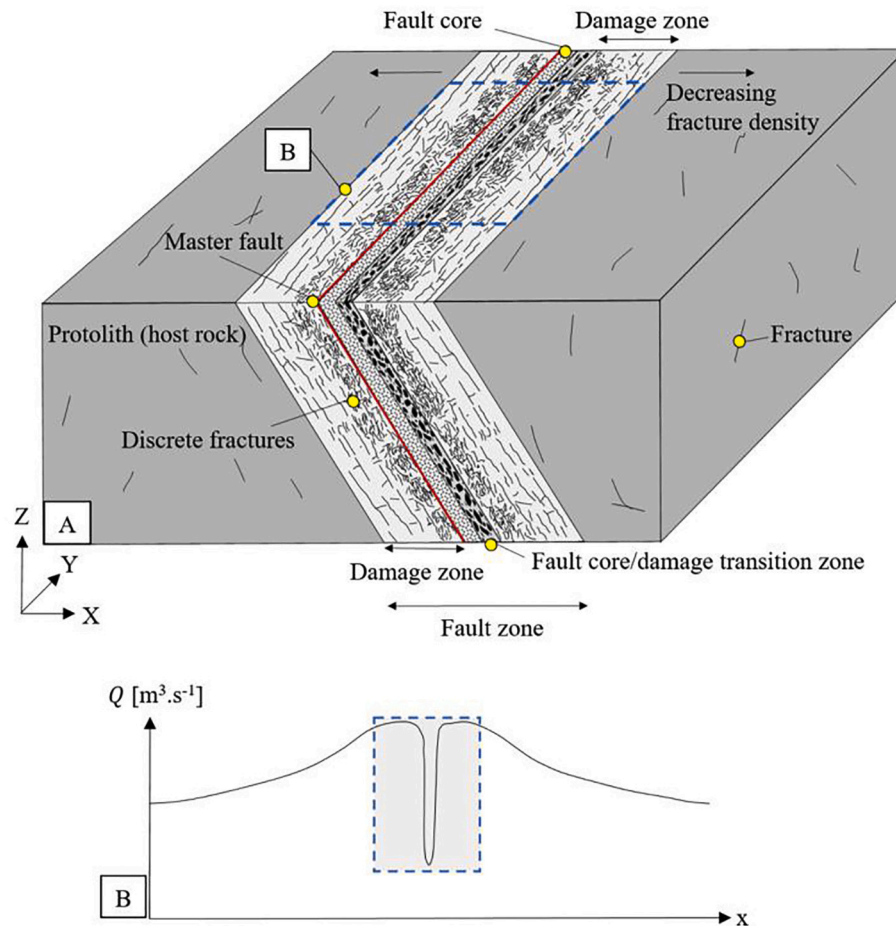
Fig. 2. (A) Schematic geological representation of a typical fault damage zone (FDZ) in a mudrock formation, comprising a master fault with an associated low-permeability (fine-grained) fault core, a transition zone where permeability appears highest and a gradually decreasing fracture density with increasing distance from the fault core. (B) Generalised conceptual diagram of the area highlighted in A (blue dashed region), denoting the order of magnitude differences in hydraulic transmissivity (*Q*) along the entire fault zone (redrawn after Cappa and Rutqvist (2011)).

## 2. Structural settings of natural fractures and their genesis

2.1. Importance of natural fractures for fluid conductivity

Large permeability contrasts between faults/fractures and rock matrix make them a critical feature governing mass and heat transport, and the production and storage performance of geological reservoirs. Despite their critical importance, understanding and predicting fluid flow rates through these naturally occurring features, at a variety of scales, remains challenging (Faulkner et al., 2010; Yang et al., 2019a). Difficulties in predicting fluid flow through such features arise from the complexity of faults and fracture networks, our limited understanding of the fundamental controls on their intrinsic permeabilities, and the coupling of multiphase flow as well as geomechanical and geochemical phenomena which modify permeability (Kishida et al., 2013; Wang et al., 2016). For example, the coupling of flow, pore pressure, and effective stress leads to complex hydromechanical responses in fractured media, and a strong back coupling on fluid flow rates (Baghbanan and Jing, 2008; Edwards et al., 2017). Effective stress ($\sigma' = \sigma - P_p$), describing the total applied stress (σ) minus the pore pressure (P_p), exerts a strong influence over the aperture of a single fracture and thus the permeability (Faulkner et al., 2010). The conductivity of individual fractures, their frequency and connectivity ultimately determine the intrinsic permeability of the fracture network (Jolley and London, 2007). Injection or production of fluids from geological reservoirs commonly give rise to multiphase immiscible fluid systems (e.g. water-gas or water-oil), and the strong phase interference that accompanies two-phase flow through fractures reduces phase permeability and leakage rates, influencing, for example, the risks associated with CO_2 or energy storage.

The majority of rocks exhibit fractures at some scale, varying over approximately ten orders of magnitude (millimetre- to kilometre-scale) (Bonnet et al., 2001). Fracture networks may occur as pervasive regional rock deformation, primarily resulting from large-scale folding, bending or uplift, or as localised features associated with (large-scale) shear and fault zones (Gale et al., 2014). Regionally diffuse fractures typically display homogeneous geometrical configurations, however subtle differences in mechanical stratigraphy can result in fracture patterns that vary drastically from layer to layer in regional fracture systems (Boersma et al., 2020; Douma et al., 2019; Forbes Inskip et al., 2020; Gale et al., 2014). Mechanical rock properties also evolve through geological time in response to burial and diagenetic processes, which can also influence fracture pattern development (Laubach et al., 2009). Pervasive fracturing of mudrocks may occur as a result of hydraulic fracturing during burial and uplift, especially in overpressured sedimentary basins, often linked to seal failure and secondary hydrocarbon migration (Engelder, 1985; King Hubbert and Rubey, 1959; Mandl and Harkness, 1987; Roberts and Nunn, 1995). However, identifying which loading path or paths are responsible for a given fracture pattern is challenging (English and Laubach, 2017; Virgo et al., 2014), with an outline of these difficulties and some recent solutions discussed in Laubach et al. (2019). It is the case that mudrocks display somewhat distinctive fracture mechanisms from other rock types (e.g. sandstones, carbonates), for example, mudrocks commonly exhibit layer-parallel
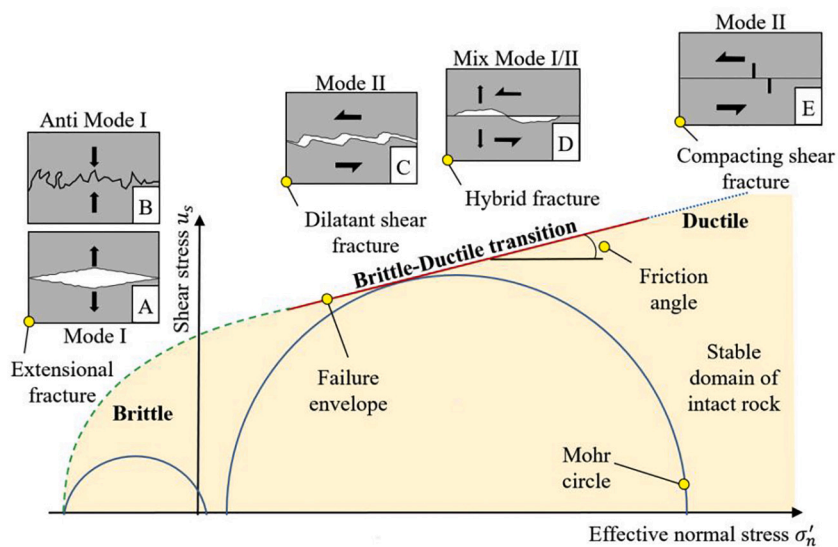
Fig. 3. Simplified Mohr-Coulomb failure criterion diagram illustrating brittle to ductile failure (modified after Ingram and Urai (1997) and Nygard et al. (2006)). Shaded region denotes the stable domain of intact rock, where breaching of the failure envelope shown leads to failure and fracture initiation. Brittle failure is observed at intermediate compressive confining stresses while increasing confinement leads to more ductile deformation. (A) Mode I (tensile opening). (B) Anti Mode I stylolites representing dissolution surfaces perpendicular to opening-mode fractures. (C) Mode II (shear failure with aperture dilatancy). (D) Mix Mode I/II. (E) Mode II shear fracture showing appreciable shear without aperture dilation as a result of deformation occurring at high confining pressures.

fractures (see the review by Hooker et al., 2019). Mudrock-hosted fracturing has been shown to be as much the result of diagenesis as to tectonically-induced stresses (Hooker et al., 2017; Laubach et al., 2019). In the case of folding, mudrocks, for example, can fold via flexural (layer-parallel) slip, meaning fracture formation will be concentrated on the limbs of the folds corresponding to the areas of maximum strain (Cosgrove, 2015). Other fold-related fracture configurations in mudrocks have been reported and as a result can have different impacts on fluid flow properties (Cosgrove, 2015; Evans et al., 2012; Hansberry et al., 2014).

The (permeability) structure of faults is a complex function of lithology, tectonic environment (e.g. strike-slip, extension or compression), fault displacement, fluid flow and fluid-rock reaction history (Faulkner et al., 2010). If conductive, large-scale faults present substantial leakage risks as they have the potential to cross-cut several formations (Fig. 1). Faults typically comprise a fault core, where strain is localised forming a gouge, cataclastite or ultracataclastite (or a combination of these), surrounded by a zone of fractures and faulting, distributed over a wide range of length scales, forming a fault damage zone (FDZ; Fig. 2a) (Caine et al., 1996; Faulkner et al., 2010). In mudrocks, fault gouge, where present, typically creates impermeable or low-permeability fault core, with permeability enhancement confined to the surrounding zone of fractures (Fig. 2b). Fault-related fractures may form simple regular geometries (sub)parallel to the fault core or more complex network geometries comprising anastomosing fracture surfaces (Johri et al., 2014; Kim et al., 2004). The damage zones may be tip-, linking- or wall-damage zones, based upon position within and around a fault, with the most intense deformation, commonly being located towards the fault tips and linkages (Kim et al., 2004; Kirkpatrick et al., 2008). The fractures may be permeability-enhancing slip surfaces or permeability impeding deformation bands (Lunn et al., 2008). Fracture network permeability is governed by a complex interplay of fracture permeability, connectivity and stress conditions (Caine et al., 1996; Evans et al., 1997; Nygard et al., 2006). Whether a fracture network displays irregular or homogeneously spaced fractures is influenced by a mixture of failure mode (Anderson, 2005; Aydin et al., 2006), mechanical stratigraphy (Hooker et al., 2013), varying growth processes and rates (Alzayer et al., 2015; Atkinson, 1984), loading conditions (Engelder, 1985), scale (Bonnet et al., 2001) and interplay with simultaneous or subsequent geochemical processes (Hooker et al., 2012; Olson et al., 2009). Fractures within the vicinity of large-scale faults exhibit variable properties over small distances (De Joussineau and Aydin, 2007; Faulkner et al., 2010), and scaling relationships between FDZ thickness, lithology, failure mode, and fault throw are key

aspects of characterising fault zone permeability (Faulkner et al., 2010; Shipton et al., 2006). Comprehensive reviews of fracture spacing relationships and FDZ permeability evolution are provided by Billi et al. (2003), Cappa and Rutqvist (2011), Nussbaum et al. (2011) and McGinnis et al. (2017).

What follows is a review of the different parameters that exert an influence on the fluid transport properties of fractures. We begin by discussing the origin of fractures and the effect this has on the initial aperture of a fracture while describing how different fracture attributes scale in nature. We then narrow the focus and detail the importance of hierarchical features that influence fracture transport properties.

2.2. Origin of natural fractures

Natural fractures arise from the partial loss of cohesion around flaws and heterogeneities in response to stress conditions. The stress conditions, fluid pressures, and mechanical properties of the rock control fracture initiation and attributes such as density, aperture width, asperity size, strength and network geometry (Atkinson, 1984; Ingraffea, 1987). Fracture type (mode I, II, III; opening, in-plane shear or out-of-plane shear or a mixture of any/all) influences aperture and therefore permeability, rendering the initial stress regime crucial when predicting the geometry of fractures and networks (Gale et al., 2014). Mode I fractures result from effective tension, leading to open discontinuities that propagate parallel to their own plane due to the orientation of the maximum tensile stress (Fig. 3a) (Atkinson, 2015). Applied shear stress (u_s) in the in-plane direction leads to shear mode II fractures, contrasting from mode III fractures that result from out-of-plane shear stress (Gudmundsson, 2011). Fracture network topology, defining the local to system-wide connectivity (Long and Witherspoon, 1985), is complicated further by the nature of deformation, for example, within rocks that have been subjected to numerous deformational events, exhibiting extensional and compressional (mixed-mode) fractures overprinting one another in a sequential manner (Fig. 3d) (Pollard and Aydin, 1988).

Mudrocks exhibit a wide range of mechanical behaviours spanning brittle and ductile responses to stress (Fig. 3) (Jaeger et al., 2009; Nygard et al., 2006). During ongoing burial, mudrocks behave as normally consolidated materials and exhibit a ductile response to increased loads (Nygard et al., 2006). However, several processes like uplift, chemical diagenesis, and overpressure build-up, turn mudrocks into over-consolidated materials which exhibit brittle behaviour during unloading (Nygard et al., 2006). Under low effective stresses, a brittle mudrock is inherently stronger than a ductile mudrock, enabling

permeability increase through the development of open dilatant fractures syn- and post-deformation (Fig. 3c) (Ingram and Urai, 1999). Shear fractures in brittle mudrocks exhibit dilation at low effective normal stresses (σ_n'), leading to increased permeability with increasing shear deformation (Nygard et al., 2006). Shear fractures formed in ductile mudrocks, conversely, undergo contraction at high effective stresses causing permeability reduction with increasing shear deformation (Fig. 3e) (Gutierrez et al., 2000; Ingram and Urai, 1999). Considering no chemical changes or significant shearing, only compacting shear fractures will remain highly impermeable post-deformation. However, chemical influences characteristic of a fractures opening history can significantly affect permeability depending on the nature and severity of mineral infill; for example, calcite-filled opening-mode fractures are synonymous with mudrocks (Gale et al., 2014; Gale et al., 2007). The effect of chemical influences on fracture roughness, aperture and permeability is discussed in Section 3.3.2.

2.3. Scaling of natural fractures

Observations across a wide range of length scales (thin section up to seismic scales) indicate that many fracture properties (length, aperture, roughness, connectivity and permeability) can be considered to be self-similar and scale-independent, following power-law scaling relationships (Candela et al., 2012; Cowie et al., 1996; Davy et al., 2010; Gillespie et al., 2001; Hooker et al., 2014; Johnston and McCaffrey, 1996; Marrett et al., 1999; Odling et al., 1999; Ortega et al., 2006; Perfect, 1997; Poon et al., 1992; Roy et al., 2007; Schultz et al., 2008; Wei and Xia, 2017; Wong et al., 1989). However, limitations to the range of scaling relationships for mudrock fractures do exist, and recent studies have shown that some fracture systems, particularly in mudrocks, may not show scaling on account of chemical-mechanical interactions (Gale et al., 2014; Laubach et al., 2019).

Fracture size distribution and spacing may be characterised by a variety of size-distribution relationships including exponential, log-normal, power-law and power-exponential relationships (Dershowitz and Einstein, 1988; Hooker et al., 2013; Laubach et al., 2018; Massiot et al., 2015; Priest and Hudson, 1976). Differences in fracture size and distribution arise from fracture growth determined by rock properties, flaws and stress boundary conditions (Hooker et al., 2018). Providing mechanical barriers do not truncate a fracture, propagation, is governed by the total amount of energy in a given system, which is distributed over all existing fractures (Sanderson and Zhang, 1999). In such a scenario, fracture lengths primarily follow power-law distributions. Truncation of fractures caused by mechanical layering leads to elongation of the longitudinal fracture length resulting in cross-sectional fracture heights that follow a negative exponential distribution (Bonnet et al., 2001). For a comprehensive description of the scaling properties of fractures and associated networks, see the review by Bonnet et al. (2001).

2.4. Implications for predictions of fluid flow rates in fractured caprocks

- Accurate, verified, and robust methods to model flow rates in faults and fracture networks require a balance to be struck between representing internal complexity across different length scales and computational feasibility. The widespread nature of fractures, in terms of (multi-scalar) frequency, mechanism of creation, and resulting geometrical complexities, has consequences for accurate fluid flow prediction. A lack of 3D observational data describing natural fracture configurations, specifically in mudrocks, is required to validate fluid flow predictions in modelled low-permeability seals.
- Despite the documentation of pervasive fracturing under certain subsurface conditions, imaging and identifying the presence of fracture systems remains a key challenge in the assessment of storage security risks. Geophysical or log-based imaging methods are

often inadequate, given the small size of fracture and large spatial scales. For example, certain rock types which have been subjected to protracted loading histories and exposed to numerous structural events may still display large (km^2) unfractured regions (e.g. Ellis et al., 2012).
- Diagenetic chemical reactions must not be understated when predicting fracture-size attributes (Gale et al., 2014; Hooker et al., 2013), both in terms of chemically assisted fracture growth (Atkinson, 1984) and dissolution/precipitation, which can lead to changes in host rock and fracture zone mechanical properties (Laubach et al., 2019). The presence of cement precipitation/dissolution may greatly influence both local permeability and large-scale conductivity of a given fault/fracture system, such effects must be accounted for when predicting fluid flow rates through fractured caprock materials.

3. Controls on fluid flow in natural fractures

3.1. Governing equations for single(-phase) fracture permeability

Fundamentally, the physics of single-phase fluid flow through rock fractures is well-understood, being governed by the Navier-Stokes equations (NSE), which can be written, in steady-state, as (Batchelor and Batchelor, 2000):

$$\rho(\boldsymbol{u} \bullet \nabla)\boldsymbol{u} = -\nabla P + \mu \nabla^2 \boldsymbol{u} \tag{1}$$

where ρ is the fluid density, $\boldsymbol{u}$ is the velocity vector, μ is the fluid viscosity, and P is a reduced pressure defined by $P = p - \rho g \zeta$, where p is the fluid pressure and ζ is the coordinate pointing in the direction of the gravitational acceleration (g). The three sets of terms represent advective acceleration, pressure gradient and viscous forces, respectively. NSE are challenging to solve, both analytically and numerically, and thus approximations are typically introduced (Cardenas et al., 2007; Crandall et al., 2010; Zimmerman et al., 2004); ignoring the acceleration terms yields the well-known steady-state Stokes equation (SE):

$$\nabla P = \mu \nabla^2 \boldsymbol{u} \tag{2}$$

representing a linearized relationship between the pressure field and fluid velocity. The SE have been solved numerically for both idealised, synthetic fracture surfaces (Brown et al., 1995; Brush and Thomson, 2003; Cao and Kitanidis, 1998; Mourzenko et al., 1995) and natural fracture surfaces (Cardenas et al., 2009; Kosakowski and Berkowitz, 1999; Lee et al., 2014). The complexity of solutions to the NSE and SE for real fracture geometries (Fig. 4) has commonly motivated their replacement with the more readily solved Reynolds lubrication equation (Brown, 1987). The classical description of fluid flow in a single fracture treats opposing walls as parallel, smooth plates, proposing that local flow magnitudes are well described by the Reynolds equation for Newtonian fluids with negligible fluid body forces (Mourzenko et al., 1995; Zimmerman et al., 1991), such that:

$$\nabla \bullet \left(\frac{a^3(x, y)}{12\mu} \bullet \nabla \Phi \right) = 0 \tag{3}$$

where a is the local aperture (i.e. a function of the spatial coordinates in the plane of the fracture) (Fig. 4b) and Φ is the local hydraulic head. Under such conditions, the volumetric flow rate (Q), can be obtained by integration of the parabolic velocity profile that develops from the centre of the aperture towards the fracture walls (Zimmerman and Bodvarsson, 1996), such that:

$$Q = \frac{-w_f a^3}{12\mu} \frac{dP}{dx} \tag{4}$$

where w_f is the fracture width perpendicular to the flow direction. Written in terms of transmissivity (T) as $Q = -(T/\mu)(dP/dx)$, leading to the "cubic law" (CL) (Snow, 1969; Witherspoon et al., 1980):
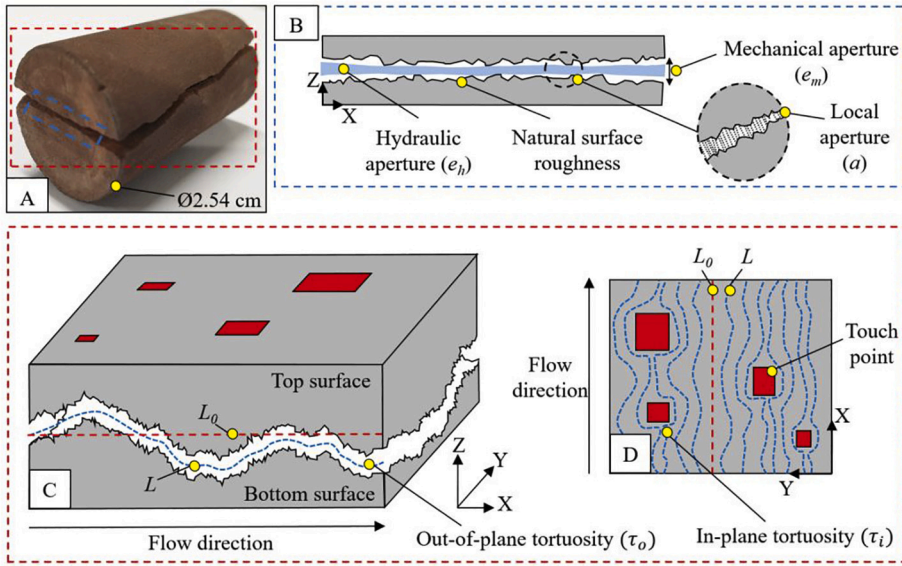
Fig. 4. (A) Photograph of a fractured (drilling-induced) Carmel Formation (Carmel Sample 1) core plug obtained from a scientific drilling campaign near Green River, Utah, USA (Kampman et al., 2014b) (See Appendices A and B). (B) Simplified 2D representation of the region highlighted (dashed blue) in A, showing a rough fracture. The (effective) hydraulic aperture (e_h) always appears smaller than the (geometrically measured) mechanical aperture (e_m) due to surface roughness (Esaki et al., 1999; Huang et al., 2019). Fracture aperture measurements are only valid at a specific stress state and pore pressure. (C) 3D schematic illustration of the region highlighted in A (dashed red), showing a single fracture, its associated aperture distribution, and the relationship between the effective flow path length (L) and the linear distance (L_0) (large-scale tortuosity). (D) Segmented plan view of the fracture shown in C, showing (simplified) discrete touch points where the top and bottom surfaces contact one another, leading to the occlusion of flow paths (meso-scale tortuosity).

$$T = \frac{w_f a^3}{12} \tag{5}$$

where T scales with the cube of the aperture due to Q scaling linearly with w_f perpendicular to the flow. From which a single fracture permeability (k^F) can be expressed as (Zimmerman and Bodvarsson, 1996):

$$\frac{T}{w_f a} = k^F = \frac{a^2}{12} \tag{6}$$

The permeability of a uniformly fractured medium (k^{FM}) with negligible matrix permeability can thus be described by (Adler et al., 2012):

$$k^{FM} = \frac{a^3}{(12 \cdot s)} \tag{7}$$

where s is the fracture spacing.

This (CL) relation adequately describes Darcian (linear) flow in parallel-sided apertures over a wide range of aperture sizes and flow rates (Witherspoon et al., 1980). However, many laboratory experiments (e.g. Durham and Bonner, 1994; Raven and Gale, 1985), field studies (e.g. Novakowski et al., 1995; Rasmuson and Neretnieks, 1986; Raven et al., 1988) and numerical simulations (e.g. Oron and Berkowitz, 1998; Ranjith and Viete, 2011) have shown this classical view does not accurately describe fluid flow in natural rock fractures, where rough surface topology leads to complex and tortuous flow paths, and at high fluid flow rates, where the effects of turbulence, eddies and inertia lead to non-Darcian (turbulent) flow regimes (Fig. 4c).

In discretised fracture flow problems, with fractures of varying aperture, the CL is generally assumed to hold locally (i.e. for each fracture element) giving rise to the local cubic law (LCL) (Ge, 1997; Meheust and Schmittbuhl, 2000; Zimmerman and Bodvarsson, 1996). Modified forms of the LCL have further been introduced to account for fracture surface topology, which leads to a reduction in the effective aperture size open to flow, and for cases including weak inertial forces (e.g. Wang et al., 2015). The concept of a hydraulic aperture (e_h) (Fig. 4b) has been introduced to account for this constricted flow; usually being described as the equivalent (reduced) aperture through which fluid can flow, which when substituted into the CL would yield the correct transmissivity:

$$T = \frac{w_f e_h^3}{12} \tag{8}$$

Discrete surface asperities cause the hydraulic aperture to appear smaller than the opening or displacement of the mechanical aperture (e_m) (Fig. 4b), a purely geometric measure describing the arithmetic mean of the aperture, during normal loading and unloading (Klimczak et al., 2010; Olsson and Barton, 2001). Several formulations have been proposed for this relation, the most commonly used empirical relationship being that of Barton et al. (1985):

$$e_h = \frac{e_m^2}{JRC^{2.5}} \tag{9}$$

where JRC (Joint Roughness Coefficient) is an empirical coefficient describing the surface roughness of fracture profiles (Eq. (10)). Alternative relations are also discussed by Rutqvist and Stephansson (2003).

3.2. Heterogeneous fracture surface roughness and aperture distribution

3.2.1. Self-similar and self-affine surface roughness

Fracture roughness describes the relief of a fracture surface, referring to local departures from planarity in the form of asperities (Adler et al., 2012; Grasselli et al., 2002; Li and Huang, 2015). Fracture surface roughness has been shown to follow fractal power-law scaling relationships (e.g. Brown, 1995a; Brown and Scholz, 1985) where the topological complexity of a line or surface profile (D_E) has a higher (fractal) dimensionality (D_f) than its intrinsic topological dimension (D_T) (e.g. $D_T < D_E$) (Brown and Scholz, 1985). Fracture surfaces may be self-similar, displaying the same roughness regardless of the observational length scale, or self-affine, whereby the surface becomes progressively smoother when viewed at progressively larger length scales (Berkowitz, 2002). This roughness is typically expressed as the height difference between adjacent points on a 2D surface profile, such that $\Delta h \propto \Delta x^H$, where Δh is the height difference over the horizontal distance (Δx). H represents the Hurst coefficient, describing the scale of self-similarity and wavelength correlation properties, which equals 1 for self-similar surfaces and lies between 0 and 1 for self-affine surfaces (Odling, 1994). The Hurst coefficient varies linearly with the 3D fractal dimension, such that $H = D_E - D_f$, where D_E is the Euclidean dimension of the embedding medium (3 for surfaces and 2 for profiles) (Family and Vicsek, 1991; Wang et al., 2016). It is noted that natural rock fractures exhibit H values between 0.45 and 0.85, corresponding to 3D D_f values between 2.55 and 2.15 (Babadagli and Develi, 2003; Babadagli et al., 2015; Brown and Scholz, 1985; Carr and Warriner, 1989; Huang et al., 1992; Kulatilake et al., 2006; Odling, 1994; Poon et al., 1992; Power and Tullis, 1991; Schmittbuhl et al., 1993; Schmittbuhl et al., 2008).

Roughness strongly influences fracture transport properties via the

creation of variable (heterogeneous) apertures, constrictions and contact points, which generate tortuous flow paths (Fig. 4c, d) (Brown and Scholz, 1985; Pyrak-Nolte et al., 1988; Tsang, 1984). The size and distribution of the hydraulic aperture, and the tortuosity of the flow paths available to fluids, ultimately control fracture transport properties, rendering this a key input parameter for numerical models aiming to predict fluid transport (e.g. Obeysekara et al., 2018; Zhao et al., 2011). Experimental investigation (e.g. Qian et al., 2011; Walsh and Brace, 1984) and theoretical analysis (e.g. Brown, 1987; Moreno et al., 1988; Tsang, 1984; Tsang and Tsang, 1987; Wang et al., 1988) highlight the effect of surface roughness on fracture transport properties, especially in smaller apertures where the separation is small relative to the magnitude of surface roughness.

Several metrics have been proposed to quantify fracture surface roughness, including, but not limited to; (i) the empirical joint roughness coefficient (*JRC*) (e.g. Barton et al., 1985; Olsson and Barton, 2001), commonly expressed as (Barton and Choubey, 1977; Tse and Cruden, 1979):

$$JRC = 32.2 + 32.47 \log Z_2; \qquad (10)$$

where Z_2 is the dimensionless root mean square of the first derivative of a fracture surface profile, expressed in the discrete form (Myers, 1962):

$$Z_2 = \left[\frac{1}{N_t} \sum \left(\frac{Z_{i-1} - Z_i}{x_{i-1} - x_i} \right)^2 \right]^{1/2} \qquad (11)$$

where x_i and Z_i denote the co-ordinates of the fracture surface profile, N_t the number of sampling points along the fracture length, and; (ii) relative roughness (σ_a/a_m), describing the ratio of the standard deviation (σ_a) and initial mean of the aperture field (a_m) (e.g. Barton and de Quadros, 1997; Brown, 1987; Brush and Thomson, 2003; Ge, 1997; Kling et al., 2017; Matsuki et al., 1999; Rasouli and Hosseinian, 2011; Renshaw, 1995; Xie et al., 2015; Xiong et al., 2011).

3.2.2. Tortuosity

Fractures exhibit tortuosity (τ) at multiple scales, where tortuosity is defined as the effective flow path length between two points divided by the linear distance, $\tau = L/L_0$ (Bear, 1972). Fine-scale tortuosity, or roughness, results from small-scale fracture surface irregularities, mineral grain topology, bedding discontinuities, and fracture intersections (Fig. 4b), such as those accounted for in the modified LCL. Meso-scale tortuosity results from increased fracture contact areas and the complete occlusion of flow paths (Fig. 4d). Large-scale tortuosity arises from anisotropies and heterogeneities within the host formation that generate large-scale fracture surface irregularities (Fig. 4c). Ultimately, fluid flow decreases with fracture closure (Δa) as aperture size and connectivity decrease, and fracture contact area and flow path tortuosity increase (Briggs et al., 2017; Brown, 1995b; Nicholl et al., 1999; Tsang, 1984; Tsang and Tsang, 1987; Walsh, 1981). The greater the number of small apertures within the overall aperture distribution, the greater the influence of tortuosity (Lemarchand et al., 2010; Tsang, 1984; Wang et al., 2015).

Fracture tortuosity can decrease fluid flow by two or more orders of magnitude when the fracture wall contact area increases above 30% (Brown, 1995b). Rugged natural fracture topographies comprise a large spectrum of wavelengths and amplitudes (Fig. 4) (Babadagli et al., 2015; Brown, 1987; Brown and Scholz, 1985; Poon et al., 1992; Schmittbuhl et al., 1993). At shorter wavelengths and amplitudes, fracture surfaces become uncorrelated, producing asperities of contact (Hustrulid and Johnson, 1990). Variations in wavelength and amplitude may account for increased flow path length and differences within the cross-sectional area of flow as a result of surface roughness (Waite et al., 1998), known as out-of-plane tortuosity (τ_0) (Fig. 4c). For example, the contribution of out-of-plane tortuosity to a reduced fracture permeability ($K^{\overline{F}}$) may be expressed as:

$$K^{\overline{F}} = \frac{e_h{}^2}{(12 \cdot \tau_0)} \qquad (12)$$

In-plane tortuosity (τ_i) (Fig. 4d) must be considered where fracture planes exhibit contact areas, which, in turn, influences flow paths, as fluid can only migrate through connecting void space (i.e. increased path lengths) (Hustrulid and Johnson, 1990). The contribution of these contact areas to fracture permeability reduction is most simply expressed for circular contact regions as:

$$\overline{k^F} = \frac{1 - \alpha_c}{1 + \alpha_c} k^F \qquad (13)$$

where α_c is the ratio of the contact area to the total fracture area (Walsh, 1981).

3.3. Fracture surface roughness in mudrocks

3.3.1. Observations of fracture surface roughness

As with all other fractured rocks, mudrock fractures display surface roughness to various degrees as a result of small-scale irregularities. Coarser-grained lithologies (e.g. sandstone, limestone) have been shown to exhibit rougher profiles than fine-grained lithologies (e.g. mudrocks) (e.g. Al-Fahmi et al., 2018). Studies have demonstrated that for a range of mudrocks with similar mineralogy, fractures aligned normal to bedding had higher surface roughness than those aligned parallel to bedding (Forbes Inskip et al., 2018; Yin, 2018). Such findings may suggest surface roughness is partly controlled by grain size and orientation. For example, parallel to bedding, grains align with bedding (i.e. depositional alignment), whereas, a fracture forming at higher angles to bedding may become progressively rougher due to grain end exposure. However, some studies have also uncovered a weak relation between angle to bedding and surface roughness (Huang et al., 2020). Additionally, mineralogy has been shown to influence surface roughness distribution in natural faults, where topographies varied extensively in clay-rich samples compared to the more concentrated regions of surface relief in calcite-rich samples (Wu et al., 2017). Observations from fractures in the Carmel Formation (see Fig. 4a and Appendix A) attest to the topographic complexities observed in both drilling-induced and natural fractures.

Due to the propensity of mudrocks to fragment during the coring process, surface weathering, and difficulties associated with distinguishing natural and drilling-induced fractures (Kulander et al., 1990), obtaining naturally fractured mudrock samples representative of subsurface conditions is challenging. These difficulties are reflected in the sparsity of naturally fractured mudrock data. Fracture surface roughness is also a result of diagenetic history and geomechanical influences, and, as is the case with other rock types, mudrocks are not exempt from chemical alteration (e.g. Jia et al., 2018).

3.3.2. Geochemical influences

Mudrock fractures, as a matter of course, contain minerals that are prone to chemically-driven alteration when exposed to high temperatures and mineral-laden fluids in the deep subsurface. Over geological timescales, mudrock fractures formed under moderate to deep burial conditions and prolonged high temperatures are commonly cemented (e.g. with calcite). Such diagenetic processes can profoundly influence fracture aperture and intrinsic flow properties, resulting in mudrock fractures with little to no porosity due to fibrous crystal infill (Bons et al., 2012; Hooker et al., 2019). However, due to the intrinsically low permeability of mudrocks, fractures with low porosity mineral infill may still represent regions of enhanced permeability compared to the surrounding host lithology (Landry et al., 2016). Additionally, incomplete fracture sealing may result in persistent mechanical weakness (Hooker and Katz, 2015; Lee et al., 2015). Heterogeneous surface mineralogy promotes heterogeneous mineral precipitation, commonly resulting in thinly-lined mineralisation of the fracture wall-rock

interspersed with thicker, highly localised deposits (Lander and Laubach, 2015; Laubach, 2003), shown to exist in mudrocks (Gale et al., 2014). Conversely, fracture wall-rock composition may impede or enhance precipitation of particular mineral phases due to crystal nucleation barriers and epitaxial and syntaxial growth effects (Gale et al., 2014).

On engineering timescales, a fracture may undergo aperture (and permeability) modification, for example, through carbonate precipitation during the flow of CO_2-saturated brine through fractured mudrocks (Kampman, 2018). Conversely, carbonate minerals filling fractures may be dissolved, for example, via the dissolution of CO_2 into resident brines which form acidified fluids that promote carbonate mineral dissolution (Fitts and Peters, 2013; Gaus, 2010) and fracture aperture enlargement (Ellis et al., 2011). The magnitude and severity of fracture mineral precipitation/dissolution is strongly dependent on the progress of coupled reactive transport processes (Detwiler, 2010; Kampman et al., 2014a), with their importance on fracture transport garnering wide attention and review (Deng and Spycher, 2019; Song and Zhang, 2013; Taron et al., 2009; Xiao et al., 2018). Mudrock fracture aperture may also be subject to clay (e.g. smectite) swelling processes, whereby the adsorption of CO_2 induces appreciable volumetric strains (Busch et al., 2016; Busch et al., 2020; Wentinck and Busch, 2017).

In addition to mineralogical heterogeneity, fracture surface roughness also perturbs feedback between mineral precipitation and permeability alteration (Chaudhuri et al., 2012). The degree of roughness can affect reaction rates, either through promoting enhancedsolid-phase reactivity through increasing surface area (Deng et al., 2018), or influencing the progress of reaction rates depending on hydraulic tortuosity within the fracture (Deng et al., 2013). The resulting mineral heterogeneity can exert strong influences on fluid transport and therefore requires careful consideration and sophisticated modelling techniques to determine the relative impact of such phenomena on permeability (Ankit et al., 2015; Lander and Laubach, 2015; Wendler et al., 2016). Considering a fracture with uniform mineralogy, rapid permeability reduction (fracture sealing) could result from progressive smoothing of the fracture surface (Hilgers et al., 2004; Hilgers and Urai, 2002), however such permeability response is commonly disrupted by the absence of reactive wall-rock minerals, allowing large aperture voids to persist (Lee and Morse, 1999). Experimental investigation has demonstrated fracture wall roughness, alongside fluid chemical composition and flow rate, to be a primary control on mineral precipitation, with rough-walled fractures clogging faster than their smooth-walled counterparts (Singurindy and Berkowitz, 2005). Experimental studies investigating the impact of mineral precipitation on fracture permeability are difficult, partly due to the length of time required to observe precipitation (in the order of months) and difficulties associated with precipitation occurring mainly at the fracture inlet (Jones and Detwiler, 2016). For a comprehensive review of reactive transport processes in fractures, see the review by Deng and Spycher (2019) and references therein.

3.4. Implications for predictions of fluid flow rates in fractured caprocks

- Obtaining an improved understanding of the interplay between surface geometry, pore pressure, and effective stress, coupled with a strong quantification of multi-scalar tortuosity to determine the available area for advective flow, is a critical component in the accurate modelling of fracture flow to achieve realistic flow rates (Berre et al., 2018; Pyrak-Nolte et al., 1988; Raven and Gale, 1985).
- Fracture mineralisation can profoundly influence fracture aperture and thus intrinsic transport properties, with mineral precipitation either, preserving or destroying fracture permeability (Laubach, 2003). The degree to which permeability is affected, particularly across widely varying temporal scales (Gratier, 2011), is pertinent information which must be accounted for in leakage modelling. However, despite active research our understanding of such

processes is largely unresolved (Hooker et al., 2019), which currently limits our capabilities to model and determine the implications of such phenomena in scenario-based leakage modelling.
- Studies have shown reactive transport can significantly affect mineral precipitation/dissolution, and in the case of dissolution can exacerbate leakage risks. Averting the risks associated with fracture-driven leakage requires increased understanding of the factors which govern geochemical and goemechanical alterations in fractures (Spokas et al., 2018). Despite widespread acknowledgement that reactive transport may significantly alter fracture mineralogy and surface roughness, the interplay between geomechanical and geochemical processes remains largely unclear (Spokas et al., 2019).

4. Non-Darcian flow regimes

In rough fractures, sharp corners, bends, and crevices, can lead to the formation of eddies (regions of nonlinear flow) and significant inertial forces (e.g. flow separation), causing a breakdown in the validity of the linear flow laws (Brown, 1987; Glover et al., 1997; Qian et al., 2012; Radilla et al., 2013; Zhou et al., 2015; Zimmerman et al., 1992). Non-Darcian (nonlinear) flow may be induced by surface roughness or by an increase in pressure gradient (Elsworth and Doe, 1986; Wang et al., 2016; Wen et al., 2006; Yeo and Ge, 2001). Diverging or converging fracture surfaces, and differential acceleration across these surfaces, cause deviations in the flow velocity profile from the ideal parabolic shape predicted by the CL (Brown, 1995b; Brush and Thomson, 2003), and the formation of whorls and stagnant zones around contact points (Briggs et al., 2017; Gutfraind and Hansen, 1995; Oron and Berkowitz, 1998; Raven et al., 1988). These artefacts of surface roughness result in higher energy dissipation than that predicted between two smooth parallel plates, signifying lower flow rates in rough-walled fractures (Konzuk and Kueper, 2004).

4.1. Characterising non-Darcian flow

The emergence of nonlinear flow occurs when the increase in discharge is smaller than the proportional increase in pressure gradient. These nonlinear inertial flow regimes may be expressed empirically, through the Forchheimer equation (Forchheimer, 1901), where the pressure drop is a quadratic function of the flow rate, written by Bear (1972) as:

$$- \nabla p = A_e Q + B_e Q^2 \tag{14}$$

where $A_e Q$ and $B_e Q$ denote the coefficients describing energy losses due to viscous and inertial dissipation mechanisms, respectively (Moutsopoulos, 2009). From this, a dimensionless Forchheimer number (F_0), widely used to define the ratio of nonlinear to linear pressure losses (i.e. $F_0 = A_e Q / B_e Q$), for a single rough-walled fracture can be derived (Chen et al., 2015; Javadi et al., 2014; Nowamooz et al., 2009; Zhou et al., 2015). Another traditionally employed dimensionless measure of the strength of inertial to viscous forces relative to one another in a single rough fracture is the Reynolds number (Re), with the latter dominating at low Re (Brush and Thomson, 2003; Ranjith and Darlington, 2007; Zimmerman et al., 1991):

$$Re = \frac{\rho \tilde{v} e_m}{\mu} \tag{15}$$

where $\tilde{v}$ is the mean velocity. Termination of linear flow in a rough-walled fracture may be characterised by a critical Reynolds number, Re_c:

$$Re_c = \frac{F_0}{\beta} \tag{16}$$

where β is a dimensionless Forchhemier coefficient introduced by Zimmerman et al. (2004). Zimmerman et al. (2004) and Zeng and Grigg (2006) define the critical condition for the onset of nonlinearity as the

point at which the pressure gradient continues approximately 10 % of the overall pressure gradient (i.e. $F_0 = 0.11$). Deviations from linear flow occur as a function of the ratio of aperture to the wavelength of the dominant aperture (a/λ_a) (Ai-Yaarubi et al., 2005). For a review of the critical conditions controlling the onset of nonlinear flow regimes in fractures, see Yu et al. (2017).

4.2. Validity of governing flow equations

In practice, full NSE (Eq. (1)) comprehensively describe fluid transmissivity in rough-walled fractures, stating a nonlinear relation between the hydraulic head and flow velocity, however, nonlinear flow leads to increased observational and computational intensity. Neglecting inertia (or when viscous forces are dominant; i.e. $Re < 1$) leads to a simplification of the NSE to the SE (Eq. (2)), where it has been shown that the latter can be adequately replaced by the simpler Reynolds equation (Eq. (3)). This is valid if the wavelength of the dominant aperture variations is approximately 3 times greater than the mechanical aperture, or exhibit a relative roughness of < 0.23, however, many natural fractures do not satisfy this condition (Ai-Yaarubi et al., 2005; Meheust and Schmittbuhl, 2003; Zimmerman and Yeo, 2000). A central, yet unsolved, question, is how to correlate fluid flow with the complex geometries observed in natural fractures, especially considering abrupt aperture field changes (Qian et al., 2012).

4.2.1. Simulating flow in complex geometries

Traditional computational flow dynamic (CFD) approaches to model flow through fractures with complex geometries adopt the (Darcian-type) LCL due to its relative (computational and analytical) simplicity (e.g. Brown, 1987; David, 1993; Moreno et al., 1988; Nazridoust et al., 2006; Thompson and Brown, 1991; Unger and Mase, 1993; Witherspoon et al., 1980). Reduced computational intensity is achieved through, for example, application of the CL locally in each subcell, representing a lower-dimensional solution that utilises square rather than irregular or hexagonal grids required when using NSE. However, discarding the out-of-plane velocity introduces errors (10 - 20 % of NSE) that increase as a function of relative roughness (Zimmerman et al., 2004). In some cases with an $Re < 1$, the LCL overestimated the flow rate by approximately 75 % (Konzuk and Kueper, 2004), with an earlier study reporting a 22 to 47 % overestimation (Nicholl et al., 1999). Such deviations are attributed, at low velocities, to the LCL neglecting rough walls, asperity contact, and thus tortuous flow paths (Brown, 1987; Sisavath et al., 2003), while at higher velocities, by the nonlinear nature of flow (Boutt et al., 2006). Breakdown in the validity of the LCL, therefore, occurs when the two primary conditions leading the NSE, SE and lubrication equations are not satisfied; (i) wavelength of the dominant aperture appears 3 times less than the mean aperture, and; (ii) the onset of nonlinear flow. These theoretical benchmarks are supported by numerical (e.g. Basha and El-Asmar, 2003; Koyama et al., 2008; Skjetne et al., 1999) and experimental investigations (e.g. Durham and Bonner, 1994; Keller et al., 1995; Louis, 1969; Qian et al., 2007; Qian et al., 2005; Raven and Gale, 1985). Questions have also been raised as to the validity of the LCL at varying stresses, for example, Pyrak-Nolte et al. (1987) concluded (experimentally) a breakdown in the LCL at either high or low stresses for naturally fractured crystalline rocks.

Numerical experiments performed to solve the Reynolds equation in a 3D fracture indicated that roughness may cause deviation from the CL by 10 - 50 % (Briggs et al., 2017; Brown, 1987). Through measuring velocity vectors to analyse inertial and viscous forces, Lee et al. (2014) found that, under low flow regimes (i.e. $Re < 0.1$), inertial forces were negligible compared to viscous forces in a highly rough-walled region, confirming that flow nonlineairty was not the cause of flow rate overestimation. Furthermore, overestimation was shown to increase by 47 - 60 % with increasing roughness, indicating that discrete roughness alterations for $Re < 1$ significantly alter flow rates derived using the Reynolds equation. Several studies have discussed cases when simplifications of the full NSE are acceptable (e.g. Brown, 1995b; Brush and Thomson, 2003). Understanding which geometric and hydraulic scenarios represent acceptable limits comes with great difficulty (Zimmerman and Yeo, 2000), implying that the validity of the Reynolds equation, even under low inertial regimes, remains an open question.

Flow simulations using the SE represents a more computationally inexpensive undertaking than the full nonlinear NSE, with the former being limited to lower flow velocities. For example, Konzuk and Kueper (2004) showed that application of the SE at $Re > 1$ led to an over-prediction of flow rates by up to 90 %. NSE have previously been solved using different representations of a rough fracture with varying success (e.g. Ai-Yaarubi et al., 2005; Boutt et al., 2006; Brown, 1995b; Brush and Thomson, 2003; Cardenas et al., 2007; Kim et al., 2003; Madadi et al., 2003; Waite et al., 1998; Zimmerman et al., 2004). 2D steady-state NSE simulations undertaken on natural surface topographies illustrated the importance of directionality, surface roughness, and aperture over millimetre to centimetre length scales (Cardenas et al., 2007; Cardenas et al., 2009). Brush and Thomson (2003) examined the effect of roughness on the validity of the LCL through solving 3D NSE and SE in synthetically generated normally and log-normally distributed apertures, where simulations clearly demonstrated that for larger values of relative roughness, inertial forces significantly affect the flow field. Cheng (2018) proposed a modified CL accounting for nonlinearity in the NSE and variations in both vertical and horizontal velocities. Despite improvements in terms of transmissivities and pressure distributions over previously implemented LCL investigations (e.g. Hakami and Larsson, 1996; Koyama et al., 2008; Mourzenko et al., 1995; Vilarrasa et al., 2011; Yeo et al., 1998), it's reliability in predicting realistic flow rates is still subject to debate.

4.2.2. Capturing roughness and towards solving non-Darcian flow problems

In the case of large fracture apertures (i.e. mean aperture larger than the critical value), surface roughness can be disregarded as it's effect diminishes with increasing mean aperture, enabling a fracture to be adequately represented using parallel plates (Boutt et al., 2006; Crandall et al., 2010; Sisavath et al., 2003). In scenarios where surface roughness appears in the same order of magnitude as the mean aperture, resulting geometric complexities must be accounted for to capture the full physics of flow (Boutt et al., 2006). Capturing velocity distributions in a single rough fracture benefits from a CFD approach (Dijk and Berkowitz, 1998), from which a popular numerical method for simulating flow governed by NSE can be adopted, termed the Lattice Boltzmann method (LBM) (Boutt et al., 2006; Eker and Akin, 2006; Yan and Koplik, 2008). The discrete nature of the LBM makes it efficient in modelling complex geometries (Briggs et al., 2014; Lammers et al., 2006), characteristic of rough fractures. Full details of the development, groups of methods, and application of the LBM can be found in Succi (2001) and Sukop and Thorne (2007).

As the (fracture) flow domain is bounded by rough surfaces, the discrete LBM specifies the excluded solid region (aperture) as a lattice that can accommodate a variety of boundary conditions, namely; (i) pressure drops across a fluid-fluid interface; (ii) wetting phenomena at a fluid-solid interface, and; (iii) maintain constant pressure or velocity boundary conditions (Tian et al., 2011), making it advantageous for single- and two-phase fluid mechanical calculations (Yan and Koplik, 2008). Despite possessing the capabilities of solving NSE on the macroscopic scale (He and Luo, 1997; Qian et al., 1992), simulating flow (Briggs et al., 2017; Ju et al., 2017), characterising the influence of wettability (Dou et al., 2013) and the effect of shear (Zhou et al., 2018) in natural and synthetic fractures, LBM simulations of nonlinear flow in 3D rough fractures are rare (e.g. Wang et al., 2016; Yang et al., 2018). Difficulties arise when quantitatively analysing nonlinear flow in rough fractures, primarily because of multi-scale surface roughness. For example, representing primary (large-scale waviness) and secondary roughness (unevenness superimposed on the primary roughness), and

the influence this has on physical processes, such as turbulence (e.g. Eddy flow), in a manner which does not increase the computational cost, remains an important and unsolved area of research (Drikakis et al., 2019; Wang et al., 2016). 2D simulations of nonlinear flow in rough fractures suffer from failing to capture flow behaviours through primary (large aperture regions) and secondary (smaller aperture regions) conductive paths as a consequence of overestimating the effect of roughness on reducing the effective advective flow area (Wang et al., 2016). The prediction, evolution and representation of turbulence is frustrated by a lack of quantitative investigation into the severity and distribution of nonlinear flow initiation in relation to alterations in surface geometry, and the existence of studies analysing non-steady-state evolution of Eddy flow regions (Zou et al., 2015).

4.3. Implications for predictions of fluid flow rates in fractured caprocks

- Fracture geometries in nature are highly complex and do not appear as perfectly planar surfaces, despite most large-scale fracture network models representing them in this manner (Berre et al., 2018; Flemisch et al., 2018). The challenge to produce fully realised, predictive models of fluid flow in fractured media is rooted, in part, by our limited capabilities of representing fracture surface roughness on the single-fracture scale (Luo et al., 2016), particularly under nonlinear flow regimes. Progressing the understanding of flow processes through rough fractures on the continuum scale necessitates working with full NSE (Ai-Yaarubi et al., 2005; Brush and Thomson, 2003; Cardenas et al., 2007; Liu et al., 2020; Waite et al., 1998; Zou et al., 2015).
- Achieving a more fundamental understanding of how to quantify the nonlinear relationship between flow rate and pressure drop during non-Darcian flow is highly desirable for the prediction of fluid fluxes and the impact this may have on storage security. The degree to which secondary fluid flow phenomena, such as Eddy flow, cause deviations in fluid flow predictions through a single fracture, undoubtedly has consequences for the prediction of flow rates in fracture networks and faults.

5. Two-phase fracture permeability

5.1. The nature of two-phase flow

Multiphase flow through rough-walled fractures in caprocks is a process significant to many geoenergy applications, including CO_2 and energy storage. Constitutive relationships, including capillary pressure and relative permeability models, are essential to model multiphase flow in both rock matrix and fractures in such systems. For example, the significant reduction in permeability of a brine-filled fracture to CO_2, at intermediate saturations, will strongly reduce CO_2 leakage rates from a storage reservoir through leakage pathways such as fractures. Experimental or numerical studies of CO_2-brine relative permeability behaviour in fractures are rare, one of the few studies is presented by Oh et al. (2013).

A fractures ability to transmit two phases, for example, CO_2 and brine, depends on its intrinsic permeability, which is governed by a complex interplay between fracture geometry (Hu et al., 2019; Renshaw, 1995), confining stress (Bertels et al., 2001; da Silva et al., 2019; Huo and Benson, 2016), fluid properties (Glass et al., 1998; Glass et al., 2003), surface wetting properties (Dou et al., 2013; Huppert and Neufeld, 2014), and initial and boundary conditions for flow (Glass et al., 1998). Relative permeability (k_r) is a measure of the reduction in permeability to a given wetting (w) or non-wetting (nw) phase that occurs between partially (k_f) and fully saturated (k_s) conditions (i.e. $k_r = k_f/k_s$) (Romm, 1966). During two-phase flow, the permeability of a fracture to a given fluid phase ($k_{r,\,w}$ or $k_{r,\,nw}$) is determined by the geometry of that phase, which in turn evolves during the displacement of one fluid (defending phase) by another (invading phase). While the

fracture apertures are occupied by wetting and non-wetting phases, each phase can only move through its own continuous pathway. At any given stage of its development, phase geometry is a history-dependent product of competition between local capillary, viscous, and gravity forces (Glass and Nicholl, 1995), and inertia at high flow rates. The two-phase flow velocity (v_w or v_{nw}), in individual fractures, can be relative via Darcy's law and written explicitly as:

$$v_w = -k\frac{k_{r,w}}{\mu_{v,w}}(\nabla P_w - \rho_w G) \tag{17}$$

$$v_{nw} = -k\frac{k_{r,nw}}{\mu_{v,nw}}(\nabla P_{nw} - \rho_{nw} G) \tag{18}$$

where $\mu_{v,\,w}$ and $\mu_{v,\,nw}$ represent the wetting and non-wetting dynamic viscosities, G is the gravity constant, P_{nw} and P_w are the non-wetting and wetting phase pressures, and ρ_{nw} and ρ_w are the non-wetting and wetting phase densities, respectively. The simplest X-type relative permeability model suggests negligible interference between phases within a fracture so that wetting and non-wetting phase relative permeabilities, $k_{r,\,w}$ and $k_{r,\,nw}$, respectively, change linearly with wetting phase saturation (S_w):

$$k_{r,w} = S_w \tag{19}$$

$$k_{r,nw} = 1 - S_w = S_{nw} \tag{20}$$

where S_{nw} represents the non-wetting phase saturation.

In the absence of an influence of capillarity, relations between wetting and non-wetting phase relative permeabilities agree with that of the X-type relative permeability curves (Romm, 1966). However, for smaller fracture apertures, the relative permeabilities are strongly influenced by capillarity, and in the case of viscous-dominated flow, the fluid fluxes (Glass and Nicholl, 1995). Further, the fracture orientation has a strong impact on relative permeability behaviour via the competing influence of gravity, capillary and viscous forces. The nature of the two-phase flows include bubble, slug, and channel flows, depending on the relative velocity of the wetting and non-wetting phases (Fig. 5), and the phase relative permeabilities may depend on the nature of these flow structures (Chen et al., 2004). Wetting phase imbibition into the matrix surrounding a fracture can also drive co-current and/or counter-current flows into the fracture, which influences relative permeability behaviour. For example, matrix-fracture counter-current imbibition strongly influences relative permeability behaviour in water-wet fractured oil reservoirs (Babadagli and Ershaghi, 1992), but, its significance for drainage displacement during CO_2 fracture flow has not been
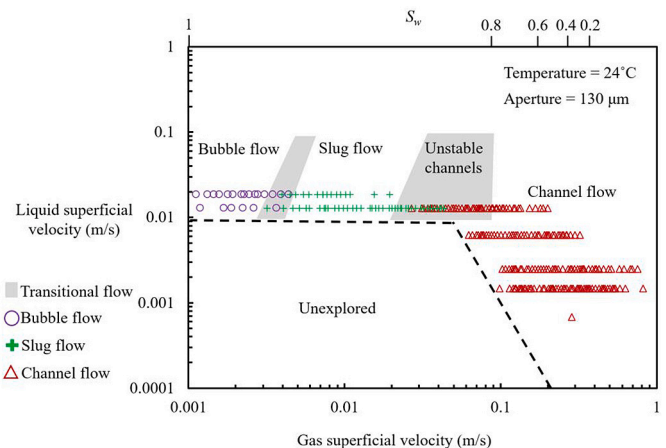

Fig. 5. Experimentally determined bubble, slug, and channel flow behaviour in a smooth fracture, determined as a function of wetting (liquid) and non-wetting (gas) flow velocities (redrawn after Chen et al. (2004)).

studied. Additionally, relative permeabilities above the single fracture scale become scale-dependent under the influence of the complex flow dynamics in fracture networks (Ju et al., 2017).

5.1.1. Capillarity and two-phase flow in fractures

For a vertical fracture under the effects of gravity, and in capillary equilibrium, capillary pressure (P_c) varies with vertical position as:

$$P_c = \Delta\rho g h \tag{21}$$

where h is vertical height above a surface where $P_c = 0$, and $\Delta\rho$ is the density contrast between the two phases. The capillary pressure is thus related to the wetting and non-wetting phase saturations via the familiar Brooks-Corey model for porous media capillary pressure curves as:

$$P_c = P_e \left(\frac{S_w - S_{w,r}}{1 - S_{w,r}} \right)^{-\frac{1}{\lambda}} \tag{22}$$

where λ is an empirical pore size distribution index and $S_{w,r}$ is the residual wetting phase saturation. The Brooks-Corey model has been used successfully in the interpretation of capillary pressure-saturation relationships in rock fractures (Reitsma and Kueper, 1994). Therefore, under the influence of gravity, saturations and thus relative permeability vary with vertical position in a vertical fracture.

During slow immiscible fluid displacement in a horizontal rough-walled fracture, where viscous and gravity forces are negligible, phase geometries are determined by the capillarity, except at either higher contact angles (90°) or intrinsic permeabilities ($> 10^{-10}$ m²), where no influence of capillarity is observed, as demonstrated experimentally and numerically for larger aperture fractures (Romm, 1966; Watanabe et al., 2015). The capillary entry pressure depends on the interfacial tension (γ) and curvature of the fluid-fluid interface in the fracture plane, which can be expressed as the general Young-Laplace equation:

$$P_e = P_{nw} - P_w = \gamma \left(\frac{1}{R_1} + \frac{1}{R_2} \right) \tag{23}$$

where R_1 and R_2 are the aperture-induced and in-plane radii of curvature of the fluid-fluid interface, respectively (Fig. 6). Generally, R_1 dictates the phase structure and R_2 is neglected (i.e. when the correlation length of the aperture field is much larger than the mean aperture) (Glass et al., 2003), such that the fluid-fluid interface curvature can be directly related to the aperture size and fluid-fluid contact angle (θ) as:

$$R_1 = \frac{a}{2\cos\theta} \tag{24}$$

Substituting Eq. (24) into Eq. (23) yields the Young-Laplace equation for local capillary force balance between displacing and defending phases, such that the capillary entry pressure is:

$$P_e = \frac{2\gamma \cos\theta}{a} \tag{25}$$

Considering a horizontal rough fracture composed of many elementary parallel plates. Under quasi-static conditions (low-pressure gradient) and assuming a local equilibrium, P_c within each elementary volume, with aperture, is uniformly distributed and the occupancy of wetting and non-wetting phases is completely governed by the local capillary pressure. Specifically, for an externally imposed P_c, fracture apertures smaller than the critical aperture size $a_c = 2\gamma \cos\theta/P_c$ are preferentially occupied by wetting phase and the rest by the non-wetting phase. Consequently, fracture phase occupancy is controlled by the aperture distribution. The non-wetting phase saturation (S_{nw}) of the fracture corresponds to the fractional void volume with apertures bigger than a_c, which can be explicitly expressed for any aperture distribution $f(a)$ as:

$$S_{nw} = \frac{\int_{a_c}^{\infty} a f(a) da}{\int_0^{\infty} a f(a) da} \tag{26}$$

and the corresponding wetting phase saturation is the fractional void volume of apertures smaller than a_c:

$$S_w = \frac{\int_0^{a_c} a f(a) da}{\int_0^{\infty} a f(a) da} = 1 - S_{nw} \tag{27}$$

However, a portion of the wetting or non-wetting phase in two-phase displacements would usually be trapped or bypassed as a result of the local capillary force and heterogeneity (Chen and Horne, 2006; Knackstedt et al., 2001). Therefore, the wetting and non-wetting residual saturations depend not only on the size of aperture distribution but also on the spatial correlation of apertures. When the wetting phase is restricted to the apertures smaller than a critical value ($a_{c, min}$), these few scattered areas are insufficient to construct a continuous flow path. The volume fraction of the immobile wetting phase is defined as the residual wetting phase saturation (or irreducible saturation), as:

$$S_{w,r} = \frac{\int_0^{a_{c,min}} a f(a) da}{\int_0^{\infty} a f(a) da} \tag{28}$$

Similarly, the non-wetting phase limited to fracture apertures larger than a critical value ($a_{c, max}$) cannot flow any more, and this defines the residual non-wetting phase saturation ($S_{nw, r}$) as:

$$S_{nw,r} = \frac{\int_{a_{c,max}}^{\infty} a f(a) da}{\int_0^{\infty} a f(a) da} \tag{29}$$

The values of $a_{c, min}$ and $a_{c, max}$ depend both on the mean and standard deviation of the aperture distribution and can be fitted from experiments or numerical simulation.

In a statistically homogeneous horizontal fracture much larger than
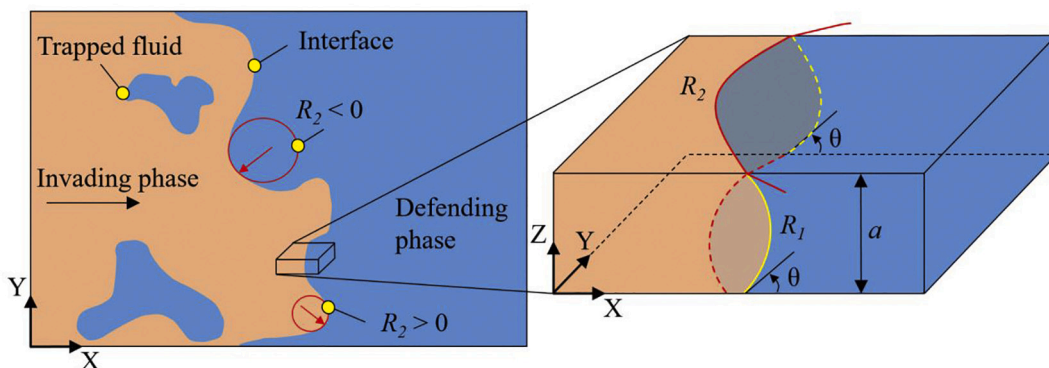

Fig. 6. Illustration of the two principal radii (R_1; aperture-induced radii, R_2; in-plane radii) for a two-phase fluid-fluid interface within a rough-walled fracture (redrawn after Yang et al. (2019b)).
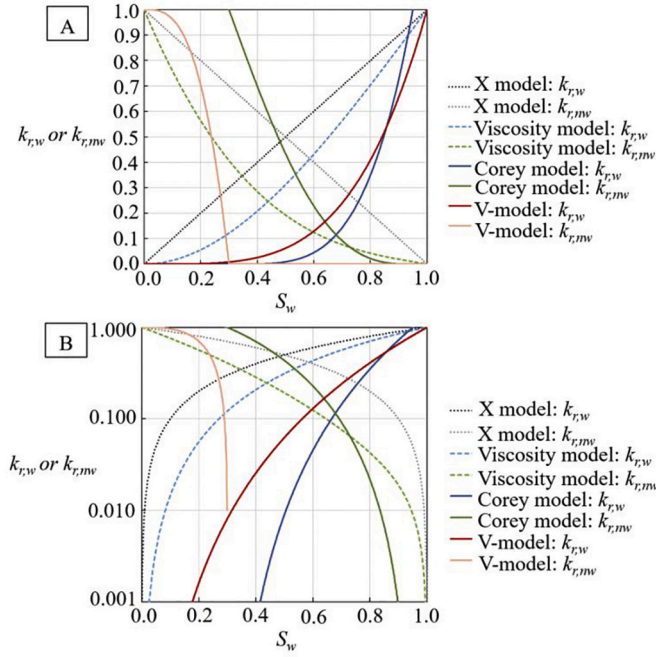
Fig. 7. (A) Relative permeability and (B) log relative permeability of brine-CO_2 versus phase saturation, at 50°C and 200 bar, computed using the X, viscosity, Corey and V-models, for a water-wet system.

the spatial correlation length of the aperture field, slow, steady displacement along the fracture plane leads to a satiated condition where the invading phase spans the fracture in all directions, and the remaining defending phase is fully entrapped (Glass et al., 1995). Following invasion to a satiated state, lack of an escape path for the entrapped defending phase precludes further changes in the geometry of the respective phases. Lateral diversion of flow by an immobile entrapped phase increases average path length through the fracture with respect to that for the saturated case. This decreases the effective hydraulic gradient, and consequently fracture permeability. The critical saturations that define the satiated condition are termed the satiated saturation of the wetting (S_{ws}) and non-wetting (S_{nws}) phases, with a corresponding satiated value of the relative permeabilities ($k_{rs,\ w}$, $k_{rs,\ nw}$), that limit the maximum value of k_s to be < 1. Satiation can be a significant effect in horizontal fractures, but for non-horizontal fractures the values of S_{ws} and S_{nws} generally approach unity and consequently $k_{rs,\ w}$ and $k_{rs,\ nw}$ approach k_s.

5.2. Experimental studies

The appropriate form of relative permeability curves for two-phase flow through rough fractures, and fracture networks, has been debated extensively in the literature. A range of experimental, numerical and theoretical studies have attempted to derive two-phase relative permeability models for fractured media. The various approaches commonly used for predicting the two-phase relative permeability of fractures can be classified into the microscopic (or statistical) approach, and the macroscopic approach developed for porous media. However, the low capillarity and 2D pore network geometry of fractured media mean that the nature of the fluid displacement in fractures is distinct from that in porous media.

5.2.1. Microscopic relative permeability models
Several authors have attempted to use microscopic models derived for porous media, including the viscous coupling (Fourar and Bories, 1995), Corey (Corey, 1954), Burdine (Burdine, 1953) and Mualem models (Mualem, 1976), to model fractures as a 2D porous network.

These microscopic models have generally been developed theoretically based on the pore size spatial distribution and the assumption of an assemblage of parallel capillary tubes, in which the capillary pressure is determined by applying the Young-Laplace equation and flow path tortuosity via a tortuosity factor.

The viscous coupling model, based on pipe flow, suggests deviation from linearity in two-phase relative permeabilities, arising from the interference between phases with a high viscosity contrast, such that (Fourar and Bories, 1995; Fourar and Lenormand, 1998):

$$k_{r,w} = \frac{S_w^2}{2}(3 - S_w) \tag{30}$$

$$k_{r,nw} = (1 - S_w)^3 + \frac{3}{2}\frac{\mu_{v,nw}}{\mu_{v,w}}S_w(1 - S_w)(2 - S_w) \tag{31}$$

This model has been shown to agree with experimentally obtained relative permeabilities in smooth-walled fractures (Chen and Horne, 2006). The Corey model, which is generally used for two-phase matrix flow, predicts phase interference in fractures arising from capillary pressure effects, rather than viscosity effects, such that (Corey, 1954; Diomampo, 2001):

$$k_{r,w} = \left(\frac{S_w - S_{w,r}}{1 - S_{w,r} - S_{nw,r}}\right)^4 \tag{32}$$

$$k_{r,nw} = \left(1 - \frac{S_w - S_{w,r}}{1 - S_{w,r} - S_{nw,r}}\right)^2\left(1 - \left(\frac{S_w - S_{w,r}}{1 - S_{w,r} - S_{nw,r}}\right)^2\right) \tag{33}$$

where $S_w = 1 - S_{nw}$, which has been used successfully in the interpretation of capillary pressure-saturation relationships in rock fractures (Reitsma and Kueper, 1994).

These three different models have been verified using experiments on smooth parallel plates, and, as such, are probably not applicable to naturally rough variable-aperture fractures, which have log-normal or (truncated) Gaussian aperture distributions (Mo and Li, 2019). For example, two-phase flow experiments involving natural rock fractures have shown that wetting and non-wetting phase relative permeabilities are much smaller at intermediate saturations than those obtained with the X, viscosity and Corey models (Persoff and Pruess, 1995). This suggests that flow behaviour not captured by those models exists. For example, Pruess and Tsang (1990) performed a theoretical and numerical study of two-phase flow in fractures in a 2D porous medium and demonstrated that non-wetting phase occupancy of small apertures significantly reduced the relative permeabilities at intermediate phase saturations, and showed much stronger interference between phases than the Corey model (Figs. 7 and 8). In order to account for the limited phase mobility at intermediate saturations, Watanabe et al. (2015) proposed a new V-type (semi-)empirical relative permeability model:
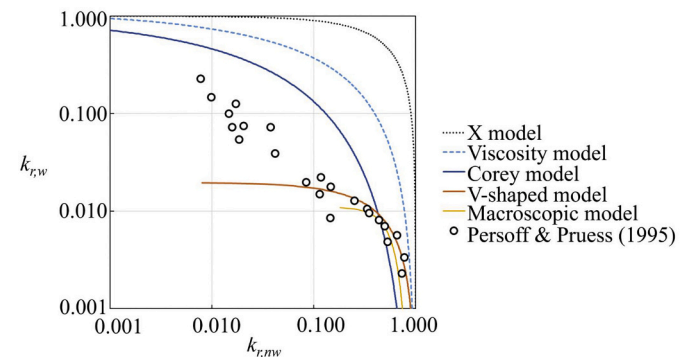

Fig. 8. Cross plot of nitrogen gas-water relative permeabilities in a single rough fracture computed using the X, viscosity, Corey and V-models, for a water-wet system compared to the experimental data of Persoff and Pruess (1995).

$$k_{r,w} = \left(\frac{S_w - S_{w,r}}{1 - S_{w,r}}\right)^4 \tag{34}$$

$$k_{r,w} = 1 - \left(\frac{S_w}{1 - S_{nw,r}}\right)^3 \tag{35}$$

This model replicates the non-wetting phase permeability behaviour but tends to underestimate wetting phase permeability at high wetting phase saturations (e.g. Fig. 7). Of the developed microscopic models, only the V-type model adequately satisfies the two-phase relative permeability behaviour observed in fractured media influenced by capillarity (Fig. 8) (Ye et al., 2017). However, the constitutive equations are limited in terms of predicting two-phase flow across a broad range of fracture heterogeneity, and consequently the upscaling of two-phase flow from the single fracture scale to the continuum scale remains challenging (Ye et al., 2015).

5.2.2. Macroscopic relative permeability models

The macroscopic approach differs from the microscopic approach in that it links directly macro hydraulic conductivity from Darcy's law, where both the wetting and non-wetting phases are treated as a continuous constituent stretched over the total surface of the flow domain (Mualem, 1978). The macroscopic model describes the power-law relationships between relative permeability and saturation for the wetting and non-wetting phases as:

$$k_{r,w} = S_{we}^{\eta} \tag{36}$$

$$k_{r,w} = S_{nwe}^{\eta} \tag{37}$$

where S_{we} and S_{nwe} are the effective saturations for the wetting and non-wetting phase, respectively:
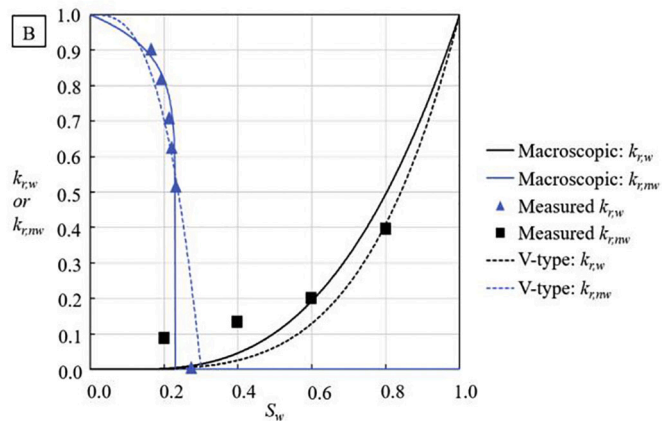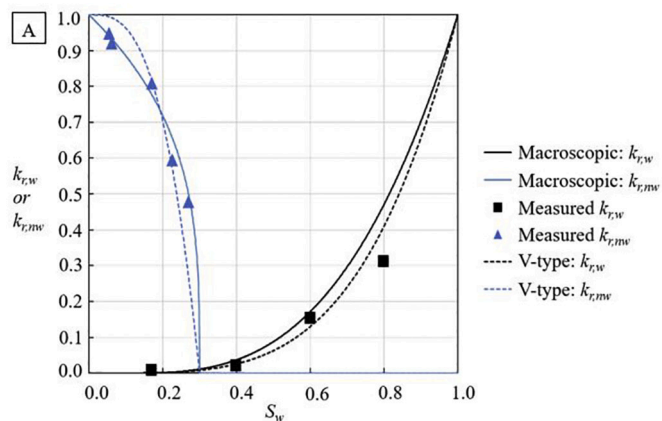

Fig. 9. Experimentally derived relative permeably of water-nitrogen in (A) Granite and (B) Limestone at an effective confining stress of 1 MPa (Watanabe et al., 2015), compared to the macroscopic and V-type models.

$$S_{we} = \frac{S_w - S_{wr}}{S_{ws} - S_{wr}} \tag{38}$$

$$S_{nwe} = \frac{S_{nw} - S_{nwr}}{S_{nws} - S_{nwr}} \tag{39}$$

The value of η is sensitive to flow path tortuosity and the spatial correlation of apertures. When η is equal to 1 the model is equivalent to the X model, with values of η being obtained from experiments or numerical simulation. The macroscopic model has been found to best approximate fracture relative permeability behaviour derived from experiments and simulations (Ye et al., 2017) (Fig. 9).

5.3. Numerical studies

Many studies have used numerical simulations to estimate fracture relative permeability behaviour. These approaches can be broadly grouped into continuum (Murphy and Thomson, 1993; Watanabe et al., 2015; Yang et al., 2012; Yang et al., 2013; Ye et al., 2017), invasion-percolation (Glass et al., 1998; Glass et al., 2003; Yang et al., 2013; Ye et al., 2017) and pore network (Ferer et al., 2011; Hughes and Blunt, 2001; Karpyn and Piri, 2007) models. Continuum models have some advantages over invasion-percolation models (Yang et al., 2013):

i. They consider viscous forces, which is essential when the capillary number is large;
ii. They realistically capture the invading sequence of two-phase flow once the cells' entry pressures are exceeded and when the internal cells connect to the invading phase, whilst in invasion-percolation models, the invading phase sequentially invades the cells only according to the order of their entry pressures;
iii. Solving the governing equations in a continuum model is conceptually identical to a pore-network model since both are based on mass conservation and the pore throats' (or cells) hydraulic conductivity, estimated using the LCL.

For example, Watanabe et al. (2015) used numerical fracture flow simulations of nitrogen-water and decane-water flows in rough fractures to estimate both the phase saturations in their two-phase fracture flow experiments and to numerically derive capillary pressure and relative permeability curves. Their simulations modelled Darcy flow through rough fractures, assuming that local fracture permeability and two-phase relative permeability could be described using the LCL and X-type relative permeability models, respectively, with phase invasion controlled by a local capillarity term ($P_c = (2\gamma \cos \theta)/a$) in each grid block, based on the Young-Laplace equation and local fracture aperture (Fig. 10). The simulation results showed good agreement to experimentally derived capillary pressure and relative permeability curves. Similarly, Wang and Cardenas (2018) used a 2D continuum model to simulate CO_2 drainage in rough fractures, to numerically derive constitutive models for two-phase fracture flow and to numerically examine the influence of fracture roughness and correlation length scale on the empirical parameters of upscaled van-Genuchten capillary pressure and V-type relative permeability models (Wang and Cardenas, 2018). Yang et al. (2019b) used a 2D continuum modelling approach to examine emergent fluid invasion patterns in rough fractures and the transition from capillary to viscous fingering regimes, including the effect of in-plane interface curvature on capillary entry pressure previously neglected in other studies. Their results compared favourably to experimentally determined drainage patterns in rough fractures.

5.4. Implications for predictions of fluid flow rates in fractured caprocks

- The significant gaps identified in our understanding of, and ability to model, multiphase fluid flow in rough fractures and fracture networks hinder our ability to predict fluid leakage rates through
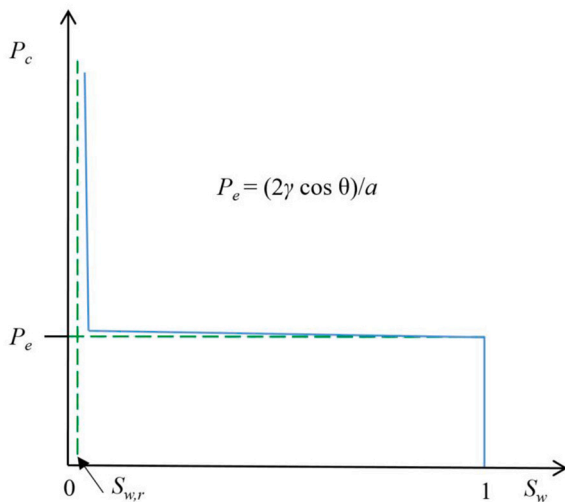
Fig. 10. Illustration of the grid block scale capillary pressure-saturation function (redrawn after Yang et al. (2013)), typically used in continuum models of two-phase rough fracture flow (Wang and Cardenas, 2018; Watanabe et al., 2015; Yang et al., 2019b; Yang et al., 2012; Yang et al., 2013). An entry pressure (P_e) is defined for each element, depending on the local aperture (a), contact angle (θ), and interfacial tension (γ). This relationship is composed of three straight lines connecting from $S_w = 1$ to $S_w = S_{w,\,r}$, capturing the rapid decrease in S_w of an element to $S_{w,\,r}$ once the entry pressure for the element is exceeded. To ensure P_c is a monotonic function of S_w, a small slope of 0.001 is assigned for the middle line, while a slope of 1000 is assigned for the other two lines.

fractured caprocks. An improved understanding of the nature of two-phase flows, and phase interference, at a range of length scales, is required if accurate modelling and upscaling techniques are to be developed.

- The commonality of two-phase flow in fractures has motivated several numerical studies, but only a limited number of experimental studies. Enhancing the validity of simulating such behaviour on a variety of spatial and temporal scales requires systematic experimental investigation of the governing physical forces that may impact predicted flow properties.

6. Mechanical properties of fractures and their link to flow

6.1. Effect of stress on single(-phase) fracture permeability and aperture

In the subsurface, confining stresses reduce fracture aperture. The degree of aperture reduction arises from a complex interplay between fracture surface topography, mechanical and chemical properties of the fracture and matrix, fracture orientation relative to the principal stress directions, effective stresses and stress shadowing (Laubach et al., 2004; Olson et al., 2007; Olsson and Barton, 2001; Yang et al., 2019a).

Fracture orientation in relation to the stress field acting upon the rock may promote increased coupling between fracture walls and fluid flow, thereby altering the underlying mechanics of the fractures (Boutt et al., 2006; Lei et al., 2017; Stephanson et al., 1997). Fracture apertures may alter due to normal stress-induced closures or openings and shear-induced dilations. Fractures aligned subparallel to the maximum principal compressive stress (σ_1) are near-critically stressed and therefore exhibit the greatest affinity to slip, dilate and increase permeability (Gan and Elsworth, 2016; Heffer and Lean, 1993). This process is based upon assumptions that fractures subjected to the least amount of stress will offer the least resistance to flow. Fractures oriented normal to σ_1 undergo compaction and permeability reduction. However, studies utilising core permeability and static stress measurements indicated that at depths of > 3 kilometres, open fractures were not aligned

parallel to σ_1 (Laubach et al., 2004). This suggests that *in-situ* stress orientations alone may not be a reliable indicator when predicting fluid flow directions and pathways in fractured rock. Permeability preservation within rough fractures undergoing contact stresses across the fracture plane may be attributed to the microscopic structure and roughness of the fracture surfaces (Cuss et al., 2011). It is stipulated that even in the presence of excessive loading exceeding the strength of the sediment matrix, microscopic asperities associated with the fracture surface maintain sufficient space and channels along the fracture that enable fluid flow through these enhanced permeability pathways (Cuss et al., 2011; Ilgen et al., 2017).

6.1.1. Microscopic aperture distribution

Despite both experimental (e.g. Brown et al., 1998; Indraratna et al., 2015; Scesi and Gattinoni, 2007) and numerical studies (e.g. Auradou, 2009; Xie et al., 2015; Zimmerman and Bodvarsson, 1996) demonstrating the sensitivity of fluid transport to aperture distribution, data on, and methods to reconstruct, *in-situ* fracture aperture distributions are somewhat lacking. Stress relaxation during uplift, and, particularly in mudrocks, weathering processes can make the systematic measurement of *in-situ* aperture distribution challenging. However, despite a significant lack of such data sets, studies have demonstrated that reliable aperture size data can be acquired, for example, from quarry exposures (Gale et al., 2014). Aperture distributions derived from high-quality image logs are generally overestimated due to uncertainties in the spatial variability and statistical distributions of fracture characteristics, and can only provide a 1D view of aperture in an inherently 3D environment (Bisdom et al., 2016; Bisdom et al., 2017; Botros et al., 2008). Therefore, reconstruction of *in-situ* aperture distributions is typically related to simple measurable quantities or reconciled via modelling.

Models resolving the hydraulic and mechanical effects (e.g. asperity interaction and aperture constriction) on the microscopic scale have been developed. Mechanical models of rough fractures typically represent roughness as either collections of asperities (Fig. 11a) or cracks (Fig. 11b). In asperity-based models, the fracture is approximated by a slab with columns of different height, mimicking aperture distribution, in either 1- or 2D, and the number of contacting asperities and their elastic deformation are evaluated. Asperity-based models commonly use Hertzian contact mechanics to describe rough rock fracture deformation under stress (e.g. Gangi, 1978), or the Boussinesq solution (Pyrak-Nolte and Morris, 2000) that considers the deformation of the supporting half-space, with a potential lateral offset (Detwiler and Morris, 2014). Tsang and Witherspoon (1981) more realistically described void deformation in between the asperities rather than deformation of the asperities themselves. Walsh (1981) applied Hertzian contact theory to the asperities, first modelling the fracture by two
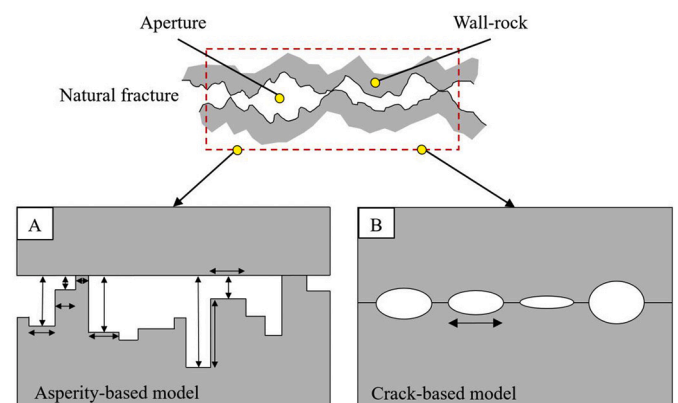

Fig. 11. Common representations of rough fracture surfaces in fracture flow models (modified after Tsang and Witherspoon (1981). (A) Asperity-based models. (B) Crack-based models.
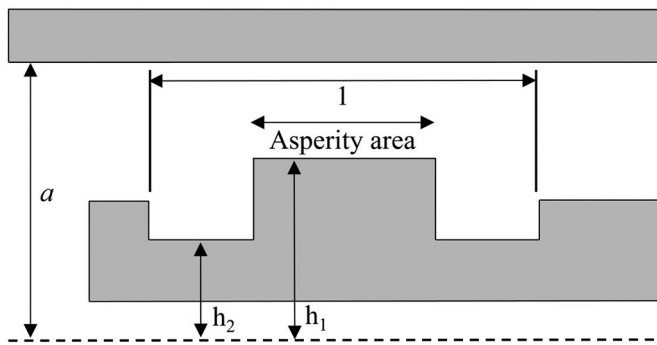
Fig. 12. Radially symmetric fundamental unit (redrawn after Walsh et al. (1997)), where the fundamental unit area is 1. Valley and asperity heights (h_1 & h_2) and aperture (a) are measured relative to an arbitrary reference.

uncorrelated rough surfaces with random topography of exponential distribution, and later extending the model for consideration of a spatial correlation of the asperity heights (Walsh et al., 1997). The same authors employed effective medium theory based on a fundamental unit, as shown in Fig. 12. This enabled retention of the statistical distribution of asperity heights below the correlation length, while at the same time introducing the short-range order required in the effective medium theories. Assuming a fractal surface topography and random aperture distributions, fluid channelisation was observed at small apertures.

Crack-based models often focus on the mechanical problem of fracture closure under stress. Variable crack sizes are considered by integrating over the reference solution evaluated for the different sizes and weighted with the respective volume fraction. Myer (2000) used a strain energy approach to correct for the excess deformation resulting from interaction within collections of cracks. Zimmerman (2008) included the effect of complete crack closure and linked the mechanical model to a hydraulic model for determining effective fracture permeability. For the latter, the CL was applied to the individual fluid channels in each crack with stress-dependent crack apertures. Lemarchand et al. (2010) utilised effective medium theory to determine both fracture closure under stress and the resulting effective permeability, adopting a crack-based approach assuming cracks of spheroidal shape. In contrast to the common cylindrical crack models, this enables consideration of, in a simplified manner, tortuosity and the lack of continuous flow channels in the fracture.

6.1.2. Fracture contact area

The contact area relative to the total surface area governs fracture aperture distribution, which is, in turn, a function of the specific

stiffness (k_n) of a fracture, describing the ratio of the increment of stress to the increment of displacement (Pyrak-Nolte and Morris, 2000). The relationship between specific stiffness, normal stress and aperture have been experimentally measured by Bandis et al. (1983), from which a linear function is proposed as:

$$k_n = J\sigma_n \tag{40}$$

where J serves as a fitting coefficient (discussed by Wang and Cardenas, 2016), showing that fractures which have undergone larger displacements for a specific stress increment have larger apertures. Specific stiffness is affected by the rate of discrete contact area formation from the resulting increase in normal stress (Zimmerman et al., 1990). Previous investigation into fracture specific stiffness have incorporated surface roughness measurements, and numerical and theoretical characterisation of asperity deformations to confirm that specific stiffness and fluid transmissivity is intimately linked to the spatial correlation of the aperture distribution (e.g. Bandis et al., 1983; Brown and Scholz, 1985; Brown and Scholz, 1986; Cook, 1992; Swan, 1983). Surfaces exhibiting the same amount of contact area, but with varying spatial distributions will display different specific stiffness values (Hopkins et al., 1990).

6.1.3. Experimental observations of fracture stress-permeability relationships

Experimental data from flow experiments on the permeability of individual fractures in mudrock core plugs are shown in Fig. 13. One of the Carmel datasets (Carmel 1, Fig. 4a) is previously unpublished, with details of the experimental setup given in the appendix (Appendix B). For the effective stress range investigated across all studies (up to approximately 40 MPa), a permeability reduction of between one to three orders of magnitude is observed. Direct comparison between the studies is difficult due to differences in sample mineralogy, fracture surface roughness, experimental setup, and fluid type (gas/water) used to measure permeability. Generally, permeabilities measured using water as the permeating fluid are lower than those measured using gas. This is primarily attributed to slip flow (Klinkenberg phenomenon) and whether or not certain wall-rock minerals react with the permeating fluid (e.g. swelling of clay minerals). Detailed discussions on these topics can be found in the following studies and references therein (Busch et al., 2016; Busch et al., 2020; Fink et al., 2017; Foster, 1954; Heller et al., 2014; Klinkenberg, 1941; Zhang et al., 2018).

The data presented in Fig. 13 represent the bulk permeabilities of each core plug, at given effective stress conditions, which therefore includes contributions to flow from both the fracture and matrix. For most mudrocks, flow is largely governed by the fracture due to low matrix permeabilities. Using the method described by Zhang (2011) and Zhang (2013), it is possible to calculate fracture conductivity
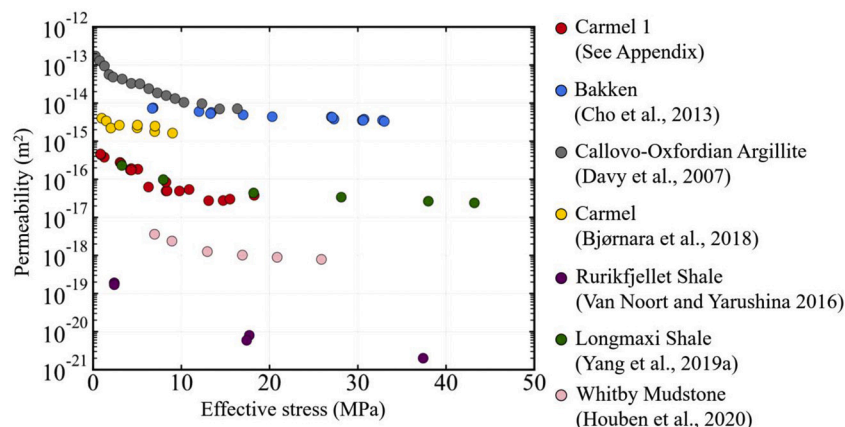

Fig. 13. Single-phase permeability data of mudrock samples containing a single through-going fracture as a function of effective stress.

($K_{fracture}$) using the bulk permeability measurement (k_{bulk}), such that:

$$k_{bulk} = k_{matrix} + K_{fracture} = k_{matrix} + \frac{F}{12}(e_m - a_c)^3 \qquad (41)$$

where k_{matrix} is the matrix permeability, a_c is the critical aperture, and F is a geometric parameter related to the sample dimensions:

$$F = \frac{4}{\pi d} \qquad (42)$$

where d is the core plug diameter. For mudrocks, matrix permeabilities are typically of the order $10^{-19} – 10^{-21}$ m^2 (Ross and Bustin, 2009). The subsequent geometric (mechanical) aperture can be calculated using:

$$e_m = b_m - \Delta a \qquad (43)$$

where b_m the initial unstressed aperture and Δa is approximated as:

$$\Delta a = b_m (1 - e^{- \sigma' Z}) \qquad (44)$$

where $\acute{y}$ and Z are constants. If k_{matrix}, d and σ' are known then the values of a_c, b_m, $\acute{y}$ and Z can be obtained by fitting of bulk permeability data, and the fracture permeability can be estimated. Utilising this approach, the bulk permeability data shown in Fig. 13 have been converted into fracture permeability, presented in Fig. 14.
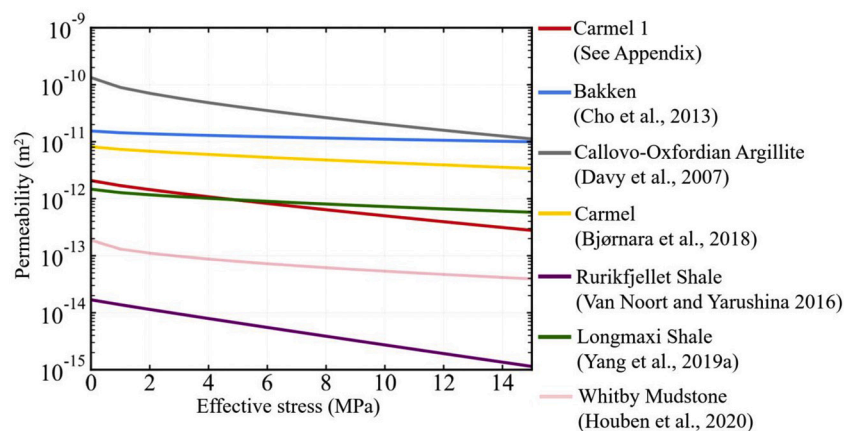
rough fractures have been developed (see de Dreuzy et al., 2012; McDermott and Kolditz, 2006; Unger and Mase, 1993).

6.2. Effect of stress on fracture network permeability

In fractured media with very low matrix permeabilities (e.g. mudrocks), fracture geometry and connectivity, describing the number of intersections per fracture, is a first-order determinant of flow initiation and transport (de Dreuzy et al., 2000; Huang et al., 2018; Koudina et al., 1998; Long and Billaux, 1987; Sanderson and Nixon, 2018; Tsang and Tsang, 1987). Fracture connectivity is a complex function of fracture density, orientations, length and topology (e.g. cross-cutting relations). Densely fractured media are not always well-connected, with other geometric properties playing an equally important role in determining network connectivity (Long and Billaux, 1987). As fracture length distributions typically follow a power-law relation, fractures equivalent to the size of the system may enable system-wide connection at all scales (de Dreuzy et al., 2000).

Realistic representation of the fracture networks response to stress requires solution of the associated fracture and solid mechanics with respect to complex boundary conditions (Jing, 2003). The coupling of stress and deformation is notoriously challenging to predict in complex fracture networks, and so is, consequently, the hydraulic response (Baghbanan and Jing, 2008; Koh et al., 2011; Min et al., 2004; Rutqvist

Fig. 14. Fracture permeability of mudrock samples as a function of effective stress, calculated using the method described by Zhang (2011) and Zhang (2013). This is based upon the core plug permeabilities presented in Fig. 13.

6.1.4. Empirical, analytical and numerical models of fracture contact mechanics

Several additional empirical relationships have also been proposed to describe the influence of stress on the effective aperture of a single fracture. For example, Zoback (2010) specified the equivalent relation for an elliptical cross-section of a fracture with maximum opening (a_{max}) and fracture length (L) under consideration of stress influences using Linear Elastic Fracture Mechanics as:

$$a_{max} = \frac{2(P_p - S_{h,min})L(1 - v^2)}{E} \qquad (45)$$

This allows consideration of the interplay between pore pressure and minimum horizontal stress ($S_{h, min}$), which is assumed to act orthogonally to the fracture surface. The permeability then depends on the rocks elastic properties, namely Poisson's ratio (v) and Young's modulus (E), such that:

$$k^F = \frac{\pi}{8} \left[\frac{(1 - v^2)}{E} L(P_p - S_{h,min}) \right]^3 \qquad (46)$$

where the aperture is the term in angular brackets. A number of (semi-)analytical and numerical models to describe stress-dependent flow in

and Stephansson, 2003). Reliable observations of the resulting anisotropic permeability response are best obtained from field experiments (Rutqvist, 2015). This is not without its own challenges related to observational dimensions (e.g. 1D borehole logging or 2D outcrop mapping of a 3D world) and length scales (Einstein and Baecher, 1983; Latham et al., 2013; Riedel et al., 2010). Even modern 3- and 4D seismic data acquisition and advanced micro-seismic methods lack the capabilities to resolve sub-seismic fractures and associated networks (e.g. Reston and McDermott, 2014). Therefore, generating predictive models relies upon extrapolations inferred to the entire study domain from limited datasets (Adler and Thovert, 1999; Dershowitz and Fidelibus, 1999).

6.2.1. Predictability of fracture network geometry and fluid flow

Characterisation of stress fields is of paramount importance when determining how faults and fracture networks interact with one another, accommodate slip, concentrate and redistribute stress, and deform the surrounding rock (Maerten et al., 2014). Typical 2D numerical solutions represent faults and fractures as dislocations (discontinuities) embedded in isotropic linear-elastic materials using a boundary element method (BEM) (e.g. Bilham and King, 1989; Crouch and Starfield,

1983; Dee et al., 2007; Olson and Pollard, 1991; Sempere and Macdonald, 1986; Wu and Pollard, 1995). BEM models do not require the discretised description of the medium, but rather utilise spatial information of existing discontinuities within the medium, such as faults (Dee et al., 2007). Through assuming that a dominant control on small-scale fracturing is strain perturbations occurring in the vicinity of larger (seismically resolvable) faults, a geomechanical approach can be adopted to predict the likely distribution of subsurface strain, and hence the intensity and nature of tensile and shear fracture networks (Bourne et al., 2000; Bourne and Willemse, 2001; Maerten et al., 2002). Models utilising the orientation and magnitude of strain to calculate stress fields perturbed by large-scale structures have been combined with rock failure criteria (e.g. Fig. 3) to model natural fracture network characteristics (e.g. Bourne et al., 2000; Bourne and Willemse, 2001; Davatzes et al., 2005; Kattenhorn et al., 2000; Maerten et al., 2006; Maerten et al., 2002). In addition to the enhanced predictability of this approach, elastic dislocations are commonly used to represent stress perturbations in idealised geomechanical models due to their computational simplicity and ability to adequately characterise deformation observed in nature (Maerten et al., 2014). 3D numerical solutions to model elastic stress fields in systems with complex discontinuities include *Poly3D* (Thomas, 1993) and *iBem3D* (Jeyakumaran et al., 1992). Maerten et al. (2014) provide a comprehensive review of the functionalities and theory behind each method.

Deformation of fractured rock in response to stress perturbations (natural or induced), involving the modification of existing surfaces and the generation of new fractures, leads to alterations in bulk permeability and fluid migration potential (Rutqvist and Stephansson, 2003). Fracture mechanical response, initiation, and propagation is strongly influenced by mechanical interactions between neighbouring fractures, leading to hydromechanical phenomena which modify permeability, such as stress relaxation or redistribution (Cruikshank et al., 1991; Lamarche et al., 2018; Thomas and Pollard, 1993). Progressive deformation may further promote fracture interaction, such as hooking of subparallel fractures (underlapping, overlapping, or linkage) (Lamarche et al., 2018; Laubach et al., 2018), hindrance of fracture propagation in the direction of existing fractures through stress reduction shadows (Ackermann and Schlische, 1997; Bai and Pollard, 2000; Nagel et al., 2013), and fracture arrest or reorientation under stress perturbations (Rawnsley et al., 1992). Increased network connectivity resulting from brittle failure and crack propagation via mechanical loading may also increase the conductivity of fractured rocks (Figueiredo et al., 2015; Latham et al., 2013; Renshaw and Park, 1997). Under high differential stress regimes, the influence of dilational jogs or bends may further increase permeability (Sanderson and Zhang, 1999). Despite these avenues for increased conductivity through enhanced fracture connectivity, it is important to note that in extensional regimes, for example, increased fracture density does not always translate into higher network permeability, as fractures tend to close when they are too densely spaced (e.g. Bai and Pollard, 2000) or due to stress differential redistribution effects around the fracture opening (Read, 2004). However, flow has been demonstrated to occur on engineering timescales in fracture networks even if the rock contains fracture networks that are not fully interconnected (Philip et al., 2005).

6.3. Impact of shear and deformation on flow properties

Shearing existing rough fracture surfaces forces opposing asperities to slide over one another, leading to surface reorganisation and destruction of bridging asperities that significantly alter the flow properties through either dilation (increased conductivity; Fig. 15b, d) or the progressive formation of gouge (decreased conductivity; 15f) (Barton et al., 1985; Crandall et al., 2017; Elsworth and Goodman, 1986; Esaki et al., 1999; Faoro et al., 2009; Gentier et al., 1997; Ishibashi et al., 2016; Lee and Cho, 2002; Makurat et al., 1997; Nemoto et al., 2009; Olsson and Barton, 2001; Xiong et al., 2011; Zimmerman

and Bodvarsson, 1996). To determine the relationship between shearing and fracture conductivity, stress relationships must be considered in all three spatial dimensions; (i) within the fracture plane in the direction of shear; (ii) perpendicular to the shear, and; (iii) perpendicular to the fracture.

Shear dilation represents the dilation of a fracture produced by shear displacement along a non-planar fracture plane, resulting in disturbances in fracture geometry and characteristics, including the contact ratio, roughness, and matedness (Fang et al., 2018; Mo and Li, 2019; Olsson and Brown, 1993; Poon et al., 1992; Schmittbuhl et al., 1995; Sharifzadeh et al., 2008). Resulting mechanical and hydraulic aperture modifications produce direct hydromechanical couplings, for example; (i) solid-to-fluid coupling, resulting from changes in applied stress altering fluid pressure and/or mass due to dissolution or precipitation, and; (ii) fluid-to-solid coupling, resulting from changing fluid pressure/mass modifying the bulk volume of the porous medium and thus the degree of compaction a rock may undergo (Wang and Park, 2002). Both forms of direct coupling lead to a reduction in the available cross-sectional area to flow, resulting in lower flow capacities (Huang et al., 2018; Rutqvist and Stephansson, 2003). Such processes are notoriously challenging to forecast, owing to formation-specific mechanical and hydraulic interactions exhibiting high sensitivity to discrete aperture alterations (Koh et al., 2011; Min et al., 2004). Ultimately, increasing shear displacement increases both the mean and standard deviation of the aperture (i.e. alteration in the relative roughness) (Frash et al., 2017; Wang et al., 2019; Yeo et al., 1998). Additionally, enhanced void space nucleation through aperture dilation has been shown to form channels aligning perpendicular to the shear direction, altering permeability by up to two orders of magnitude (Council et al., 1996; Esaki et al., 1991; Gale, 1990; Liu et al., 2020; Yeo et al., 1998).

Fracture aperture alterations due to changes in σ_n' and shear displacement may be considered by modifying e_m. As an example, the widely used empirical formulation by Barton et al. (1985) defines fracture closure in normal direction as:

$$\Delta a = \frac{\sigma_n'}{c_n + \sigma_n'/\Delta a_{c,max}} \tag{47}$$

where $\Delta a_{c,\ max}$ denotes maximum normal closure and c_n describes normal stiffness at zero stress intercept, where $\Delta a_{c,\ max}$ and c_n can be estimated from the Barton-Bandis joint parameters, namely the *JRC* (Eq. (10)) and the joint compressive stress (*JCS*). In case of un-weathered fractures, *JCS* equals the unconfined compressive strength of the rock (Barton, 2013).

An empirical relation for aperture change in consequence of dilation (Δa_s), proposed by Barton et al. (1985), reads as:

$$\Delta a_s = \Delta u_s \ tan \ \theta_{mob} \tag{48}$$

where θ_{mob} denotes the mobilised dilation angle following from:

$$\theta_{mob} = \frac{1}{2} JRC_{mob} log_{10} \left(\frac{JCS}{\sigma_n'} \right) \tag{49}$$

The index '*mob*' for '*mobilised*' indicates quantities that are evaluated at the current displacement and stress state. Subtracting the dilation according to Eq. (48) from the normal closure specified by Eq. (47) yields the total aperture change. This is added to the e_m before its conversion to e_h following Eq. (9), recognising from experimental data that the dilation relation breaks down after reaching peak shear stress ($u_{s,\ peak}$) (Olsson and Barton, 2001). At larger shear displacements, aperture starts to decrease again via asperity damage and formation of gouge. For this reason, the application range of the classical Barton equation (Eq. (9)) is limited to shear displacements of at most 75% of the displacement at $u_{s,\ peak}$. The latter can be estimated from (Asadollahi et al., 2010):
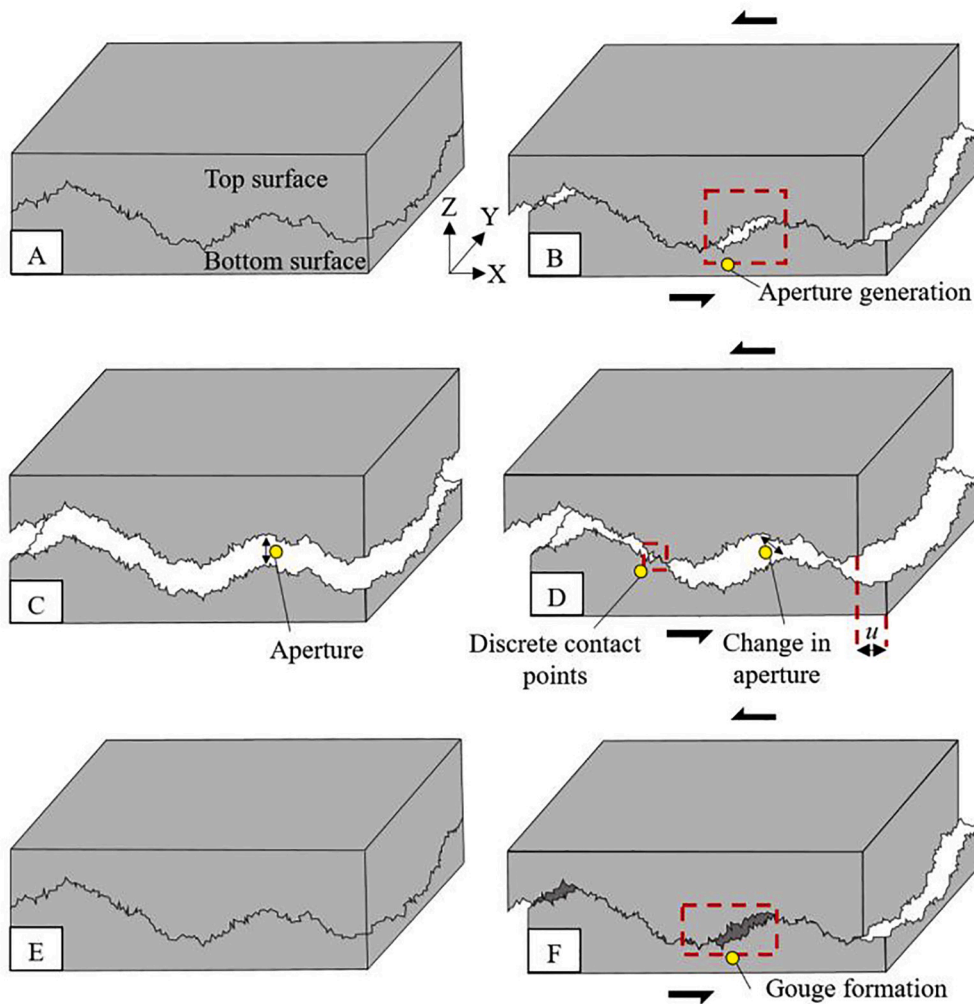
Fig. 15. 3D schematic representations of opposing rough fracture surfaces (modified after Plouraboue et al. (2000)). (A) Mated fracture surfaces. (B) Shear dilation of A leads to aperture generation. (C) Opposing fracture surfaces with aperture before shear displacement. (D) Shear displacement of C results in aperture alteration. Shear displacement modifies aperture and thus permeability as surfaces slip. *u*: amplitude of shear. (E) Mated fracture surfaces before shear deformation. (F) Formation of fine-grained, permeability-decreasing material (e.g. gouge) produced through the destruction and reorganisation of fracture wall asperities during shear deformation of E.

$$u_{s,peak} = \frac{L}{500}\left(\frac{JRC}{L}\right)^{0.33} \tag{50}$$

At shear displacements higher than $u_{s,\,peak}$, fracture wall geometries change with increasing shear displacement, therefore an alternative relation between e_m and e_h is recommended (Olsson and Barton, 2001):

$$e_h = \sqrt{e_m}\,JRC_{mob.} \tag{51}$$

Finally, linear interpolation between the apertures is suggested for $0.75 \le u_s/u_{s,\,peak} \le 1$.

6.3.1. Experimental observations of shear-dependent permeability relationships

In-situ field well studies have shown that fractures exhibiting a stress state close to the failure criterion have a higher likelihood to be conductive due to localised failure as a direct consequence of a large shear component acting along the fracture surface (Barton et al., 1995; Ito and Zoback, 2000). It has also been shown that fractures totally misoriented to the current stress field can profoundly enhance fluid flow (Laubach, 2003; Laubach et al., 2016). Field studies conducted by Rogers (2003) indicate an affinity for these fractures to orientate approximately 30° to the σ_1 direction (i.e. critically stressed fractures). Barton et al. (1985) demonstrated through coupled experimental and numerical studies that under normal stress (σ_n) conditions high enough to produce asperity failure during shear, conductivity, may decrease, with this relationship becoming more pronounced with higher degrees of roughness (Mokhtari et al., 2015). Previous numerical studies predict the pronounced effect of surface roughness on shear strength for

moderately low normal stresses (Huang et al., 2018; Huang et al., 2002). An experimental study at low normal stresses ($\sigma_n/\sigma_c = 6 \times 10^{-4}$) confirms this prediction, demonstrating that shearing occurs via overriding the asperities (Grasselli, 2006). Increasing the normal stress ($\sigma_n/\sigma_c = 1.5 \times 10^{-2}$) led to the shearing of asperities, which completely replaces dilation at sufficiently high values of normal stress. These results highlight the role of surface morphology, whereby resistance to shearing decreases with an increased normal load.

The permeability evolution of the Utica shale (40 % clay content) was investigated upon failure in either compression or direct shear experiments under low confining pressures (3.45 MPa and 11.7 MPa; Carey et al. (2015)) and higher confining pressures (up to 22 MPa; Frash et al. (2016)) to more accurately reflect subsurface conditions. Carey et al. (2015) found that the effects of shear were strongly dependent on the orientation of the bedding planes relative to the loading direction and highlights the impact high-stress environments exert over the stimulation of permeability through shear displacement. For example, the apparent permeability of a sample tested at 22 MPa exhibited < 0.1 order of magnitude permeability increase, while similar experiments conducted on the same Utica shale material yielded an apparent permeability increase of up to four orders of magnitude at 3.4 MPa confining stress. Frash et al. (2017) conducted shearing experiments, similar to those conducted by Bakker et al. (2016) on simulated fault gouges, with the carbonate-rich (65.8%) Marcellus shale at a range of *in-situ* stress conditions (2.8–29.3 MPa; Fig. 16a). This experimental setup allowed for simultaneous permeability measurements during shear displacement, with findings indicating that the critical effective stress where dilatant behaviour transitions to compactive
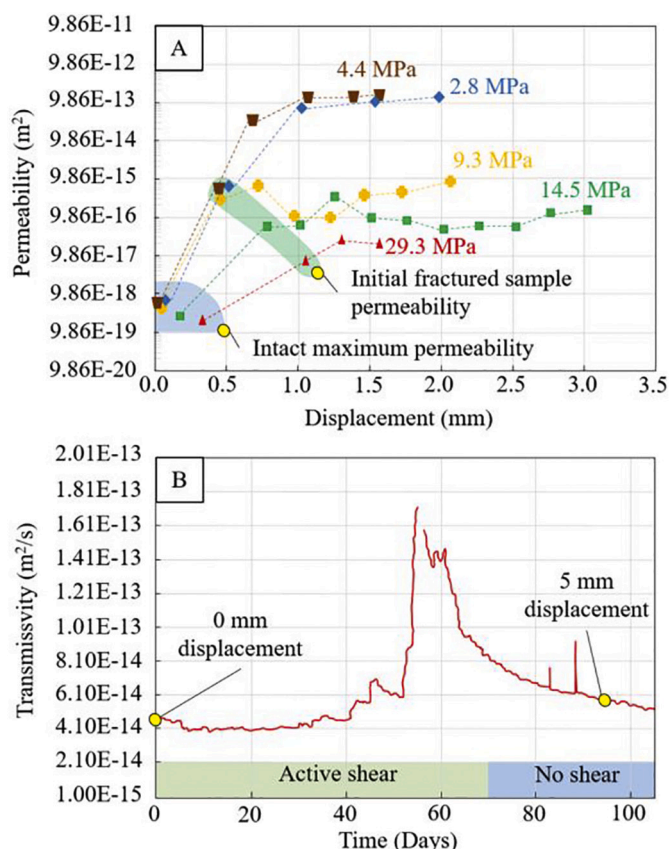
Fig. 16. (A) Permeability evolution of five separate Marcellus shale samples as a function of continued shear displacement, reproduced from Frash et al. (2017). Each fracture through the individual samples were created at a peak direct-shear stress (2.8 MPa effective confining stress, 27.5 MPa peak direct-shear stress; 4.4 MPa effective confining stress, 30.4 MPa peak direct-shear stress; 9.3 MPa effective confining stress, 44.8 MPa peak direct-shear stress; 14.5 MPa effective confining stress, 52.3 MPa peak direct-shear stress, 29.3 MPa effective confining stress, 71.2 MPa peak direct-shear stress). Each sample was sheared to an assigned maximum displacement, with the intact maximum permeability (blue region) and the initial fractured sample permeability (green region) measured for each sample. (B) Fracture transmissivity of the Opalinus clay during active shear at a constant normal load and single strain rate, reproduced from Cuss et al. (2011). The example shown illustrates a sample being actively sheared for 70 days, with the final 35 days conducted without shear.

behaviour appears in the range 14.5-29.3 MPa (Fig. 16a). Permeability decreased with time post-fracturing, indicating the presence of creep deformation through the relaxation of peaks at the fracture asperities. Such findings indicate that some existing natural fractures are likely sealing, however, have the potential to be conductive through re-activation. Cuss et al. (2011) conducted similar experiments to understand fracture transmissivity evolution with shear displacement in the Opalinus clay (40-80% clay content) (Fig. 16b), finding that permeability begins altering significantly after peak shear stress has been reached, with self-healing (i.e. clay smearing) reversing initially increasing permeability trends, even at higher displacements. Further experiments investigating the dilational effects and permeability evolution resulting from shear displacement (e.g. Gutierrez et al., 2000; Makurat et al., 1997) indicate permeability enhancement at low effective stresses and permeability reduction at higher effective stresses which exceed the unconfined compressive strength (σ_c) of the rock. Differences in permeability with varying rates of shear displacement in each of the aforementioned studies are likely a combination of; (i)

distance over which the sample was sheared (longer shearing produces smoother fracture surfaces); (ii) initial surface roughness before shear; (iii) initial mode of deformation before enhanced shear, and; (iv) the contribution of varying mineralogy to gouge formation, asperity failure, and the transport of particles that occlude flow channels.

6.4. Implications for predictions of fluid flow rates in fractured caprocks

- Despite fairly extensive experimental testing of rock fracture permeability, uncertainty in the nature and controls on stress-permeability coupling still exist (Carey et al., 2015). Questions remain about the role of deformation in the evolution of the permeability response, the nature of deformation (e.g. asperity crushing, elastic versus plastic deformation), and the importance of local (e.g. asperity) and global (e.g. rock mass) mechanical response (Anders et al., 2014; Fang et al., 2017; Liu, 2005; Walsh et al., 2008; Wang and Cardenas, 2016; Yasuhara et al., 2011; Zhang et al., 2007). Order of magnitude indications of fracture permeability from laboratory-scale measurements are a required input to guide and constrain numerical models, but translating this to the field-scale via complex upscaling schemes remains challenging.
- In the case of sub-seismic fractures, alternative methods are required to determine fracture network geometry, connectivity, and thus flow potential. Despite the existence of established geomechanical techniques to predict likely distributions of fracture networks, fully realised fracture network geometry is limited by a lack of lithology-specific, field-scale observations.
- Experimental and numerical investigations into the effect of shear displacement on fluid flow in a single fracture (e.g. Esaki et al., 1999; Frash et al., 2016; Javadi et al., 2014; Li et al., 2008; Rong et al., 2016; Watanabe et al., 2008; Yeo et al., 1998) indicate that conductivity is thought to be greater in fractures which have undergone some degree of shear displacement, as opposed to fractures which have not. The degree to which the fracture wall-rock becomes smoother and the critical effective stress threshold required to transition from dilatant (conductive) to compactive (sealing) behaviour may have a significant impact for predicting potential leakage rates from geological stores (e.g. reactivation).

7. Conclusions

Understanding the fluid flow properties of fractures and fracture networks in mudrocks is crucial for accurate assessment of waste and energy storage security in the subsurface. We have collated and reviewed the large body of literature on the controls on the intrinsic permeabilities of rough fractures and fracture networks, addressing single- and two-phase fluid transport and the mechanical properties of single fractures and fracture networks, and their impact on fluid flow.

Single-phase fracture flow is now a mature research field, where linear flow regimes are well-understood. Nevertheless, fundamental challenges remain within the nonlinear flow domain, where gaps exist in both our understanding and ability to model the relations between fracture surface properties, turbulence, and viscous and inertial forces. Predictions of fluid flow rates at both the single fracture- and fracture network-scale are further complicated in multiphase flow systems by phase interference and viscous coupling; a greater fundamental understanding of these effects, at a range of length scales, for modelling and prediction of fluid leakage rates is needed. Significant advances in recent years in our understanding of the coupling of fluid flow and the mechanical behaviour of faults and fractures have been made, but, predictions of the behaviour are computationally challenging, and a rigorous understanding for multiphase fluid systems is mostly lacking.

8. Open questions and outlook

Improving our understanding of fault and fracture fluid flow is essential for the accurate assessment of containment risk in subsurface waste and energy storage systems. Satisfying this criterion motivates continued academic and industrial research into this broad research field. Based on the amassed literature and our own observations, we suggest the following outstanding research questions:

1. Additional laboratory and especially field-scale measurements of fault-fracture single and multiphase fluid flow rates are required. Experimentally derived fracture permeability measurements are challenging, require complex upscaling schemes to be applied at the field-scale, and thus require robust verification with field-scale fluid injection experiments.

2. A more fundamental understanding of the nature of multiphase fluid flow in fractures and fracture networks, at a range of length scales, is required to develop improved models of the phenomenon and allow accurate estimates of fluid flow rates. This includes an improved understanding of the relationship between fracture surface roughness, capillarity and phase interference, viscous coupling, and the impact of current and counter-current flows on relative permeabilities. The coupling of fluid flow and mechanics in multiphase fluid systems has seldom been addressed.

3. An improved understanding of fracture deformation and its impact on fluid flow is required. The critical effective stress whereby fractures undergoing shear begin to compact rather than continue to dilate is crucial missing information, as are the methods required to upscale this to the field-scale. An improved framework for relating fracture surface roughness, asperity deformation and fluid flow rates is required.

4. Numerical methods to simulate turbulent flows in rough fractures and fracture networks require further developments. An improved understanding of the transition from laminar to turbulent flow and its fundamental controls in rough-walled fractures is needed, including a more robust definition of the critical Reynolds number.

5. The use of typical constants (e.g. fractal dimension, Hurst coefficient, JRC, relative roughness or Z_2) to describe fracture surface roughness is probably inadequate, as fracture surfaces contain non-uniform discontinuities (e.g. steps and jogs) and characteristically different roughnesses at different length scales. Predictions of fluid flow require an improved understanding of the multiplicity of fracture roughness scales, and methods to account for irregular features.

6. Geochemical influences may profoundly impact both the local and large-scale permeability of fracture systems, with mineral precipitation greatly reducing conductivity, whereas mineral dissolution may promote leakage through fractured caprocks. Integration of chemical and mechanical models is required in the future, both for the prediction of fracture network distribution and for accurate prediction of fracture permeability in response to geochemical and geomechanical coupling processes.

7. Significant challenges persist in finding adequate representations of the 3D complexity and multiplicity of scales in fracture systems, especially when considering that naturally occurring fractures form under specific self-organised dynamics. Accurate representations of hydromechanical coupling across a wide range of scales and boundary conditions remain elusive.

8. Characterising the complexities of natural fracture geometries is by no means a trivial undertaking, as subsurface data needed to accurately represent such systems is limited, and numerical methods to predict fracture geometries are illustrative at best. Additional observational data, in 3D, is badly needed. Investigation into analogue storage systems is highly desirable to progress our understanding of how different geological components (reservoir, caprock, and fault/fracture systems) interact with one another and drive the process of fault/fracture leakage in a real setting.

Nomenclature

A_eQ	Coefficient describing energy loss due to viscous forces [−]
a	Local aperture [m]
a_c	Critical aperture size [m]
$a_{c,\,max}$	Apertures larger than a critical value [m]
$a_{c,\,min}$	Apertures smaller than a critical value [m]
a_m	Initial mean of the aperture field [m]
a_{max}	Elliptical cross-section of a fracture with maximum opening [−]
B_eQ	Coefficient describing energy loss due to inertial forces [−]
b_m	Possible maximum aperture closure [m]
C	Proportionality constant [−]
CL	Cubic law [−]
c_n	Normal stiffness at zero stress intercept [−]
d	Core plug diameter [m]
D_E	Euclidean dimension of the embedding medium [−]
D_f	Fractal dimension [−]
D_T	Intrinsic topological dimension [−]
E	Young's modulus [MPa]
e_h	Hydraulic aperture [m]
e_m	Mechanical aperture [m]
F	Geometric parameter related to the sample dimensions [m]
F_0	Forchheimer number [−]
G	Gravity constant [g/cm³]
g	Gravitational acceleration [m²/s]
$G(k)$	Power spectral density functions [−]
H	Hurst coefficient [−]
h	Vertical height above a surface [m]
J	Fitting coefficient [−]
JCS	Joint compressive strength [MPa]
JRC	Joint roughness coefficient [−]
$K_{fracture}$	Fracture conductivity [m²]
k^F	Fracture permeability [m²]
k^{FM}	Permeability of a uniformly fractured matrix with negligible permeability [m²]
$K^{\overline{F}}$	Reduced fracture permeability [m²]
k_f	Partially saturated conditions [−]
k_{bulk}	Bulk permeability [m²]
k_{matrix}	Matrix permeability [m²]
k_n	Specific stiffness of a fracture [−]
k_r	Relative permeability [−]
$k_{rs,\,w}$	Satiated value of the wetting phase relative permeability [−]
$k_{rs,\,nw}$	Satiated value of the non-wetting phase relative permeability [−]
k_s	Fully saturated conditions [−]
$k_{r,\,w}$	Wetting phase relative permeability [−]
$k_{r,\,nw}$	Non-wetting phase relative permeability [−]
L	Linear distance (length) of a fracture [m]
LCL	Local cubic law [−]
L_0	Effective path length [m]
$MLCL$	Modified local cubic law [−]
N_t	Number of sampling points along the length of a fracture [−]
nw	Non-wetting phase [−]
P_c	Capillary pressure [MPa]
P_e	Capillary entry pressure [MPa]
P_p	Pore pressure [MPa]
P_{nw}	Non-wetting phase pressure [MPa]
P_w	Wetting phase pressure [MPa]
p	Fluid pressure [MPa]
Q	Volumetric flow rate (hydraulic transmissivity) [m³.s⁻¹]
Re	Reynolds number [−]
Re_c	Critical Reynolds number [−]
R_1	Aperture-induced radii of curvature of the fluid-fluid interface [°]
R_2	In-plane radii of curvature of the fluid-fluid interface [°]
s	Fracture spacing [m]
$S_{h,\,min}$	Minimum horizontal stress [MPa]
S_{nw}	Non-wetting phase saturation [%]
S_w	Wetting phase saturation [%]
S_{we}	Effective saturation of wetting phase [%]
S_{ws}	Satiated saturation of the wetting phase [%]
S_{nwe}	Effective saturation of non-wetting phase [%]
S_{nws}	Satiated saturation of the non-wetting phase [%]
$S_{nw,\,r}$	Residual non-wetting phase saturation [%]
$S_{w,\,r}$	Residual wetting phase saturation (irreducible saturation) [%]
T	Fluid transmissivity [m².s⁻¹]
u	Amplitude of shear [−]
v	Poisson's ratio [−]
v_{nw}	Non-wetting phase flow velocity [m³/s]
v_w	Wetting phase flow velocity [m³/s]

|				
$\tilde{v}$	Mean velocity [m³/s]		σ	Total applied stress [MPa]
w	Wetting phase [−]		σ_a	Standard deviation of the aperture [m]
w_f	Fracture width [m]		σ_a/a_m	Relative roughness [−]
x_i	Coordinates of the fracture surface profile [−]		σ_c	Uniaxial compressive strength [MPa]
Z_i	Coordinates of the fracture surface profile [−]		σ_n	Normal stress [MPa]
Z_2	Root mean square of the first derivative of a fracture surface profile [−]		σ_n'	Effective normal stress [MPa]
α	Power (falling in the range $2 < \alpha > 3$) [−]		σ'	Effective stress [MPa]
α_c	Ratio of the contact area to the total area of the fracture [−]		σ_1	Maximum principal compressive strength [MPa]
ρ	Fluid density [g/cm³]		ζ	Coordinate [−]
ρ_{nw}	Non-wetting phase density [g/cm³]			
ρ_w	Wetting phase density [g/cm³]			
P	Reduced pressure [MPa]			
$\mathbf{u}$	Velocity vector of the fluid [m³/s]			
μ	Fluid viscosity [Pa·s]			
u_s	Shear stress [MPa]			
$u_{s,\,peak}$	Peak shear stress [MPa]			
$\mu_{v,\,w}$	Wetting phase dynamic viscosity [Pa·s]			
$\mu_{v,\,nw}$	Non-wetting phase dynamic viscosity [Pa·s]			
τ	Tortuosity [−]			
τ_i	In-plane tortuosity [−]			
τ_0	Out-of-plane tortuosity [−]			
β	Forchheimer coefficient [−]			
λ	Empirical pore size distribution index [−]			
λ_a	Wavelength of the dominant aperture [m]			
$\lambda_{asperity}$	Wavelength of asperities [m]			
γ	Interfacial tension [N/m]			
$\acute{y}$	Constant [−]			
$\acute{Z}$	Constant [−]			
Φ	Local hydraulic head [m]			
θ	Fluid-fluid contact angle [°]			
θ_{mob}	Mobilised dilation angle [°]			
Δa	Fracture closure in the normal direction [−]			
$\Delta a_{c,\,max}$	Maximum normal closure [m]			
Δa_s	Aperture dilation [m]			
Δh	Height difference [m]			
Δx	Horizontal difference [m]			
$\Delta \rho$	Density contrast between two phases [g/cm³]			

Appendix A. Rock samples

From recovered core material obtained from a scientific drilling campaign performed to investigate natural (along-fault) leakage from a natural CO_2 reservoir (Kampman et al., 2014b; Kampman et al., 2013), we cored four fractures from a fractured mudrock sequence, which is a regional aquitard (Carmel Formation). Details of each sample are provided in Table A.1.

Table A.1
Rock samples used in this study, obtained from core recovered as a part of the CO2W55 drilling project in Green River, Utah (USA), (Kampman et al., 2014b).

Sample	Depth (m)	Formation	Fracture type
Carmel Sample 1 (Fig. 4a, 13, & 14)	195 m	Carmel	Drilling-induced
Carmel Sample 2 (Fig. A.1)	186.2–186.4 m	Carmel	Natural
Carmel Sample 3 (Fig. A.1)	186.2–186.4 m	Carmel	Natural
Carmel Sample 4 (Fig. A.1)	186.2–186.4 m	Carmel	Natural

Carmel samples 2, 3 and 4 (Fig. A.1) represent high angle open fractures, orientated parallel to the normal fault (Dockrill and Shipton, 2010), showing mm to cm normal offsets. We conclude that these are natural fractures formed in relation to the large-scale fault, and not drilling- or uplift-related on account of orientation and offset. These fracture surfaces attest to inherent topographic complexities occurring across micrometre to centimetre length scales, exhibiting H values ranging between 0.41 and 0.54 (D_f = 2.59–2.46).
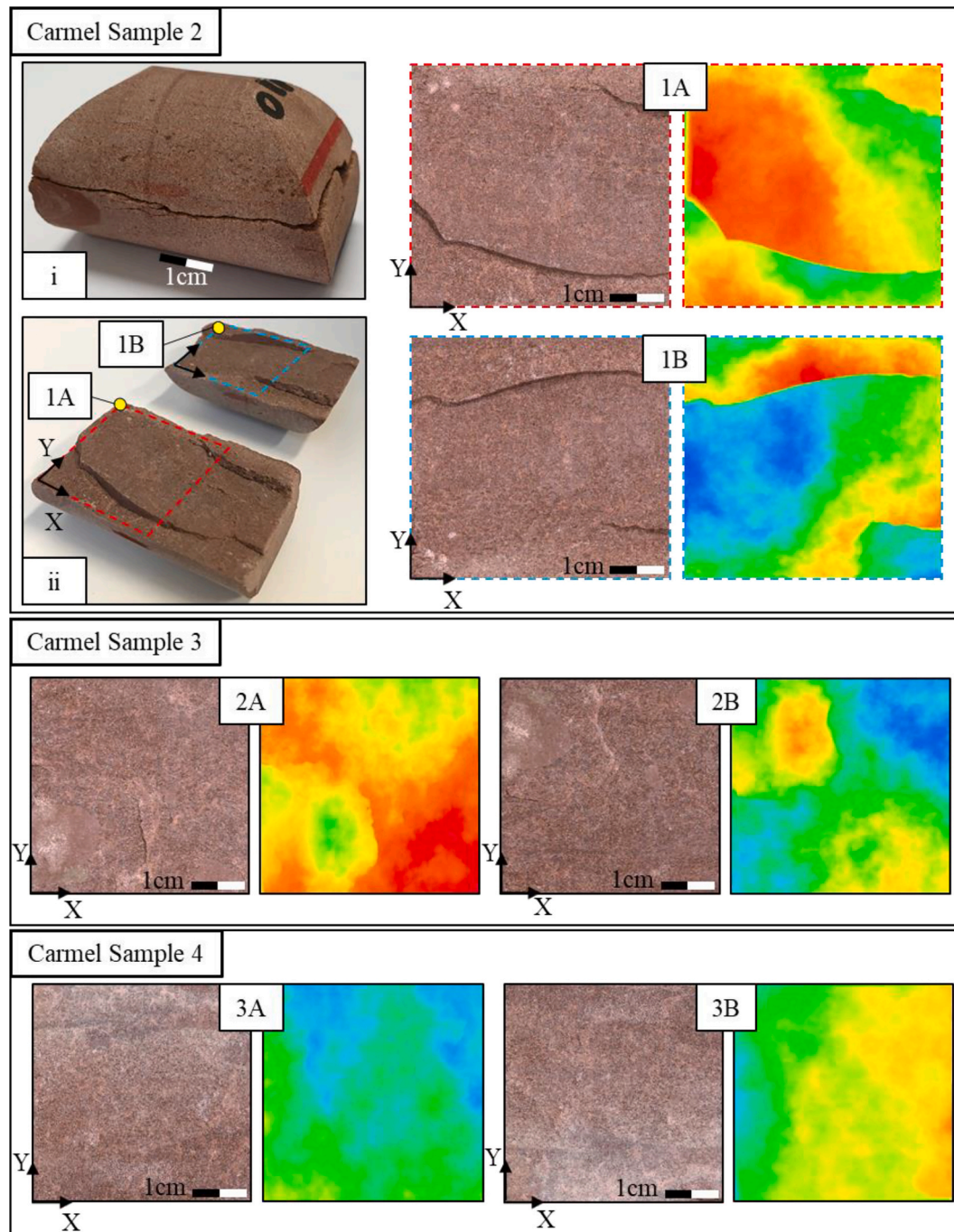
Fig. A.1. Fracture surface scans of 3 naturally fractured samples obtained from a scientific drilling campaign near Green River, Utah, USA (Kampman et al., 2014b). Carmel Sample 2: (i) Full core plug. (ii) Top and bottom fracture surface. (1A) Plan view of the bottom fracture surface highlighted (dashed red box) in ii. Left: 100 x magnification scan of the fracture surface. Right: Resulting 3D topographical colour map showing micrometre-scale fracture surface variations. (1B) Top fracture surface highlighted (dashed blue box) in ii. Carmel Sample 3 & 4: (A) Plan view of the bottom fracture surface. Left: 100 x magnification scan of the fracture surface. Right: Resulting 3D topographical colour map.

Appendix B. Laboratory single-phase permeability measurements

Single-phase permeability measurements were performed on Carmel Sample 1 (Table A.1), a 2.54 cm diameter core plug (Fig. 4a). A single fracture spans the sample, which we conclude is drilling-induced. Sample permeability was measured using the steady-state method with nitrogen as the permeating gas for effective stresses ranging between 0.83 and 18.25 MPa, achieved through varying both the confining and pore pressure. Table B.1 provides a full list of testing conditions and the corresponding permeabilities. All tests were carried out at a temperature of 25°C.

Table B.1
Test conditions for steady state permeability experiments on the Carmel 1 sample.

Confining pressure (MPa)	Mean pore pressure (MPa)	Effective stress (MPa)	Permeability (1×10^{-17} m^2)
5.00	1.94	3.06	27.69
5.00	1.83	3.17	25.81
7.00	1.93	5.07	18.39
7.00	2.67	4.33	19.12
7.00	2.78	4.22	17.57
7.00	2.68	4.32	17.41
14.88	4.01	10.88	5.38
15.00	5.22	9.78	4.93
15.00	6.73	8.27	4.92
15.01	6.63	8.39	4.95
20.93	6.20	14.73	2.77
20.85	7.76	13.09	2.74
20.89	5.38	15.51	3.01
20.96	2.71	18.25	3.79
9.06	2.79	6.27	6.25
9.06	0.80	8.26	8.41
2.21	0.94	1.27	37.93
2.18	1.30	0.88	44.41
2.17	1.34	0.83	46.18

Using the method outlined in Section 6.1.3, fracture permeability was calculated from the core permeability measurements. Fig. B.1 compares a fitted permeability to the bulk permeability measurements from Table B.1 for Carmel Sample 1 (Table A.1) tested as part of this study. This method was also used to calculate fracture permeabilities from other datasets presented in Fig. 13, with a summary of the fitting parameters (a_c, b_m, $\acute{y}$ and Z) used to calculate fracture permeabilities (Fig. 14) presented in Table B.2.
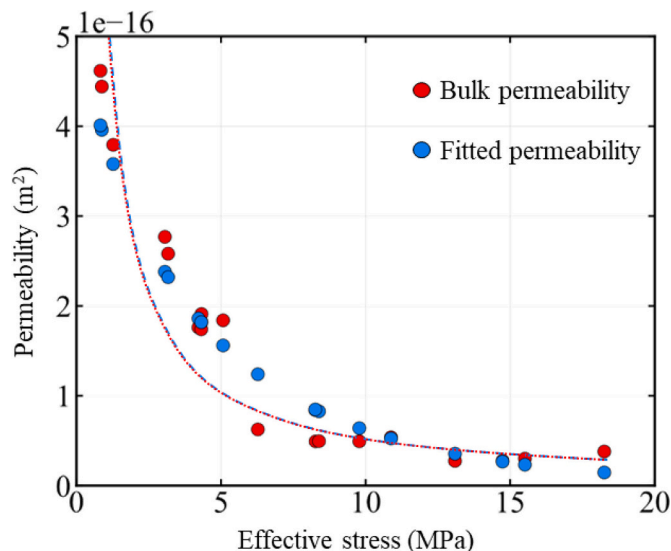
Fig. B.1. Comparison of fitted permeability to bulk permeability of the Carmel 1 sample tested as part of this study.

Table B.2
Fitting parameters used to calculate fracture permeabilities in Fig. 14.

Sample	a_c	b_m	$\acute{y}$	Z
Carmel Sample 1 (this study)	1.00E-07	5.10E−06	1.00E−01	0.84
Bakken (Cho et al., 2013)	0	1.36E−05	3.50E−02	0.675
Callovo-Oxfordian Argillite (Davy et al., 2007)	0	4.00E−05	1.99E−01	0.675
Carmel (Bjørnara et al., 2018)	0	9.90E−06	5.30E−02	0.78
Rurikfjellet Shale (van Noort and Yarushina, 2016)	0	4.50E−07	1.00E−01	0.96
Longmaxi Shale (Yang et al., 2019a)	0	4.20E−06	7.00E−02	0.7
Whitby Mudstone (Houben et al., 2020)	0	1.50E−06	1.80E−01	0.542

Appendix C. Surface roughness characterisation

To investigate fracture surface topography of Carmel samples 1, 2, 3 and 4 (Table C.1 & Fig. A.1) on the micrometre-scale, a Keyence VHX-6000 digital optical microscope (Keyence, 2017) was utilised to produce a 3D realisation of each fracture surface using photogrammetry. Each fracture surface, in turn, was positioned on an XYZ motorised microscope stage, supported by modelling clay to stabilise the cylindrical samples. Once sample alignment and stability was achieved, the horizontal area of interest was identified through digitally selecting the outer four edges (Fig. A.1). Selection area is a function of the maximum pixel limit and the scanning magnification. A 100 x magnification was chosen to allow for the largest field of view (x and y dimensions) while maintaining high-resolution. The vertical (z dimension) was then defined through digitally identifying the minimum and maximum height ranges, enabling the vertical scanning range to be constrained on a sample-specific basis.

All scans were conducted using high definition settings, yielding uncompressed (TIF) images comprising bit depths of 24 and horizontal and vertical resolutions of 96 dpi (dots per inch). The maximum achievable image size was limited to 20,000 x 20,000 pixels; meaning for samples scanned at 100 x magnification, a resolution of approximately 1–2.5 μm per pixel was achieved. During scanning, an embedded image-stitching algorithm used fine changes in surface texture to calculate the respective 3D height data by compiling multiple overlapping images at different exposures and focal planes. Several automated scans were conducted in a grid-like fashion, which were stitched together to produce a true colour (RGB) image and a 3D height field that was then extracted for roughness analysis (Adler et al., 2012; Hale et al., 2019). To omit sampling bias, a Python-based workflow was utilised in conjunction with open-source image processing toolboxes (van der Walt et al., 2014).

Table C.1

Roughness statistics obtained for Carmel samples 1, 2, 3 and 4 (Table A.1). Descriptions of each parameter and methods of calculation are detailed in Section 3.2.1. It should be noted that these measurements were performed at high-resolution, meaning that surface roughness measurements documented in other studies, at lower resolutions, might differ.

Sample	Hurst coefficient (H) (x, y)	Joint Roughness Coefficient (JRC) (x, y)
Carmel Sample 1 top	(0.4, 0.42)	(9.87, 12.66)
Carmel Sample 1 bottom	(0.41, 0.42)	(10.33, 12)
Carmel Sample 2 (Side 1A)	(0.42, 0.46)	(22.65, 19.17)
Carmel Sample 2 (Side 1B)	(0.48, 0.41)	(20.74, 19.04)
Carmel Sample 3 (Side 2A)	(0.41, 0.49)	(19.29, 21.34)
Carmel Sample 3 (Side 2B)	(0.46, 0.51)	(20.27, 20.25)
Carmel Sample 4 (Side 3A)	(0.43, 0.47)	(21.05, 20.6)
Carmel Sample 4 (Side 3B)	(0.54, 0.5)	(19.6, 19.7)

References

Ackermann, R.V., Schlische, R.W., 1997. Anticlustering of small normal faults around larger faults. Geology 25 (12), 1127–1130.

Adler, P.M., Thovert, J.F., 1999. Fractures and Fracture Networks. Springer Netherlands.

Adler, P.M., Thovert, J.F., Mourzenko, V.V., 2012. Fractured Porous Media. OUP Oxford.

Ai-Yaarubi, A.H., Pain, C.C., Grattoni, C.A., Zimmerman, R.W., 2005. Navier-Stokes simulations of fluid flow through a rock fracture. In: Faybishenko, B., Witherspoon, P.A., Gale, J. (Eds.), Dynamics of Fluids and Transport in Fractured Rock. Geophysical Monograph Seriespp. 55–64.

Al-Fahmi, M.M., Ozkaya, S.I., Cartwright, J.A., 2018. New insights on fracture roughness and wall mismatch in carbonate reservoir rocks. Geosphere 14 (4), 1851–1859.

Alzayer, Y., Eichhubl, P., Laubach, S.E., 2015. Non-linear growth kinematics of opening-mode fractures. J. Struct. Geol. 74, 31–44.

Amann-Hildenbrand, A., Ghanizadeh, A., Krooss, B.M., 2012. Transport properties of unconventional gas systems. Mar. Pet. Geol. 31 (1), 90–99.

Amann-Hildenbrand, A., Bertier, P., Busch, A., Krooss, B.M., 2013. Experimental investigation of the sealing capacity of generic clay-rich caprocks. Int. J. Greenh. Gas Control 19, 620–641.

Anders, M.H., Laubach, S.E., Scholz, C.H., 2014. Microfractures: a review. J. Struct. Geol. 69, 377–394.

Anderson, T.L., 2005. Fracture Mechanics: Fundamentals and Applications, Third edition. Taylor & Francis.

Ankit, K., Urai, J.L., Nestler, B., 2015. Microstructural evolution in bitaxial crack-seal veins: A phase-field study. J. Geophys. Res. Solid Earth 120 (5), 3096–3118.

Asadollahi, P., Invernizzi, M.C.A., Addotto, S., Tonon, F., 2010. Experimental validation of modified Barton's model for rock fractures. Rock Mech. Rock. Eng. 43 (5), 597–613.

Atkinson, B.K., 1984. Subcritical crack-growth in geological-materials. J. Geophys. Res. 89 (NB6), 4077–4114.

Atkinson, B.K., 2015. Fracture Mechanics of Rock. Elsevier Science.

Auradou, H., 2009. Influence of wall roughness on the geometrical, mechanical and transport properties of single fractures. J. Phys. D Appl. Phys. 42 (21).

Aydin, A., Borja, R.I., Eichhubl, P., 2006. Geological and mathematical framework for failure modes in granular rock. J. Struct. Geol. 28 (1), 83–98.

Babadagli, T., Develi, K., 2003. Fractal characteristics of rocks fractured under tension. Theor. Appl. Fract. Mech. 39 (1), 73–88.

Babadagli, T., Ershaghi, I., 1992. Imbibition assisted two-phase flow in natural fractures. In: SPE Western Regional Meeting. Society of Petroleum Engineers.

Babadagli, T., Ren, X.J., Develi, K., 2015. Effects of fractal surface roughness and lithology on single and multiphase flow in a single fracture: an experimental investigation. Int. J. Multiphase Flow 68, 40–58.

Baghbanan, A., Jing, L., 2008. Stress effects on permeability in a fractured rock mass with correlated fracture length and aperture. Int. J. Rock Mech. Min. Sci. 45 (8), 1320–1334.

Bai, T.X., Pollard, D.D., 2000. Closely spaced fractures in layered rocks: initiation mechanism and propagation kinematics. J. Struct. Geol. 22 (10), 1409–1425.

Bakker, E., Hangx, S.J.T., Niemeijer, A.R., Spiers, C.J., 2016. Frictional behaviour and transport properties of simulated fault gouges derived from a natural CO2 reservoir. Int. J. Greenh. Gas Control 54, 70–83.

Bandis, S.C., Lumsden, A.C., Barton, N.R., 1983. Fundamentals of rock joint deformation. Int. J. Rock Mech. Min. Sci. 20 (6), 249–268.

Barton, N., 2013. Shear strength criteria for rock, rock joints, rockfill and rock masses: problems and some solutions. J. Rock Mech. Geotech. Eng. 5, 249–261.

Barton, N., Choubey, V., 1977. The shear strength of rock joints in theory and practice. Rock Mech. 10, 1–54.

Barton, N., de Quadros, E.F., 1997. Joint aperture and roughness in the prediction of flow and groutability of rock masses. Int. J. Rock Mech. Min. Sci. 34 (3-4), 252.

Barton, N., Bandis, S., Bakhtar, K., 1985. Strength, deformation and conductivity coupling of rock joints. Int. J. Rock Mech. Min. Sci. 22 (3), 121–140.

Barton, C.A., Zoback, M.D., Moos, D., 1995. Fluid-flow along potentially active faults in crystalline rock. Geology 23 (8), 683–686.

Basha, H.A., El-Asmar, W., 2003. The fracture flow equation and its perturbation solution. Water Resour. Res. 39 (12).

Batchelor, C.K., Batchelor, G., 2000. An introduction to Fluid Dynamics. Cambridge university press.

Bauer, S., Dahmke, A., Kolditz, O., 2017. Subsurface energy storage: geological storage of renewable energy-capacities, induced effects and implications. Environ. Earth Sci. 76 (20).

Bear, J., 1972. Dynamics of Fluids in Porous Media. Am. Elsevier, New York.

Berkowitz, B., 2002. Characterizing flow and transport in fractured geological media: a review. Adv. Water Resour. 25 (8–12), 861–884.

Berre, I., Doster, F., Keilegavlen, E., 2018. Flow in fractured porous media: a review of conceptual models and discretization approaches. Transp. Porous Media 1–22.

Bertels, S.P., DiCarlo, D.A., Blunt, M.J., 2001. Measurement of aperture distribution, capillary pressure, relative permeability, and in situ saturation in a rock fracture using computed tomography scanning. Water Resour. Res. 37 (3), 649–662.

Bildstein, O., Kervevan, C., Lagneau, V., Delaplace, P., Credoz, A., Audigane, P., Perfetti, E., Jacquemet, N., Jullien, M., 2010. Integrative modeling of caprock integrity in the context of CO2 storage: evolution of transport and geochemical properties and impact on performance and safety assessment. Oil Gas Sci. Technol. Rev. D IFP Energ.

Nouvelles 65 (3), 485–502.

Bilham, R., King, G., 1989. The morphology of strike-slip faults: examples from the San Andreas Fault, California. J. Geophys. Res. Solid Earth Planets 94 (B8), 10204–10216.

Billi, A., Salvini, F., Storti, F., 2003. The damage zone-fault core transition in carbonate rocks: implications for fault growth, structure and permeability. J. Struct. Geol. 25 (11), 1779–1794.

Bisdom, K., Bertotti, G., Nick, H.M., 2016. The impact of different aperture distribution models and critical stress criteria on equivalent permeability in fractured rocks. J. Geophys. Res. Solid Earth Planets 121 (5), 4045–4063.

Bisdom, K., Nick, H.M., Bertotti, G., 2017. An integrated workflow for stress and flow modelling using outcrop-derived discrete fracture networks. Comput. Geosci. 103, 21–35.

Bjørnara, T.I., Skurtveit, E., Sauvin, G., 2018. Stress-dependent fracture permeability in core samples: an experimental and numerical study. In: 2nd International Discrete Fracture Network Engineering Conference. American Rock Mechanics Association, Seattle, Washington, USA, pp. 15.

Boersma, Q.D., Douma, L.A.N.R., Bertotti, G., Barnhoorn, A., 2020. Mechanical controls on horizontal stresses and fracture behaviour in layered rocks: a numerical sensitivity analysis. J. Struct. Geol. 130, 103907.

Bond, C.E., Wightman, R., Ringrose, P.S., 2013. The influence of fracture anisotropy on CO2 flow. Geophys. Res. Lett. 40 (7).

Bonnet, E., Bour, O., Odling, N.E., Davy, P., Main, I., Cowie, P., Berkowitz, B., 2001. Scaling of fracture systems in geological media. Rev. Geophys. 39 (3), 347–383.

Bons, P.D., Elburg, M.A., Gomez-Rivas, E., 2012. A review of the formation of tectonic veins and their microstructures. J. Struct. Geol. 43, 33–62.

Botros, F.E., Hassan, A.E., Reeves, D.M., Pohll, G., 2008. On mapping fracture networks onto continuum. Water Resour. Res. 44 (8).

Bourne, S.J., Willemse, E.J.M., 2001. Elastic stress control on the pattern of tensile fracturing around a small fault network at Nash Point, UK. J. Struct. Geol. 23 (11), 1753–1770.

Bourne, S.J., Brauckmann, F., Rijkels, L., Stephenson, B.J., Weber, A., Willemse, E.J.M., 2000. Predictive modelling of naturally fractured reservoirs using geomechanics and flow simulation. In: Abu Dhabi International Petroleum Exhibition and Conference. Society of Petroleum Engineers, Abu Dhabi, United Arab Emirates, pp. 10.

Boutt, D.F., Grasselli, G., Fredrich, J.T., Cook, B.K., Williams, J.R., 2006. Trapping zones: the effect of fracture roughness on the directional anisotropy of fluid flow and colloid transport in a single fracture. Geophys. Res. Lett. 33 (21).

Briggs, S., Karney, B.W., Sleep, B.E., 2014. Numerical modelling of flow and transport in rough fractures. J. Rock Mech. Geotech. Eng. 6 (6), 535–545.

Briggs, S., Karney, B.W., Sleep, B.E., 2017. Numerical modeling of the effects of roughness on flow and eddy formation in fractures. J. Rock Mech. Geotech. Eng. 9 (1), 105–115.

Brown, S.R., 1987. Fluid-flow through rock joints - The effect of surface-roughness. J. Geophys. Res. Solid Earth Planets 92 (B2), 1337–1347.

Brown, S.R., 1995a. Measuring the dimension of self-affine fractals: example of rough surfaces. In: Fractals in the Earth Sciences. Springer, pp. 77–87.

Brown, S.R., 1995b. Simple mathematical-model of a rough fracture. J. Geophys. Res. Solid Earth Planets 100 (B4), 5941–5952.

Brown, S.R., Scholz, C.H., 1985. Broad bandwidth study of the topography of natural rock surfaces. J. Geophys. Res. Solid Earth Planets 90 (B14), 2575–2582.

Brown, S.R., Scholz, C.H., 1986. Closure of rock joints. J. Geophys. Res. Solid Earth Planets 91 (B5), 4939–4948.

Brown, S.R., Stockman, H.W., Reeves, S.J., 1995. Applicability of the Reynolds equation for modeling fluid flow between rough surfaces. Geophys. Res. Lett. 22 (18), 2537–2540.

Brown, S., Caprihan, A., Hardy, R., 1998. Experimental observation of fluid flow channels in a single fracture. J. Geophys. Res. Solid Earth Planets 103 (B3), 5125–5132.

Brush, D.J., Thomson, N.R., 2003. Fluid flow in synthetic rough-walled fractures: Navier-Stokes, Stokes, and local cubic law simulations. Water Resour. Res. 39 (4).

Burdine, N., 1953. Relative permeability calculations from pore size distribution data. J. Pet. Technol. 5 (3), 71–78.

Busch, A., Amann-Hildenbrand, A., 2013. Predicting capillarity of mudrocks. Mar. Pet. Geol. 45, 208–223.

Busch, A., Kampman, N., 2018. Migration and leakage of CO2 from deep geological storage sites. In: Vialle, S., Ajo-Franklin, J., Carey, J.W. (Eds.), Geological Carbon Storage, pp. 285–302.

Busch, A., Bertier, P., Gensterblum, Y., Rother, G., Spiers, C.J., Zhang, M., Wentinck, H.M., 2016. On sorption and swelling of CO2 in clays. Geomech. Geophys. Geo-Energy Geo-Resour. 2 (2), 111–130.

Busch, A., Hangx, S.J.T., Marshall, J.D., Wentinck, H.M., 2020. Swelling clay minerals and containment risk assessment for the storage seal of the Peterhead CCS project. Int. J. Greenh. Gas Control 94.

Caine, J.S., Evans, J.P., Forster, C.B., 1996. Fault zone architecture and permeability structure. Geology 24 (11), 1025–1028.

Candela, T., Renard, F., Klinger, Y., Mair, K., Schmittbuhl, J., Brodsky, E.E., 2012. Roughness of fault surfaces over nine decades of length scales. J. Geophys. Res. Solid Earth Planets 117.

Cao, J., Kitanidis, P., 1998. Adaptive finite element simulation of Stokes flow in porous media. Adv. Water Resour. 22 (1), 17–31.

Cappa, F., Rutqvist, J., 2011. Modeling of coupled deformation and permeability evolution during fault reactivation induced by deep underground injection of CO2. Int. J. Greenh. Gas Control 5 (2), 336–346.

Cardenas, M.B., Slottke, D.T., Ketcham, R.A., Sharp Jr., J.M., 2007. Navier-Stokes flow and transport simulations using real fractures shows heavy tailing due to eddies. Geophys. Res. Lett. 34 (14).

Cardenas, M.B., Slottke, D.T., Ketcham, R.A., Sharp Jr., J.M., 2009. Effects of inertia and directionality on flow and transport in a rough asymmetric fracture. J. Geophys. Res. 114.

Carey, J.W., Lei, Z., Rougier, E., Mori, H., Viswanathan, H., 2015. Fracture-permeability behavior of shale. J. Unconv. Oil Gas Resour. 11, 27–43.

Carr, J.R., Warriner, J.B., 1989. Relationship between the fractal dimension and joint roughness coefficient. Bull. Assoc. Eng. Geol. 26 (2), 253–263.

Chaudhuri, A., Rajaram, H., Viswanathan, H., 2012. Fracture alteration by precipitation resulting from thermal gradients: upscaled mean aperture-effective transmissivity relationship. Water Resour. Res. 48 (1).

Chen, C.Y., Horne, R.N., 2006. Two-phase flow in rough-walled fractures: experiments and a flow structure model. Water Resour. Res. 42 (3).

Chen, C.Y., Horne, R.N., Fourar, M., 2004. Experimental study of liquid-gas flow structure effects on relative permeabilities in a fracture. Water Resour. Res. 40 (8).

Chen, Y.F., Zhou, J.Q., Hu, S.H., Hu, R., Zhou, C.B., 2015. Evaluation of Forchheimer equation coefficients for non-Darcy flow in deformable rough-walled fractures. J. Hydrol. 529, 993–1006.

Cheng, Y., 2018. On improving the local cubic law for fracture flow modeling by keeping impacts of fluid inertia and irregular boundaries. J. Porous Media 21 (1), 51–64.

Cho, Y., Apaydin, O.G., Ozkan, E., 2013. Pressure-dependent natural-fracture permeability in shale and its effect on shale-gas well production. SPE Reserv. Eval. Eng. 16 (2), 216–228.

Cook, N.G.W., 1992. Natural joints in rock - Mechanical, hydraulic and seismic behavior and properties under normal stress. Int. J. Rock Mech. Min. Sci. Geomech. Abstr. 29 (3), 198–223.

Corey, A.T., 1954. The interrelation between gas and oil relative permeabilities. Prod. Mon. 19 (1), 38–41.

Cosgrove, J.W., 2015. The association of folds and fractures and the link between folding, fracturing and fluid flow during the evolution of a fold-thrust belt: a brief review. In: Richards, F.L., Richardson, N.J., Rippington, S.J., Wilson, R.W., Bond, C.E. (Eds.), Industrial Structural Geology: Principles, Techniques and Integration. Geological Society Special Publication, pp. 41–68.

Council, N.R., Studies, D.E.L., Commission on Geosciences, E.R., Flow, C.F.C.F., 1996. Rock Fractures and Fluid Flow: Contemporary Understanding and Applications. National Academies Press.

Cowie, P.A., Knipe, R.J., Main, I.G., 1996. Special issue: scaling laws for fault and fracture populations – analyses and applications – introduction. J. Struct. Geol. 18 (2-3), R5–R11.

Crandall, D., Bromhal, G., Karpyn, Z.T., 2010. Numerical simulations examining the relationship between wall-roughness and fluid flow in rock fractures. Int. J. Rock Mech. Min. Sci. 47 (5), 784–796.

Crandall, D., Moore, J., Gill, M., Stadelman, M., 2017. CT scanning and flow measurements of shale fractures after multiple shearing events. Int. J. Rock Mech. Min. Sci. 100, 177–187.

Crouch, S.L., Starfield, A.M., 1983. Boundary Element Methods in Solid Mechanics. George Allen and Unwin, London.

Cruikshank, K.M., Zhao, G.H., Johnson, A.M., 1991. Analysis of minor fractures associated with joints and faulted joints. J. Struct. Geol. 13 (8), 865–886.

Cuss, R.J., Milodowski, A., Harrington, J.F., 2011. Fracture transmissivity as a function of normal and shear stress: first results in Opalinus Clay. Phys. Chem. Earth 36 (17-18), 1960–1971.

da Silva, J.A., Kang, P.K., Yang, Z.B., Cueto-Felgueroso, L., Juanes, R., 2019. Impact of confining stress on capillary pressure behavior during drainage through rough fractures. Geophys. Res. Lett. 46 (13), 7424–7436.

Davatzes, N.C., Eichhubl, P., Aydin, A., 2005. Structural evolution of fault zones in sandstone by multiple deformation mechanisms: Moab fault, southeast Utah. Geol. Soc. Am. Bull. 117 (1-2), 135–148.

David, C., 1993. Geometry of flow paths for fluid transport in rocks. J. Geophys. Res. Solid Earth Planets 98 (B7), 12267–12278.

Davies, R., Foulger, G., Bindley, A., Styles, P., 2013. Induced seismicity and hydraulic fracturing for the recovery of hydrocarbons. Mar. Pet. Geol. 45, 171–185.

Davy, C.A., Skoczylas, F., Barnichon, J.D., Lebon, P., 2007. Permeability of macro-cracked argillite under confinement: gas and water testing. Phys. Chem. Earth 32 (8-14), 667–680.

Davy, P., Le Goc, R., Darcel, C., Bour, O., de Dreuzy, J.R., Munier, R., 2010. A likely universal model of fracture scaling and its consequence for crustal hydromechanics. J. Geophys. Res. Solid Earth Planets 115.

de Dreuzy, J.R., Davy, P., Bour, O., 2000. Percolation parameter and percolation-threshold estimates for three-dimensional random ellipses with widely scattered distributions of eccentricity and size. Phys. Rev. E 62 (5), 5948–5952.

de Dreuzy, J.R., Meheust, Y., Pichot, G., 2012. Influence of fracture scale heterogeneity on the flow properties of three-dimensional discrete fracture networks (DFN). J. Geophys. Res. Solid Earth Planets 117.

De Joussineau, G., Aydin, A., 2007. The evolution of the damage zone with fault growth in sandstone and its multiscale characteristics. J. Geophys. Res. Solid Earth Planets 112 (B12).

Dee, S.J., Yielding, G., Freeman, B., Healy, D., Kusznir, N.J., Grant, N., Ellis, P., 2007. Elastic dislocation modelling for prediction of small-scale fault and fracture network characteristics. In: Lonergan, L., Jolly, R.J.H., Rawnsley, K., Sanderson, D.J. (Eds.), Fractured Reservoirs. Geological Society Special Publication, pp. 139–+.

Deng, H., Spycher, N., 2019. Modeling reactive transport processes in fractures. Rev.

Mineral. Geochem. 85 (1), 49–74.

Deng, H., Ellis, B.R., Peters, C.A., Fitts, J.P., Crandall, D., Bromhal, G.S., 2013. Modifications of carbonate fracture hydrodynamic properties by CO2-acidified brine flow. Energy Fuel 27 (8), 4221–4231.

Deng, H., Molins, S., Trebotich, D., Steefel, C., DePaolo, D., 2018. Pore-scale numerical investigation of the impacts of surface roughness: upscaling of reaction rates in rough fractures. Geochim. Cosmochim. Acta 239, 374–389.

Dershowitz, W.S., Einstein, H.H., 1988. Characterizing rock joint geometry with joint system models. Rock Mech. Rock. Eng. 21 (1), 21–51.

Dershowitz, W.S., Fidelibus, C., 1999. Derivation of equivalent pipe network analogues for three-dimensional discrete fracture networks by the boundary element method. Water Resour. Res. 35 (9), 2685–2691.

Detwiler, R.L., 2010. Permeability alteration due to mineral dissolution in partially saturated fractures. J. Geophys. Res. Solid Earth Planets 115.

Detwiler, R., Morris, J.P., 2014. Transmissivity anisotropy in rough-walled fractures: the combined influence of shear offset and normal deformation. In: 48th US Rock Mechanics/Geomechanics (ARMA). Vol. 7539. pp. 1–6.

Dijk, P., Berkowitz, B., 1998. Precipitation and dissolution of reactive solutes in fractures. Water Resour. Res. 34 (3), 457–470.

Diomampo, G., 2001. Relative permeability through fractures. Stanford University, Stanford, CA.

Dockrill, B., Shipton, Z.K., 2010. Structural controls on leakage from a natural CO2 geologic storage site: Central Utah, USA. J. Struct. Geol. 32 (11), 1768–1782.

Dou, Z., Zhou, Z.F., Sleep, B.E., 2013. Influence of wettability on interfacial area during immiscible liquid invasion into a 3D self-affine rough fracture: Lattice Boltzmann simulations. Adv. Water Resour. 61, 1–11.

Douma, L.A.N.R., Regelink, J.A., Bertotti, G., Boersma, Q.D., Barnhoorn, A., 2019. The mechanical contrast between layers controls fracture containment in layered rocks. J. Struct. Geol. 127, 103856.

Drikakis, D., Frank, M., Tabor, G., 2019. Multiscale Computational Fluid Dynamics. Energies 12 (17).

Durham, W.B., Bonner, B.P., 1994. Self-propping and fluid-flow in slightly offset joints at high effective pressures. J. Geophys. Res. Solid Earth Planets 99 (B5), 9391–9399.

Edwards, R.W.J., Doster, F., Celia, M.A., Bandilla, K.W., 2017. Numerical modeling of gas and water flow in shale gas formations with a focus on the fate of hydraulic fracturing fluid. Environ. Sci. Technol. 51 (23), 13779–13787.

Einstein, H.H., Baecher, G.B., 1983. Probabilistic and statistical – methods in engineering geology – specific methods and examples. 1. Exploration. Rock Mech. Rock. Eng. 16 (1), 39–72.

Eker, E., Akin, S., 2006. Lattice Boltzmann simulation of fluid flow in synthetic fractures. Transp. Porous Media 65 (3), 363–384.

Ellis, B., Peters, C., Fitts, J., Bromhal, G., McIntyre, D., Warzinski, R., Rosenbaum, E., 2011. Deterioration of a fractured carbonate caprock exposed to CO2-acidified brine flow. Greenh. Gases Sci. Technol. 1 (3), 248–260.

Ellis, M.A., Laubach, S.E., Eichhubl, P., Olson, J.E., Hargrove, P., 2012. Fracture development and diagenesis of Torridon Group Applecross Formation, near An Teallach, NW Scotland: millennia of brittle deformation resilience? J. Geol. Soc. 169 (3), 297–310.

Elsworth, D., Doe, T.W., 1986. Application of nonlinear flow laws in determining rock fissure geometry from single borehole pumping tests. Int. J. Rock Mech. Min. Sci. 23 (3), 245–254.

Elsworth, D., Goodman, R.E., 1986. Characterization of rock fissure hydraulic conductivity using idealized wall roughness profiles. Int. J. Rock Mech. Min. Sci. 23 (3), 233–243.

Engelder, T., 1985. Loading paths to joint propagation during a tectonic cycle – an example from the Appalachian Plateau, USA. J. Struct. Geol. 7 (3-4), 459–476.

English, J.M., Laubach, S.E., 2017. Opening-mode fracture systems: insights from recent fluid inclusion microthermometry studies of crack-seal fracture cements. Geol. Soc. Lond., Spec. Publ. 458 (1), 257–272.

Esaki, T., Hojo, H., Kimura, T., Kameda, N., Deut Gesell, E., Grundbau, 1991. Shear-flow coupling test on rock joints. In: Proceedings - Seventh International Congress on Rock Mechanics, Vol 1: Rock Mechanics and Environmental Protection, pp. 389–392.

Esaki, T., Du, S., Mitani, Y., Ikusada, K., Jing, L., 1999. Development of a shear-flow test apparatus and determination of coupled properties for a single rock joint. Int. J. Rock Mech. Min. Sci. 36 (5), 641–650.

Espinoza, D.N., Santamarina, J.C., 2017. CO2 breakthrough-Caprock sealing efficiency and integrity for carbon geological storage. Int. J. Greenh. Gas Control 66, 218–229.

Evans, J.P., Forster, C.B., Goddard, J.V., 1997. Permeability of fault-related rocks, and implications for hydraulic structure of fault zones. J. Struct. Geol. 19 (11), 1393–1404.

Evans, M.A., Bebout, G.E., Brown, C.H., 2012. Changing fluid conditions during folding: An example from the central Appalachians. Tectonophysics 576-577, 99–115.

Family, F., Vicsek, T., 1991. Dynamics of Fractal Surfaces. World Scientific.

Fang, Y., Elsworth, D., Wang, C.Y., Ishibashi, T., Fitts, J.P., 2017. Frictional stability-permeability relationships for fractures in shales. J. Geophys. Res. Solid Earth Planets 122 (3), 1760–1776.

Fang, Y., Elsworth, D., Ishibashi, T., Zhang, F.S., 2018. Permeability evolution and frictional stability of fabricated fractures with specified roughness. J. Geophys. Res. Solid Earth Planets 123 (11), 9355–9375.

Faoro, I., Niemeijer, A., Marone, C., Elsworth, D., 2009. Influence of shear and deviatoric stress on the evolution of permeability in fractured rock. J. Geophys. Res. Solid Earth Planets 114 (B1).

Faulkner, D., Jackson, C., Lunn, R., Schlische, R., Shipton, Z., Wibberley, C., Withjack, M., 2010. A review of recent developments concerning the structure, mechanics and fluid flow properties of fault zones. J. Struct. Geol. 32 (11), 1557–1575.

Ferer, M., Crandall, D., Ahmadi, G., Smith, D.H., 2011. Two-phase flow in a rough fracture: experiment and modeling. Phys. Rev. E 84 (1), 016316.

Ferrill, D.A., Morris, A.P., 2003. Dilational normal faults. J. Struct. Geol. 25 (2), 183–196.

Figueiredo, B., Tsang, C.F., Rutqvist, J., Niemi, A., 2015. A study of changes in deep fractured rock permeability due to coupled hydro-mechanical effects. Int. J. Rock Mech. Min. Sci. 79, 70–85.

Fink, R., Krooss, B.M., Gensterblum, Y., Amann-Hildenbrand, A., 2017. Apparent permeability of gas shales – superposition of fluid-dynamic and poro-elastic effects. Fuel 199, 532–550.

Fitts, J.P., Peters, C.A., 2013. Caprock fracture dissolution and CO2 leakage. In: DePaolo, D.J., Cole, D.R., Navrotsky, A., Bourg, I.C. (Eds.), Geochemistry of Geologic Co2 Sequestration. Reviews in Mineralogy & Geochemistrypp. 459–479.

Flemisch, B., Berre, I., Boon, W., Fumagalli, A., Schwenck, N., Scotti, A., Stefansson, I., Tatomir, A., 2018. Benchmarks for single-phase flow in fractured porous media. Adv. Water Resour. 111, 239–258.

Forbes Inskip, N.D., Meredith, P.G., Chandler, M.R., Gudmundsson, A., 2018. Fracture properties of nash point shale as a function of orientation to bedding. J. Geophys. Res. Solid Earth Planets 123 (10), 8428–8444.

Forbes Inskip, N.D., Browning, J., Meredith, P.G., Gudmundsson, A., 2020. Conditions for fracture arrest in layered rock sequences. Results Geophys. Sci. 1-4, 100001.

Forchheimer, P., 1901. Wasserbewegung durch Boden. Z. Ver. Dtsch. Ing. 45, 1782–1788.

Foster, M.D., 1954. The relation between composition and swelling in clays. Clay Clay Miner. 3, 205–220.

Fourar, M., Bories, S., 1995. Experimental study of air-water two-phase flow through a fracture (narrow channel). Int. J. Multiphase Flow 21 (4), 621–637.

Fourar, M., Lenormand, R., 1998. A viscous coupling model for relative permeabilities in fractures. In: SPE Annual Technical Conference and Exhibition. Society of Petroleum Engineers.

Frash, L.P., Carey, J.W., Lei, Z., Rougier, E., Ickes, T., Viswanathan, H.S., 2016. High-stress triaxial direct-shear fracturing of Utica shale and in situ X-ray micro-tomography with permeability measurement. J. Geophys. Res. Solid Earth Planets 121 (7), 5493–5508.

Frash, L.P., Carey, J.W., Ickes, T., Viswanathan, H.S., 2017. Caprock integrity susceptibility to permeable fracture creation. Int. J. Greenh. Gas Control 64, 60–72.

Gale, J., 1990. Hydraulic behaviour of rock joints. Rock Joints 351–362.

Gale, J.F.W., Reed, R.M., Holder, J., 2007. Natural fractures in the Barnett Shale and their importance for hydraulic fracture treatments. AAPG Bull. 91 (4), 603–622.

Gale, J.F.W., Laubach, S.E., Olson, J.E., Eichhubl, P., Fall, A., 2014. Natural fractures in shale: a review and new observations. AAPG Bull. 98 (11), 2165–2216.

Gan, Q., Elsworth, D., 2016. A continuum model for coupled stress and fluid flow in discrete fracture networks. Geomech. Geophys. Geo-Energy Geo-Resour. 2 (1), 43–61.

Gangi, A.F., 1978. Variation of whole and fractured porous rock permeability with confining pressure. Int. J. Rock Mech. Min. Sci. 15 (5), 249–257.

Garrels, R.M., Mackenzie, F.T., 1969. Sedimentary rock types – relative proportions as a function of geological time. Science 163 (3867), 570.

Gaus, I., 2010. Role and impact of CO2-rock interactions during CO2 storage in sedimentary rocks. Int. J. Greenh. Gas Control 4 (1), 73–89.

Ge, S.M., 1997. A governing equation for fluid flow in rough fractures. Water Resour. Res. 33 (1), 53–61.

Gentier, S., Lamontagne, E., Archambault, G., Riss, J., 1997. Anisotropy of flow in a fracture undergoing shear and its relationship to the direction of shearing and injection pressure. Int. J. Rock Mech. Min. Sci. 34 (3-4), 94.

Gillespie, P.A., Walsh, J.J., Watterson, J., Bonson, C.G., Manzocchi, T., 2001. Scaling relationships of joint and vein arrays from The Burren, Co. Clare, Ireland. J. Struct. Geol. 23 (2-3), 183–201.

Glass, R., Nicholl, M., 1995. Quantitative visualization of entrapped phase dissolution within a horizontal flowing fracture. Geophys. Res. Lett. 22 (11), 1413–1416.

Glass, R., Nicholl, M., Tidwell, V., 1995. Challenging models for flow in unsaturated, fractured rock through exploration of small scale processes. Geophys. Res. Lett. 22 (11), 1457–1460.

Glass, R.J., Nicholl, M.J., Yarrington, L., 1998. A modified invasion percolation model for low-capillary number immiscible displacements in horizontal rough-walled fractures: influence of local in-plane curvature. Water Resour. Res. 34 (12), 3215–3234.

Glass, R.J., Rajaram, H., Detwiler, R.L., 2003. Immiscible displacements in rough-walled fractures: competition between roughening by random aperture variations and smoothing by in-plane curvature. Phys. Rev. E 68 (6), 061110.

Glover, P.W.J., Matsuki, K., Hikima, R., Hayashi, K., 1997. Fluid flow in fractally rough synthetic fractures. Geophys. Res. Lett. 24 (14), 1803–1806.

Grasselli, G., 2006. Manuel Rocha Medal recipient – shear strength of rock joints based on quantified surface description. Rock Mech. Rock. Eng. 39 (4), 295–314.

Grasselli, G., Wirth, J., Egger, P., 2002. Quantitative three-dimensional description of a rough surface and parameter evolution with shearing. Int. J. Rock Mech. Min. Sci. 39 (6), 789–800.

Gratier, J.P., 2011. Fault permeability and strength evolution related to fracturing and healing episodic processes (years to millennia): the role of pressure solution. Oil Gas Sci. Technol. Rev. IFP Energ. Nouvelles 66 (3), 491–506.

Grigoli, F., Cesca, S., Priolo, E., Rinaldi, A.P., Clinton, J.F., Stabile, T.A., Dost, B., Fernandez, M.G., Wiemer, S., Dahm, T., 2017. Current challenges in monitoring, discrimination, andmanagement of induced seismicity related to underground industrial activities: a European perspective. Rev. Geophys. 55 (2), 310–340.

Gudmundsson, A., 2011. Rock Fractures in Geological Processes. Cambridge University Press.

Gutfraind, R., Hansen, A., 1995. Study of fracture permeability using lattice-gas automata. Transp. Porous Media 18 (2), 131–149.

Gutierrez, M., Oino, L.E., Nygard, R., 2000. Stress-dependent permeability of a de-mineralised fracture in shale. Mar. Pet. Geol. 17 (8), 895–907.

Hakami, E., Larsson, E., 1996. Aperture measurements and flow experiments on a single natural fracture. Int. J. Rock Mech. Min. Sci. Geomech. Abstr. 33 (4), 395–404.

Hale, S., Naab, C., Butscher, C., Blum, P., 2019. Method comparison to determine hydraulic apertures of natural fractures. Rock Mech. Rock. Eng. 1–10.

Hansberry, R.L., King, R., Collins, A.S., Morley, C.K., 2014. Complex structure of an upper-level shale detachment zone: Khao Khwang fold and thrust belt, Central Thailand. J. Struct. Geol. 67, 140–153.

He, X.Y., Luo, L.S., 1997. Lattice Boltzmann model for the incompressible Navier-Stokes equation. J. Stat. Phys. 88 (3-4), 927–944.

Heffer, K., Lean, J., 1993. Earth stress orientation – a control on, and guide to, flooding directionality in a majority of reservoirs. In: Reservoir Characterization III, pp. 799–822.

Heller, R., Vermylen, J., Zoback, M., 2014. Experimental investigation of matrix permeability of gas shales. AAPG Bull. 98 (5), 975–995.

Hilgers, C., Urai, J.L., 2002. Experimental study of syntaxial vein growth during lateral fluid flow in transmitted light: first results. J. Struct. Geol. 24 (6), 1029–1043.

Hilgers, C., Dilg-Gruschinski, K., Urai, J.L., 2004. Microstructural evolution of syntaxial veins formed by advective flow. Geology 32 (3), 261–264.

Hooker, J.N., Katz, R.F., 2015. Vein spacing in extending, layered rock: the effect of synkinematic cementation. Am. J. Sci. 315 (6), 557–588.

Hooker, J.N., Gomez, L.A., Laubach, S.E., Gale, J.F.W., Marrett, R., 2012. Effects of diagenesis (cement precipitation) during fracture opening on fracture aperture-size scaling in carbonate rocks. In: Garland, J., Neilson, J.E., Laubach, S.E., Whidden, K.J. (Eds.), Advances in Carbonate Exploration and Reservoir Analysis. Geological Society Special Publicationpp. 187–206.

Hooker, J.N., Laubach, S.E., Marrett, R., 2013. Fracture-aperture size-frequency, spatial distribution, and growth processes in strata-bounded and non-strata-bounded fractures, Cambrian Meson Group, NW Argentina. J. Struct. Geol. 54, 54–71.

Hooker, J.N., Laubach, S.E., Marrett, R., 2014. A universal power-law scaling exponent for fracture apertures in sandstones. Geol. Soc. Am. Bull. 126 (9-10), 1340–1362.

Hooker, J.N., Huggett, J.M., Cartwright, J., Ali Hussein, M., 2017. Regional-scale development of opening-mode calcite veins due to silica diagenesis. Geochem. Geophys. Geosyst. 18 (7), 2580–2600.

Hooker, J.N., Laubach, S.E., Marrett, R., 2018. Microfracture spacing distributions and the evolution of fracture patterns in sandstones. J. Struct. Geol. 108, 66–79.

Hooker, J.N., Abu-Mahfouz, I.S., Meng, Q., Cartwright, J., 2019. Fractures in mudrocks: advances in constraining timing and understanding mechanisms. J. Struct. Geol. 125, 166–173.

Hopkins, D.L., Cook, N.G.W., Myer, L.R., 1990. Normal joint stiffness as a function of spatial geometry and surface-roughness. Rock Joints 203–210.

Houben, M.E., van Eeden, J.C.M., Barnhoorn, A., Hangx, S.J.T., 2020. Fracture-induced permeability in Whitby mudstone. Environ. Sci. Technol. 54 (15), 9564–9572.

Hu, Q.H., Ewing, R.P., Dultz, S., 2012. Low pore connectivity in natural rock. J. Contam. Hydrol. 133, 76–83.

Hu, R., Zhou, C.X., Wu, D.S., Yang, Z.B., Chen, Y.F., 2019. Roughness control on multiphase flow in rock fractures. Geophys. Res. Lett. 46 (21), 12002–12011.

Huang, S., Oelfke, S., Speck, R., 1992. Applicability of fractal characterization and modelling to rock joint profiles. In: International Journal of rock Mechanics and Mining Sciences & Geomechanics Abstracts. Elsevier, pp. 89–98.

Huang, T.H., Chang, C.S., Chao, C.Y., 2002. Experimental and mathematical modeling for fracture of rock joint with regular asperities. Eng. Fract. Mech. 69 (17), 1977–1996.

Huang, N., Liu, R.C., Jiang, Y.Y., Li, B., Yu, L.Y., 2018. Effects of fracture surface roughness and shear displacement on geometrical and hydraulic properties of three-dimensional crossed rock fracture models. Adv. Water Resour. 113, 30–41.

Huang, N., Jian, Y.J., Liu, R.C., Li, B., Sugimoto, S., 2019. A novel three-dimensional discrete fracture network model for investigating the role of aperture heterogeneity on fluid flow through fractured rock masses. Int. J. Rock Mech. Min. Sci. 116, 25–37.

Huang, B., Li, L., Tan, Y., Hu, R., Li, X., 2020. Investigating the meso-mechanical anisotropy and fracture surface roughness of continental shale. J. Geophys. Res. Solid Earth 125 (8), e2019JB017828.

Hughes, R.G., Blunt, M.J., 2001. Network modeling of multiphase flow in fractures. Adv. Water Resour. 24 (3-4), 409–421.

Huo, D., Benson, S.M., 2016. Experimental investigation of stress-dependency of relative permeability in rock fractures. Transp. Porous Media 113 (3), 567–590.

Huppert, H.E., Neufeld, J.A., 2014. The fluid mechanics of carbon dioxide sequestration. Annu. Rev. Fluid Mech. 46, 255–272.

Hustrulid, W., Johnson, G.A., 1990. Rock Mechanics Contributions and Challenges: Proceedings of the 31st US Symposium on Rock Mechanics. Taylor & Francis.

Ilgen, A.G., Heath, J.E., Akkutlu, I.Y., Bryndzia, L.T., Cole, D.R., Kharaka, Y.K., Kneafsey, T.J., Milliken, K.L., Pyrak-Nolte, L.J., Suarez-Rivera, R., 2017. Shales at all scales: exploring coupled processes in mudrocks. Earth Sci. Rev. 166, 132–152.

Indraratna, B., Kumara, C., Zhu, S.P., Sloan, S., 2015. Mathematical modeling and experimental verification of fluid flow through deformable rough rock joints. Int. J. Geomech. 15 (4).

Ingraffea, A.R., 1987. Theory of crack initiation and propagation in rock. In: Atkinson, B.K. (Ed.), Fracture Mechanics of Rock. Academic Press, London, pp. 71–110.

Ingram, G.M., Urai, J.L., 1997. Sealing processes and top seal assessment. Nor. Pet. Soc. 7, 165–174.

Ingram, G.M., Urai, J.L., 1999. Top-seal leakage through faults and fractures: the role of mudrock properties. Geol. Soc. Lond. 158, 125–135.

IPCC, 2014. Mitigation of climate change. In: Contribution of Working Group III to the Fifth Assessment Report of the Intergovernmental Panel on Climate Change. IPCC, Geneva, Switzerland, pp. 1454.

Ishibashi, T., Watanabe, N., Asanuma, H., Tsuchiya, N., 2016. Linking microearthquakes to fracture permeability change: the role of surface roughness. Geophys. Res. Lett. 43 (14), 7486–7493.

Ito, T., Zoback, M.D., 2000. Fracture permeability and in situ stress to 7 km depth in the KTB Scientific Drillhole. Geophys. Res. Lett. 27 (7), 1045–1048.

Jackson, R.E., Gorody, A.W., Mayer, B., Roy, J.W., Ryan, M.C., Van Stempvoort, D.R., 2013. Groundwater protection and unconventional gas extraction: the critical need for field-based hydrogeological research. Ground Water 51 (4), 488–510.

Jaeger, J.C., Cook, N.G.W., Zimmerman, R., 2009. Fundamentals of Rock Mechanics. Wiley.

Javadi, M., Sharifzadeh, M., Shahriar, K., Mitani, Y., 2014. Critical Reynolds number for nonlinear flow through rough-walled fractures: the role of shear processes. Water Resour. Res. 50 (2), 1789–1804.

Jeyakumaran, M., Rudnicki, J.W., Keer, L.M., 1992. Modeling slip zones with triangular dislocation elements. Bull. Seismol. Soc. Am. 82 (5), 2153–2169.

Jia, Y., Lu, Y., Tang, J., Fang, Y., Xia, B., Ge, Z., 2018. Mechanical-chemical-mineralogical controls on permeability evolution of shale fractures. Geofluids 2018, 7801843.

Jing, L., 2003. A review of techniques, advances and outstanding issues in numerical modelling for rock mechanics and rock engineering. Int. J. Rock Mech. Min. Sci. 40 (3), 283–353.

Johnston, J.D., McCaffrey, K.J.W., 1996. Fractal geometries of vein systems and the variation of scaling relationships with mechanism. J. Struct. Geol. 18 (2-3), 349–358.

Johri, M., Zoback, M.D., Hennings, P., 2014. A scaling law to characterize fault-damage zones at reservoir depths. AAPG Bull. 98 (10), 2057–2079.

Jolley, S.J., London, G.S.o., 2007. Structurally Complex Reservoirs. Geological Society.

Jones, T.A., Detwiler, R.L., 2016. Fracture sealing by mineral precipitation: the role of small-scale mineral heterogeneity. Geophys. Res. Lett. 43 (14), 7564–7571.

Ju, Y., Zhang, Q.G., Zheng, J.T., Chang, C., Xie, H.P., 2017. Fractal model and Lattice Boltzmann method for characterization of non-darcy flow in rough fractures. Sci. Rep. 7.

Kabuth, A., Dahmke, A., Beyer, C., Bilke, L., Dethlefsen, F., Dietrich, P., Duttmann, R., Ebert, M., Feeser, V., Gorke, U.J., Kober, R., Rabbel, W., Schanz, T., Schafer, D., Wurdemann, H., Bauer, S., 2017. Energy storage in the geological subsurface: dimensioning, risk analysis and spatial planning: the ANGUS plus project. Environ. Earth Sci. 76 (1).

Kampman, N., 2018. Opening Versus Self-Sealing Behaviour Of Single Fractures In Mudstone Caprocks During CO2 Migration. Vol. 1. pp. 1–4.

Kampman, N., Maskell, A., Bickle, M.J., Evans, J.P., Schaller, M., Purser, G., Zhou, Z., Gattacceca, J., Peitre, E.S., Rochelle, C.A., Ballentine, C.J., Busch, A., Scientists of the, G, 2013. Scientific drilling and downhole fluid sampling of a natural CO2 reservoir, Green River, Utah. Sci. Dril. 16, 33–43.

Kampman, N., Bickle, M., Wigley, M., Dubacq, B., 2014a. Fluid flow and CO2–fluid–mineral interactions during CO2-storage in sedimentary basins. Chem. Geol. 369, 22–50.

Kampman, N., Bickle, M.J., Maskell, A., Chapman, H.J., Evans, J.P., Purser, G., Zhou, Z., Schaller, M.F., Gattacceca, J.C., Bertier, P., Chen, F., Turchyn, A.V., Assayag, N., Rochelle, C., Ballentine, C.J., Busch, A., 2014b. Drilling and sampling a natural CO2 reservoir: implications for fluid flow and CO2-fluid-rock reactions during CO2 migration through the overburden. Chem. Geol. 369, 51–82.

Karpyn, Z.T., Piri, M., 2007. Prediction of fluid occupancy in fractures using network modeling and x-ray microtomography. I: data conditioning and model description. Phys. Rev. E 76 (1), 016315.

Kattenhorn, S.A., Aydin, A., Pollard, D.D., 2000. Joints at high angles to normal fault strike: an explanation using 3-D numerical models of fault-perturbed stress fields. J. Struct. Geol. 22 (1), 1–23.

Keller, A.A., Roberts, P.V., Kitanidis, P.K., 1995. Prediction of single phase transport parameters in a variable aperture fracture. Geophys. Res. Lett. 22 (11), 1425–1428.

Keyence, 2017. Digitial Microscope VHX-6000 User's Manual.

Kim, I., Lindquist, W.B., Durham, W.B., 2003. Fracture flow simulation using a finite-difference lattice Boltzmann method. Phys. Rev. E 67 (4).

Kim, Y.-S., Peacock, D.C., Sanderson, D.J., 2004. Fault damage zones. J. Struct. Geol. 26 (3), 503–517.

King Hubbert, M., Rubey, W.W., 1959. Role of fluid pressure in mechanics of overthrust faulting: I. Mechanics of fluid-filled porous solids and its application to overthrust faulting. Geol. Soc. Am. Bull. 70 (2), 115–166.

Kirkpatrick, J., Shipton, Z., Evans, J.P., Micklethwaite, S., Lim, S., McKillop, P., 2008. Strike-slip fault terminations at seismogenic depths: the structure and kinematics of the Glacier Lakes fault, Sierra Nevada United States. J. Geophys. Res. Solid Earth 113, B4.

Kishida, K., Sawada, A., Yasuhara, H., Hosoda, T., 2013. Estimation of fracture flow considering the inhomogeneous structure of single rock fractures. Soils Found. 53 (1), 105–116.

Klimczak, C., Schultz, R.A., Parashar, R., Reeves, D.M., 2010. Cubic law with aperture-length correlation: implications for network scale fluid flow. Hydrogeol. J. 18 (4), 851–862.

Kling, T., Schwarz, J.O., Wendler, F., Enzmann, F., Blum, P., 2017. Fracture flow due to hydrothermally induced quartz growth. Adv. Water Resour. 107, 93–107.

Klinkenberg, L.J., 1941. The permeability of porous media to gases and liquids. In: Drilling and Production Practice, pp. 200–213.

Knackstedt, M.A., Sheppard, A.P., Sahimi, M., 2001. Pore network modelling of two-phase flow in porous rock: the effect of correlated heterogeneity. Adv. Water Resour. 24 (3-4), 257–277.

Koh, J., Roshan, H., Rahman, S.S., 2011. A numerical study on the long term thermo-

poroelastic effects of cold water injection into naturally fractured geothermal reservoirs. Comput. Geotech. 38 (5), 669–682.

Konzuk, J.S., Kueper, B.H., 2004. Evaluation of cubic law based models describing single-phase flow through a rough-walled fracture. Water Resour. Res. 40 (2).

Kosakowski, G., Berkowitz, B., 1999. Flow pattern variability in natural fracture intersections. Geophys. Res. Lett. 26 (12), 4466–4479.

Koudina, N., Garcia, R.G., Thovert, J.F., Adler, P.M., 1998. Permeability of three-dimensional fracture networks. Phys. Rev. E 57 (4), 4466–4479.

Koyama, T., Neretnieks, I., Jing, L., 2008. A numerical study on differences in using Navier-Stokes and Reynolds equations for modeling the fluid flow and particle transport in single rock fractures with shear. Int. J. Rock Mech. Min. Sci. 45 (7), 1082–1101.

Kulander, B.R., Dean, S.L., Ward Jr., B.J., 1990. Fractured Core Analysis: Interpretation, Logging, and Use of Natural and Induced Fractures in Core. American Association of Petroleum Geologists.

Kulatilake, P., Balasingam, P., Park, J., Morgan, R., 2006. Natural rock joint roughness quantification through fractal techniques. Geotech. Geol. Eng. 24 (5), 1181.

Lamarche, J., Chabani, A., Gauthier, B.D.M., 2018. Dimensional threshold for fracture linkage and hooking. J. Struct. Geol. 108, 171–179.

Lammers, P., Beronov, K.N., Volkert, R., Brenner, G., Durst, F., 2006. Lattice BGK direct numerical simulation of fully developed turbulence in incompressible plane channel flow. Comput. Fluids 35 (10), 1137–1153.

Lander, R.H., Laubach, S.E., 2015. Insights into rates of fracture growth and sealing from a model for quartz cementation in fractured sandstones. GSA Bull. 127 (3-4), 516–538.

Landry, C.J., Eichhubl, P., Prodanović, M., Wilkins, S., 2016. Nanoscale grain boundary channels in fracture cement enhance flow in mudrocks. J. Geophys. Res. Solid Earth 121 (5), 3366–3376.

Latham, J.P., Xiang, J.S., Belayneh, M., Nick, H.M., Tsang, C.F., Blunt, M.J., 2013. Modelling stress-dependent permeability in fractured rock including effects of propagating and bending fractures. Int. J. Rock Mech. Min. Sci. 57, 100–112.

Laubach, S.E., 2003. Practical approaches to identifying sealed and open fractures. AAPG Bull. 87 (4), 561–579.

Laubach, S.E., Olson, J.E., Gale, J.F.W., 2004. Are open fractures necessarily aligned with maximum horizontal stress? Earth Planet. Sci. Lett. 222, 191–195.

Laubach, S.E., Olson, J.E., Gross, M.R., 2009. Mechanical and fracture stratigraphy. AAPG Bull. 93 (11), 1413–1426.

Laubach, S.E., Fall, A., Copley, L.K., Marrett, R., Wilkins, S.J., 2016. Fracture porosity creation and persistence in a basement-involved Laramide fold, Upper Cretaceous Frontier Formation, Green River Basin, USA. Geol. Mag. 153 (5-6), 887–910.

Laubach, S.E., Lamarche, J., Gauthier, B.D.M., Dunne, W.M., Sanderson, D.J., 2018. Spatial arrangement of faults and opening-mode fractures. J. Struct. Geol. 108, 2–15.

Laubach, S.E., Lander, R.H., Criscenti, L.J., Anovitz, L.M., Urai, J.L., Pollyea, R.M., Hooker, J.N., Narr, W., Evans, M.A., Kerisit, S.N., Olson, J.E., Dewers, T., Fisher, D., Bodnar, R., Evans, B., Dove, P., Bonnell, L.M., Marder, M.P., Pyrak-Nolte, L., 2019. The role of chemistry in fracture pattern development and opportunities to advance interpretations of geological materials. Rev. Geophys. 57 (3), 1065–1111.

Lee, H.S., Cho, T.F., 2002. Hydraulic characteristics of rough fractures in linear flow under normal and shear load. Rock Mech. Rock. Eng. 35 (4), 299–318.

Lee, Y.-J., Morse, J.W., 1999. Calcite precipitation in synthetic veins: implications for the time and fluid volume necessary for vein filling. Chem. Geol. 156 (1), 151–170.

Lee, S.H., Lee, K.K., Yeo, I.W., 2014. Assessment of the validity of Stokes and Reynolds equations for fluid flow through a rough-walled fracture with flow imaging. Geophys. Res. Lett. 41 (13), 4578–4585.

Lee, H.P., Olson, J.E., Holder, J., Gale, J.F.W., Myers, R.D., 2015. The interaction of propagating opening mode fractures with preexisting discontinuities in shale. J. Geophys. Res. Solid Earth 120 (1), 169–181.

Lei, Q.H., Wang, X.G., Xiang, J.S., Latham, J.P., 2017. Polyaxial stress-dependent permeability of a three-dimensional fractured rock layer. Hydrogeol. J. 25 (8), 2251–2262.

Lemarchand, E., Davy, C.A., Dormieux, L., Skoczylas, F., 2010. Tortuosity effects in coupled advective transport and mechanical properties of fractured geomaterials. Transp. Porous Media 84 (1), 1–19.

Li, Y.R., Huang, R.Q., 2015. Relationship between joint roughness coefficient and fractal dimension of rock fracture surfaces. Int. J. Rock Mech. Min. Sci. 75, 15–22.

Li, B., Jiang, Y.J., Koyama, T., Jing, L.R., Tanabashi, Y., 2008. Experimental study of the hydro-mechanical behavior of rock joints using a parallel-plate model containing contact areas and artificial fractures. Int. J. Rock Mech. Min. Sci. 45 (3), 362–375.

Liu, E.R., 2005. Effects of fracture aperture and roughness on hydraulic and mechanical properties of rocks: implication of seismic characterization of fractured reservoirs. J. Geophys. Eng. 2 (1), 38–47.

Liu, R., He, M., Huang, N., Jiang, Y., Yu, L., 2020. Three-dimensional double-rough-walled modeling of fluid flow through self-affine shear fractures. J. Rock Mech. Geotech. Eng. 12 (1), 41–49.

Long, J.C.S., Billaux, D.M., 1987. From field data to fracture network modelling – an example incorporating spatial structure. Water Resour. Res. 23 (7), 1201–1216.

Long, J.C.S., Witherspoon, P.A., 1985. The relationship of the degree of interconnection to permeability in fracture networks. J. Geophys. Res. Solid Earth Planets 90 (NB4), 3087–3098.

Louis, C., 1969. A study of groundwater flow in jointed rock and its influence on the stability of rock masses. Imp. Coll. Rock Mech. Res. Rep. 10, 90.

Lunn, R.J., Willson, J.P., Shipton, Z.K., Moir, H., 2008. Simulating brittle fault growth from linkage of preexisting structures. J. Geophys. Res. Solid Earth 113, B7.

Luo, X., Wang, J.H., Dooner, M., Clarke, J., 2015. Overview of current development in electrical energy storage technologies and the application potential in power system operation. Appl. Energy 137, 511–536.

Luo, S., Zhao, Z.H., Peng, H., Pu, H., 2016. The role of fracture surface roughness in macroscopic fluid flow and heat transfer in fractured rocks. Int. J. Rock Mech. Min. Sci. 87, 29–38.

Madadi, M., VanSiclen, C.D., Sahimi, M., 2003. Fluid flow and conduction in two-dimensional fractures with rough, self-affine surfaces: a comparative study. Geophys. Res. Lett. 27, 2989–2992.

Maerten, L., Gillespie, P., Pollard, D.D., 2002. Effects of local stress perturbation on secondary fault development. J. Struct. Geol. 24 (1), 145–153.

Maerten, L., Gillespie, P., Daniel, J.M., 2006. Three-dimensional geomechanical modeling for constraint of subseismic fault simulation. AAPG Bull. 90 (9), 1337–1358.

Maerten, F., Maerten, L., Pollard, D.D., 2014. iBem3D, a three-dimensional iterative boundary element method using angular dislocations for modeling geologic structures. Comput. Geosci. 72, 1–17.

Makurat, A., Gutierrez, L., Backer, L., 1997. Fracture Flow and Fracture Cross Flow Experiments. Vol. 7. Norwegian Petroleum Society Special Publications, pp. 139–148.

Mandl, G., Harkness, R., 1987. Hydrocarbon migration by hydraulic fracturing. Geol. Soc. Lond., Spec. Publ. 29 (1), 39–53.

Marrett, R., Ortega, O.J., Kelsey, C.M., 1999. Extent of power-law scaling for natural fractures in rock. Geology 27 (9), 799–802.

Massiot, C., Townend, J., Nicol, A., McNamara, D.D., 2015. Fracture Width and Spacing Distributions from Borehole televiewer Logs and Cores in the Rotokawa Geothermal Field, New Zealand, World Geothermal Congress 2015. International Geothermal Association.

Matsuki, K., Lee, J.J., Sakaguchi, K., Hayashi, K., 1999. Size effect in flow conductance of a closed small-scale hydraulic fracture in granite. Geotherm. Sci. Technol. 6, 113–138.

McCartney, J.S., Sanchez, M., Tomac, I., 2016. Energy geotechnics: advances in subsurface energy recovery, storage, exchange, and waste management. Comput. Geotech. 75, 244–256.

McDermott, C., Kolditz, O., 2006. Geomechanical model for fracture deformation under hydraulic, mechanical and thermal loads. Hydrogeol. J. 14 (4), 485–498.

McGinnis, R.N., Ferrill, D.A., Morris, A.P., Smart, K.J., Lehrmann, D., 2017. Mechanical stratigraphic controls on natural fracture spacing and penetration. J. Struct. Geol. 95, 160–170.

Meheust, Y., Schmittbuhl, J., 2000. Flow enhancement of a rough fracture. Geophys. Res. Lett. 27 (18), 2989–2992.

Meheust, Y., Schmittbuhl, J., 2003. Scale effects related to flow in rough fractures. Pure Appl. Geophys. 160 (5-6), 1023–1050.

Mehmani, A., Prodanovic, M., Javadpour, F., 2013. Multiscale, multiphysics network modeling of shale matrix gas flows. Transp. Porous Media 99 (2), 377–390.

Metz, B., Davidson, O., De Coninck, H., Loos, M., Meyer, L., 2005. IPCC, 2005: IPCC Special Report on Carbon Dioxide Capture and Storage. Prepared by Working Group III of the Intergovernmental Panel on Climate Change. Cambridge University Press, Cambridge, United Kingdom and New York, NY, USA.

Min, K.B., Rutqvist, J., Tsang, C.F., Jing, L.R., 2004. Stress-dependent permeability of fractured rock masses: a numerical study. Int. J. Rock Mech. Min. Sci. 41 (7), 1191–1210.

Mo, P., Li, Y.R., 2019. Estimating the three-dimensional joint roughness coefficient value of rock fractures. Bull. Eng. Geol. Environ. 78 (2), 857–866.

Mokhtari, M., Tutuncu, A.N., Boitnott, G.N., 2015. Intrinsic anisotropy in fracture permeability. Interpretation A J. Subsurf. Charact. 3 (3), ST43–ST53.

Moreno, L., Tsang, Y.W., Tsang, C.F., Hale, F.V., Neretnieks, I., 1988. Flow and tracer transport in a single fracture – A stochastic-model and its relation to some field observations. Water Resour. Res. 24 (12), 2033–2048.

Mourzenko, V.V., Thovert, J.F., Adler, P.M., 1995. Permeability of a single fracture – validity of the Reynolds-equation. J. Phys. II 5 (3), 465–482.

Moutsopoulos, K.N., 2009. Exact and approximate analytical solutions for unsteady fully developed turbulent flow in porous media and fractures for time dependent boundary conditions. J. Hydrol. 369 (1-2), 78–89.

Mualem, Y., 1976. A new model for predicting the hydraulic conductivity of unsaturated porous media. Water Resour. Res. 12 (3), 513–522.

Mualem, Y., 1978. Hydraulic conductivity of unsaturated porous media: generalized macroscopic approach. Water Resour. Res. 14 (2), 325–334.

Murphy, J.R., Thomson, N., 1993. Two-phase flow in a variable aperture fracture. Water Resour. Res. 29 (10), 3453–3476.

Myer, L.R., 2000. Fractures as collections of cracks. Int. J. Rock Mech. Min. Sci. 37 (1-2), 231–243.

Myers, N.O., 1962. Characterization of surface roughness. Wear 5 (3), 182–189.

Nagel, N., Zhang, F., Sanchez-Nagel, M., Lee, B., Agharazi, A., 2013. Stress Shadow Evaluations for Completion Design in Unconventional Plays, SPE Unconventional Resources Conference Canada. Society of Petroleum Engineers, Calgary, Alberta, Canada, pp. 14.

Nazridoust, K., Ahmadi, G., Smith, D.H., 2006. A new friction factor correlation for laminar, single-phase flows through rock fractures. J. Hydrol. 329 (1-2), 315–328.

Nemoto, K., Watanabe, N., Hirano, N., Tsuchiya, N., 2009. Direct measurement of contact area and stress dependence of anisotropic flow through rock fracture with heterogeneous aperture distribution. Earth Planet. Sci. Lett. 281 (1-2), 81–87.

Nicholl, M.J., Rajaram, H., Glass, R.J., Detwiler, R., 1999. Saturated flow in a single fracture: evaluation of the Reynolds equation in measured aperture fields. Water Resour. Res. 35 (11), 3361–3373.

Novakowski, K.S., Lapcevic, P.A., Voralek, J., Bickerton, G., 1995. Preliminary interpretation of tracer experiments conducted in a discrete rock fracture under conditions of natural flow. Geophys. Res. Lett. 22 (11), 1417–1420.

Nowamooz, A., Radilla, G., Fourar, M., 2009. Non-Darcian two-phase flow in a transparent replica of a rough-walled rock fracture. Water Resour. Res. 45.

Nussbaum, C., Bossart, P., Amann, F., Aubourg, C., 2011. Analysis of tectonic structures and excavation induced fractures in the Opalinus Clay, Mont Terri underground rock laboratory (Switzerland). Swiss J. Geosci. 104 (2), 187–210.

Nygard, R., Gutierrez, M., Gautam, R., Hoeg, K., 2004. Compaction behavior of argillaceous sediments as function of diagenesis. Mar. Pet. Geol. 21 (3), 349–362.

Nygard, R., Gutierrez, M., Bratli, R.K., Hoeg, K., 2006. Brittle-ductile transition, shear failure and leakage in shales and mudrocks. Mar. Pet. Geol. 23 (2), 201–212.

Obeysekara, A., Lei, Q., Salinas, P., Pavlidis, D., Xiang, J., Latham, J.P., Pain, C.C., 2018. Modelling stress-dependent single and multi-phase flows in fractured porous media based on an immersed-body method with mesh adaptivity. Comput. Geotech. 103, 229–241.

Odling, N., 1994. Natural fracture profiles, fractal dimension and joint roughness coefficients. Rock Mech. Rock. Eng. 27 (3), 135–153.

Odling, N.E., Gillespie, P., Bourgine, B., Castaing, C., Chiles, J.P., Christensen, N.P., Fillion, E., Genter, A., Olsen, C., Thrane, L., Trice, R., Aarseth, E., Walsh, J.J., Watterson, J., 1999. Variations in fracture system geometry and their implications for fluid flow in fractured hydrocarbon reservoirs. Pet. Geosci. 5 (4), 373–384.

Oh, J., Kim, K.-Y., Han, W.S., Kim, T., Kim, J.-C., Park, E., 2013. Experimental and numerical study on supercritical CO2/brine transport in a fractured rock: implications of mass transfer, capillary pressure and storage capacity. Adv. Water Resour. 62, 442–453.

Olasolo, P., Juarez, M.C., Morales, M.P., D'Amico, S., Liarte, I.A., 2016. Enhanced geothermal systems (EGS): a review. Renew. Sustain. Energy Rev. 56, 133–144.

Olson, J.E., Pollard, D.D., 1991. The initiation and growth of en-chelon veins. J. Struct. Geol. 13 (5), 595–608.

Olson, J.E., Laubach, S.E., Lander, R.H., 2007. Combining diagenesis and mechanics to quantify fracture aperture distributions and fracture pattern permeability. Geol. Soc. Lond., Spec. Publ. 270 (1), 101–116.

Olson, J.E., Laubach, S.E., Lander, R.H., 2009. Natural fracture characterization in tight gas sandstones: Integrating mechanics and diagenesis. AAPG Bull. 93 (11), 1535–1549.

Olsson, R., Barton, N., 2001. An improved model for hydromechanical coupling during shearing of rock joints. Int. J. Rock Mech. Min. Sci. 38 (3), 317–329.

Olsson, W.A., Brown, S.R., 1993. Hydromechanical response of a fracture undergoing compression and shear. Int. J. Rock Mech. Min. Sci. Geomech. Abstr. 30 (7), 845–851.

Oron, A.P., Berkowitz, B., 1998. Flow in rock fractures: the local cubic law assumption reexamined. Water Resour. Res. 34 (11), 2811–2825.

Ortega, O.J., Marrett, R.A., Laubach, S.E., 2006. A scale-independent approach to fracture intensity and average spacing measurement. AAPG Bull. 90 (2), 193–208.

Perfect, E., 1997. Fractal models for the fragmentation of rocks and soils: a review. Eng. Geol. 48 (3-4), 185–198.

Persoff, P., Pruess, K., 1995. Two-phase flow visualization and relative permeability measurement in natural rough-walled rock fractures. Water Resour. Res. 31 (5), 1175–1186.

Philip, Z.G., Jennings, J.W., Olson, J.E., Laubach, S.E., Holder, J., 2005. Modeling coupled fracture-matrix fluid flow in geomechanically simulated fracture networks. SPE Reserv. Eval. Eng. 8 (4), 300–309.

Plouraboue, F., Kurowski, P., Boffa, J.M., Hulin, J.P., Roux, S., 2000. Experimental study of the transport properties of rough self-affine fractures. J. Contam. Hydrol. 46 (3-4), 295–318.

Pollard, D.D., Aydin, A., 1988. Progress in understanding jointing over the past century. Geol. Soc. Am. Bull. 100 (8), 1181–1204.

Poon, C., Sayles, R., Jones, T., 1992. Surface measurement and fractal characterization of naturally fractured rocks. J. Phys. D. Appl. Phys. 25 (8), 1269.

Power, W.L., Tullis, T.E., 1991. Euclidean and fractal models for the description of rock surface roughness. J. Geophys. Res. Solid Earth 96 (B1), 415–424.

Priest, S.D., Hudson, J.A., 1976. Discontinuity spacing in rock. Int. J. Rock Mech. Min. Sci. 13 (5), 135–148.

Pruess, K., Tsang, Y., 1990. On two-phase relative permeability and capillary pressure of rough-walled rock fractures. Water Resour. Res. 26 (9), 1915–1926.

Pyrak-Nolte, L.J., Morris, J.P., 2000. Single fractures under normal stress: the relation between fracture specific stiffness and fluid flow. Int. J. Rock Mech. Min. Sci. 37 (1-2), 245–262.

Pyrak-Nolte, L.J., Myer, L.R., Cook, N.G.W., Witherspoon, P.A., 1987. Hydraulic and mechanical properties of natural fractures in low permeability rock. In: Proceedings of the 6th International Congress on Rock Mechanics, pp. 225–231.

Pyrak-Nolte, L.J., Cook, N.G.W., Nolte, D.D., 1988. Fluid percolation through single fractures. Geophys. Res. Lett. 15 (11), 1247–1250.

Qian, Y.H., Dhumieres, D., Lallemand, P., 1992. Lattice BGK models for Navier-Stokes equation. Europhys. Lett. 17 (6BIS), 479–484.

Qian, J.Z., Zhan, H.B., Zhao, W.D., Sun, F.G., 2005. Experimental study of turbulent unconfined groundwater flow in a single fracture. J. Hydrol. 311 (1-4), 134–142.

Qian, J.Z., Zhan, H.B., Luo, S.H., Zhao, W.D., 2007. Experimental evidence of scale-dependent hydraulic conductivity for fully developed turbulent flow in a single fracture. J. Hydrol. 339 (3-4), 206–215.

Qian, J.Z., Chen, Z., Zhan, H.B., Guan, H.C., 2011. Experimental study of the effect of roughness and Reynolds number on fluid flow in rough-walled single fractures: a check of local cubic law. Hydrol. Process. 25 (4), 614–622.

Qian, J.Z., Liang, M., Chen, Z., Zhan, H.B., 2012. Eddy correlations for water flow in a single fracture with abruptly changing aperture. Hydrol. Process. 26 (22), 3369–3377.

Radilla, G., Nowamooz, A., Fourar, M., 2013. Modeling non-darcian single- and two-phase flow in transparent replicas of rough-walled rock fractures. Transp. Porous Media 98 (2), 401–426.

Ranjith, P.G., Darlington, W., 2007. Nonlinear single-phase flow in real rock joints. Water Resour. Res. 43 (9).

Ranjith, P.G., Viete, D.R., 2011. Applicability of the 'cubic law' for non-Darcian fracture flow. J. Pet. Sci. Eng. 78 (2), 321–327.

Rasmuson, A., Neretnieks, I., 1986. Radionuclide transport in fast channels in crystalline rock. Water Resour. Res. 22 (8), 1247–1256.

Rasouli, V., Hosseinian, A., 2011. Correlations developed for estimation of hydraulic parameters of rough fractures through the simulation of JRC flow channels. Rock Mech. Rock. Eng. 44 (4), 447–461.

Raven, K.G., Gale, J.E., 1985. Water-flow in a natural rock fracture as a function of stress and sample-size. Int. J. Rock Mech. Min. Sci. 22 (4), 251–261.

Raven, K.G., Novakowski, K.S., Lapcevic, P.A., 1988. Interpretation of field tracer tests of a single fracture using a transient solute storage model. Water Resour. Res. 24 (12), 2019–2032.

Rawnsley, K.D., Rives, T., Petit, J.P., Hencher, S.R., Lumsden, A.C., 1992. Joint development in perturbed stress fields near faults. J. Struct. Geol. 14 (8-9), 939–951.

Read, R.S., 2004. 20 years of excavation response studies at AECL's Underground Research Laboratory. Int. J. Rock Mech. Min. Sci. 41 (8), 1251–1275.

Reitsma, S., Kueper, B.H., 1994. Laboratory measurement of capillary pressure-saturation relationships in a rock fracture. Water Resour. Res. 30 (4), 865–878.

Renshaw, C.E., 1995. On the relationship between mechanical and hydraulic apertures in rough-walled fractures. J. Geophys. Res. Solid Earth 100 (B12), 24629–24636.

Renshaw, C.E., Park, J.C., 1997. Effect of mechanical interactions on the scaling of fracture length and aperture. Nature 386 (6624), 482–484.

Reston, T., McDermott, K., 2014. An assessment of the cause of the 'extension discrepancy' with reference to the west Galicia margin. Basin Res. 26 (1), 135–153.

Riedel, M., Collett, T.S., Kumar, P., Sathe, A.V., Cook, A., 2010. Seismic imaging of a fractured gas hydrate system in the Krishna-Godavari Basin offshore India. Mar. Pet. Geol. 27 (7), 1476–1493.

Roberts, S.J., Nunn, J.A., 1995. Episodic fluid expulsion from geopressured sediments. Mar. Pet. Geol. 12 (2), 195–204.

Rogers, S.F., 2003. Critical stress-related permeability in fractured rocks. In: Ameen, M.S. (Ed.), Fracture and in-Situ Stress Characterization of Hydrocarbon Reservoirs. Geological Society Special Publication, pp. 7–16.

Romm, E., 1966. Flow Characteristics of Fractured Rocks. Nedra, Moscow, pp. 283.

Rong, G., Yang, J., Cheng, L., Zhou, C.B., 2016. Laboratory investigation of nonlinear flow characteristics in rough fractures during shear process. J. Hydrol. 541, 1385–1394.

Ross, D.J.K., Bustin, R.M., 2009. The importance of shale composition and pore structure upon gas storage potential of shale gas reservoirs. Mar. Pet. Geol. 26 (6), 916–927.

Roy, A., Perfect, E., Dunne, W.M., McKay, L.D., 2007. Fractal characterization of fracture networks: an improved box-counting technique. J. Geophys. Res. Solid Earth 112 (B12).

Rutqvist, J., 2015. Fractured rock stress-permeability relationships from in situ data and effects of temperature and chemical-mechanical couplings. Geofluids 15 (1-2), 48–66.

Rutqvist, J., Stephansson, O., 2003. The role of hydromechanical coupling in fractured rock engineering. Hydrogeol. J. 11 (1), 7–40.

Sanderson, D.J., Nixon, C.W., 2018. Topology, connectivity and percolation in fracture networks. J. Struct. Geol. 115, 167–177.

Sanderson, D.J., Zhang, X., 1999. Critical stress localization of flow associated with deformation of well-fractured rock masses, with implications for mineral deposits. In: McCaffrey, K., Lonergan, L., Wilkinson, J.J. (Eds.), Fractures, Fluid Flow and Mineralisation. Vol. 155. Geological Society Special Publication, pp. 69–81.

Scesi, L., Gattinoni, P., 2007. Roughness control on hydraulic conductivity in fractured rocks. Hydrogeol. J. 15 (2), 201–211.

Schmittbuhl, J., Gentier, S., Roux, S., 1993. Field-measurements of the roughness of fault surfaces. Geophys. Res. Lett. 20 (8), 639–641.

Schmittbuhl, J., Schmitt, F., Scholz, C., 1995. Scaling invariance of crack surfaces. J. Geophys. Res. Solid Earth Planets 100 (B4), 5953–5973.

Schmittbuhl, J., Steyer, A., Jouniaux, L., Toussaint, R., 2008. Fracture morphology and viscous transport. Int. J. Rock Mech. Min. Sci. 45 (3), 422–430.

Schultz, R.A., Soliva, R., Fossen, H., Okubo, C.H., Reeves, D.M., 2008. Dependence of displacement-length scaling relations for fractures and deformation bands on the volumetric changes across them. J. Struct. Geol. 30 (11), 1405–1411.

Sempere, J.C., Macdonald, K.C., 1986. Overlapping spreading centers: Implications from crack growth simulation by the displacement discontinuity method. Tectonics 5 (1), 151–163.

Sharifzadeh, M., Mitani, Y., Esaki, T., 2008. Rock joint surfaces measurement and analysis of aperture distribution under different normal and shear loading using GIS. Rock Mech. Rock. Eng. 41 (2), 299–323.

Shipton, Z.K., Soden, A.M., Kirkpatrick, J.D., Bright, A.M., Lunn, R.J., 2006. How Thick is a Fault? Fault Displacement-Thickness Scaling Revisited.

Sibson, R.H., 1996. Structural permeability of fluid-driven fault-fracture meshes. J. Struct. Geol. 18 (8), 1031–1042.

Sibson, R.H., 1998. Brittle failure mode plots for compressional and extensional tectonic regimes. J. Struct. Geol. 20 (5), 655–660.

Singurindy, O., Berkowitz, B., 2005. The role of fractures on coupled dissolution and precipitation patterns in carbonate rocks. Adv. Water Resour. 28 (5), 507–521.

Sisavath, S., Al-Yaarubi, A., Pain, C.C., Zimmerman, R.W., 2003. A simple model for deviations from the cubic law for a fracture undergoing dilation or closure. Pure Appl. Geophys. 160 (5-6), 1009–1022.

Skjetne, E., Hansen, A., Gudmundsson, J.S., 1999. High-velocity flow in a rough fracture. J. Fluid Mech. 383, 1–28.

Snow, D.T., 1969. Anisotropic permeability of fractured media. Water Resour. Res. 5 (6), 1273–1289.

Song, J., Zhang, D.X., 2013. Comprehensive review of caprock-sealing mechanisms for geologic carbon sequestration. Environ. Sci. Technol. 47 (1), 9–22.

Spokas, K., Peters, C.A., Pyrak-Nolte, L., 2018. Influence of rock mineralogy on reactive fracture evolution in carbonate-rich caprocks. Environ. Sci. Technol. 52 (17),

10144–10152.

Spokas, K., Fang, Y., Fitts, J.P., Peters, C.A., Elsworth, D., 2019. Collapse of reacted fracture surface decreases permeability and frictional strength. J. Geophys. Res. Solid Earth 124 (12), 12799–12811.

Stephanson, O., Jing, L., Tsang, C.F., 1997. Coupled Thermo-Hydro-Mechanical Processes of Fractured Media: Mathematical and Experimental Studies. Elsevier Science.

Stewart, I.S., Lewis, D., 2017. Communicating contested geoscience to the public: moving from 'matters of fact' to 'matters of concern'. Earth Sci. Rev. 174, 122–133.

Succi, S., 2001. The Lattice Boltzmann Equation: For Fluid Dynamics and Beyond. Clarendon Press.

Sukop, M.C., Thorne, D.T., 2007. Lattice Boltzmann Modeling: An Introduction for Geoscientists and Engineers. Springer Berlin Heidelberg.

Swan, G., 1983. Determination of stiffness and other joint properties from roughness measurements. Rock Mech. Rock. Eng. 16 (1), 19–38.

Taron, J., Elsworth, D., Min, K.-B., 2009. Numerical simulation of thermal-hydrologic-mechanical-chemical processes in deformable, fractured porous media. Int. J. Rock Mech. Min. Sci. 46 (5), 842–854.

Thomas, A.L., 1993. A Three-Dimensional, Polygonal Element, Displacement Discontinuity Boundary Element Computer Program with Applications to Fractures, Faults, and Cavities in the Earth's Crust (Masters thesis). Stanford University.

Thomas, A.L., Pollard, D.D., 1993. The geometry of echelon fractures in rock: implications from laboratory and numerical experiments. J. Struct. Geol. 15 (3-5), 323–334.

Thompson, M.E., Brown, S.R., 1991. The effect of anisotropic surface-roughness on flow and transport in fractures. J. Geophys. Res. Solid Earth Planets 96 (B13), 21923–21932.

Tian, F.B., Luo, H.X., Zhu, L.D., Liao, J.C., Lu, X.Y., 2011. An efficient immersed boundary-lattice Boltzmann method for the hydrodynamic interaction of elastic filaments. J. Comput. Phys. 230 (19), 7266–7283.

Tsang, Y.W., 1984. The effect of tortuosity on fluid-flow through a single fracture. Water Resour. Res. 20 (9), 1209–1215.

Tsang, Y.W., Tsang, C.F., 1987. Channel model of flow through fractured media. Water Resour. Res. 23 (3), 467–479.

Tsang, Y.W., Witherspoon, P.A., 1981. Hydromechanical behaviour of a deformable rock fracture subject to normal stress. J. Geophys. Res. 86 (NB10), 9287–9298.

Tse, R., Cruden, D.M., 1979. Estimating joint roughness coefficients. Int. J. Rock Mech. Min. Sci. 16 (5), 303–307.

Unger, A.J.A., Mase, C.W., 1993. Numerical study of the hydromechanical behavior of 2 rough fracture surfaces in contact. Water Resour. Res. 29 (7), 2101–2114.

van der Walt, S., Schonberger, J.L., Nunez-Iglesias, J., Boulogne, F., Warner, J.D., Yager, N., Gouillart, E., Yu, T., Scikit Image, C., 2014. scikit-image: image processing in Python. Peerj 2.

van Noort, R., Yarushina, V., 2016. Water and CO2 permeability of a shale sample core from Svalbard. In: Ask, M., Bruckman, V., Juhlin, C., Kempka, T., Kuhn, M. (Eds.), European Geosciences Union General Assembly 2016. Energy Procedia, pp. 67–74.

Vilarrasa, V., Koyama, T., Neretnieks, I., Jing, L., 2011. Shear-induced flow channels in a single rock fracture and their effect on solute transport. Transp. Porous Media 87, 503–523.

Virgo, S., Abe, S., Urai, J.L., 2014. The evolution of crack seal vein and fracture networks in an evolving stress field: insights from Discrete Element Models of fracture sealing. J. Geophys. Res. Solid Earth 119 (12), 8708–8727.

Waite, M.E., Ge, S.M., Spetzler, H., Bahr, D.B., 1998. The effect of surface geometry on fracture permeability: a case study using a sinusoidal fracture. Geophys. Res. Lett. 25 (6), 813–816.

Walsh, J.B., 1981. Effect of pore pressure and confining pressure on fracture permeability. Int. J. Rock Mech. Min. Sci. 18 (5), 429–435.

Walsh, J.B., Brace, W.F., 1984. The effect of pressure on porosity and the transport-properties of rock. J. Geophys. Res. 89 (NB11), 9425–9431.

Walsh, J.B., Brown, S.R., Durham, W.B., 1997. Effective medium theory with spatial correlation for flow in a fracture. J. Geophys. Res. Solid Earth Planets 102 (B10), 22587–22594.

Walsh, R., McDermott, C., Kolditz, O., 2008. Numerical modeling of stress-permeability coupling in rough fractures. Hydrogeol. J. 16 (4), 613–627.

Wang, L., Cardenas, M.B., 2016. Development of an empirical model relating permeability and specific stiffness for rough fractures and numerical deformation experiments. J. Geophys. Res. Solid Earth 121, 4977–4989.

Wang, L., Cardenas, M.B., 2018. Connecting pressure-saturation and relative permeability models to fracture properties: the case of capillary-dominated flow of supercritical CO2 and brine. Water Resour. Res. 54 (9), 6965–6982.

Wang, J.A., Park, H.D., 2002. Fluid permeability of sedimentary rocks in a complete stress-strain process. Eng. Geol. 63 (3-4), 291–300.

Wang, J.S.Y., Narasimhan, T.N., Scholz, C.H., 1988. Aperture correlation of a fractal fracture. J. Geophys. Res. Solid Earth Planets 93 (B3), 2216–2224.

Wang, L.C., Cardenas, M.B., Slottke, D.T., Ketcham, R.A., Sharp, J.M., 2015. Modification of the Local Cubic Law of fracture flow for weak inertia, tortuosity, and roughness. Water Resour. Res. 51 (4), 2064–2080.

Wang, M., Chen, Y.F., Ma, G.W., Zhou, J.Q., Zhou, C.B., 2016. Influence of surface roughness on nonlinear flow behaviors in 3D self-affine rough fractures: Lattice Boltzmann simulations. Adv. Water Resour. 96, 373–388.

Wang, C.S., Jiang, Y.J., Luan, H.J., Liu, J.K., Sugimoto, S., 2019. Experimental study on the shear-flow coupled behavior of tension fractures under constant normal stiffness boundary conditions. Processes 7 (2).

Watanabe, N., Hirano, N., Tsuchiya, N., 2008. Determination of aperture structure and fluid flow in a rock fracture by high-resolution numerical modeling on the basis of a flow-through experiment under confining pressure. Water Resour. Res. 44 (6).

Watanabe, N., Sakurai, K., Ishibashi, T., Ohsaki, Y., Tamagawa, T., Yagi, M., Tsuchiya, N., 2015. New *ν*-type relative permeability curves for two-phase flows through

subsurface fractures. Water Resour. Res. 51 (4), 2807–2824.

Wei, W., Xia, Y., 2017. Geometrical, fractal and hydraulic properties of fractured reservoirs: A mini-review. Adv. Geo-Energy Res. 1 (1), 31–38.

Wen, Z., Huang, G.H., Zhan, H.B., 2006. Non-Darcian flow in a single confined vertical fracture toward a well. J. Hydrol. 330 (3-4), 698–708.

Wendler, F., Okamoto, A., Blum, P., 2016. Phase-field modeling of epitaxial growth of polycrystalline quartz veins in hydrothermal experiments. Geofluids 16 (2), 211–230.

Wentinck, H.M., Busch, A., 2017. Modelling of CO2 diffusion and related poro-elastic effects in a smectite-rich cap rock above a reservoir used for CO2 storage. In: Rutter, E.H., Mecklenburgh, J., Taylor, K. (Eds.), Geomechanical and Petrophysical Properties of Mudrocks. Geological Society Special Publication, pp. 155–173.

Witherspoon, P.A., Wang, J.S.Y., Iwai, K., Gale, J.E., 1980. Validity of cubic law for fluid-flow in a deformable rock fracture. Water Resour. Res. 16 (6), 1016–1024.

Wollenweber, J., Alles, S.A., Kronimus, A., Busch, A., Stanjek, H., Krooss, B.M., 2009. Caprock and overburden processes in geological CO2 storage: an experimental study on sealing efficiency and mineral alterations. In: Gale, J., Herzog, H., Braitsch, J. (Eds.), Greenhouse Gas Control Technologies 9. Energy Procedia, pp. 3469–3476.

Wong, T.F., Fredrich, J.T., Gwanmesia, G.D., 1989. Crack aperture statistics and pore-space fractal geometry of Westerly granite and Rutland quartzite – implications for an elastic contact model of rock compressibility. J. Geophys. Res. Solid Earth Planets 94 (B8), 10267–10278.

Wu, H.Q., Pollard, D.D., 1995. An experimental-study of the relationship between joint spacing and layer thickness. J. Struct. Geol. 17 (6), 887–905.

Wu, W., Reece, J.S., Gensterblum, Y., Zoback, M.D., 2017. Permeability evolution of slowly slipping faults in shale reservoirs. Geophys. Res. Lett. 44 (22), 11,368–11,375.

Xiao, Y., Whitaker, F., Xu, T., Steefel, C., 2018. Reactive Transport Modeling: Applications in Subsurface Energy and Environmental Problems. Wiley.

Xie, L.Z., Gao, C., Ren, L., Li, C.B., 2015. Numerical investigation of geometrical and hydraulic properties in a single rock fracture during shear displacement with the Navier-Stokes equations. Environ. Earth Sci. 73 (11), 7061–7074.

Xiong, X.B., Li, B., Jiang, Y.J., Koyama, T., Zhang, C.H., 2011. Experimental and numerical study of the geometrical and hydraulic characteristics of a single rock fracture during shear. Int. J. Rock Mech. Min. Sci. 48 (8), 1292–1302.

Yan, Y.G., Koplik, J., 2008. Flow of power-law fluids in self-affine fracture channels. Phys. Rev. E 77 (3).

Yang, Z., Niemi, A., Fagerlund, F., Illangasekare, T., 2012. Effects of single-fracture aperture statistics on entrapment, dissolution and source depletion behavior of dense non-aqueous phase liquids. J. Contam. Hydrol. 133, 1–16.

Yang, Z., Niemi, A., Fagerlund, F., Illangasekare, T., 2013. Two-phase flow in rough-walled fractures: comparison of continuum and invasion-percolation models. Water Resour. Res. 49 (2), 993–1002.

Yang, Y.F., Liu, Z.H., Yao, J., Zhang, L., Ma, J.S., Hejazi, S.H., Luquot, L., Ngarta, T.D., 2018. Flow simulation of artificially induced microfractures using digital rock and Lattice Boltzmann methods. Energies 11 (8).

Yang, D.S., Wang, W., Li, K., Chen, W.Z., Yang, J.P., Wang, S.G., 2019a. Experimental investigation on the stress sensitivity of permeability in naturally fractured shale. Environ. Earth Sci. 78 (2).

Yang, Z., Méheust, Y., Neuweiler, I., Hu, R., Niemi, A., Chen, Y.F., 2019b. Modeling immiscible two-phase flow in rough fractures from capillary to viscous fingering. Water Resour. Res. 55 (3), 2033–2056.

Yasuhara, H., Kinoshita, N., Ohfuji, H., Lee, D.S., Nakashima, S., Kishida, K., 2011. Temporal alteration of fracture permeability in granite under hydrothermal conditions and its interpretation by coupled chemo-mechanical model. Appl. Geochem. 26 (12), 2074–2088.

Ye, Z., Liu, H.-H., Jiang, Q., Zhou, C., 2015. Two-phase flow properties of a horizontal fracture: The effect of aperture distribution. Adv. Water Resour. 76, 43–54. https://doi.org/10.1016/j.advwatres.2014.12.001.

Ye, Z., Liu, H.-H., Jiang, Q., Liu, Y., Cheng, A., 2017. Two-phase flow properties in aperture-based fractures under normal deformation conditions: Analytical approach and numerical simulation. J. Hydrol. 545, 72–87.

Yeo, I.W., Ge, S.M., 2001. Solute dispersion in rock, fractures by non-Darcian flow. Geophys. Res. Lett. 28 (20), 3983–3986.

Yeo, I.W., De Freitas, M.H., Zimmerman, R.W., 1998. Effect of shear displacement on the aperture and permeability of a rock fracture. Int. J. Rock Mech. Min. Sci. 35 (8), 1051–1070.

Yin, C., 2018. Test and analysis on the permeability of induced fractures in shale reservoirs. Nat. Gas Ind. B 5 (5), 513–522.

Yu, L., Liu, R., Jiang, Y., 2017. A review of critical conditions for the onset of nonlinear fluid flow in rock fractures. Geofluids 1–17.

Zeng, Z.W., Grigg, R., 2006. A criterion for non-Darcy flow in porous media. Transp. Porous Media 63 (1), 57–69.

Zhang, C.L., 2011. Experimental evidence for self-sealing of fractures in claystone. Phys. Chem. Earth 36 (17-18), 1972–1980.

Zhang, C.L., 2013. Sealing of fractures in claystone. J. Rock Mech. Geotech. Eng. 5, 214–220.

Zhang, J., Standifird, W.B., Roegiers, J.C., Zhang, Y., 2007. Stress-dependent fluid flow and permeability in fractured media: from lab experiments to engineering applications. Rock Mech. Rock. Eng. 40 (1), 3–21.

Zhang, M., de Jong, S.M., Spiers, C.J., Busch, A., Wentinck, H.M., 2018. Swelling stress development in confined smectite clays through exposure to CO2. Int. J. Greenh. Gas Control 74, 49–61.

Zhao, Z.H., Jing, L.R., Neretnieks, I., Moreno, L., 2011. Numerical modeling of stress effects on solute transport in fractured rocks. Comput. Geotech. 38 (2), 113–126.

Zhou, J.Q., Hu, S.H., Fang, S., Chen, Y.F., Zhou, C.B., 2015. Nonlinear flow behavior at low Reynolds numbers through rough-walled fractures subjected to normal compressive loading. Int. J. Rock Mech. Min. Sci. 80, 202–218.

Zhou, J.Q., Wang, M., Wang, L.C., Chen, Y.F., Zhou, C.B., 2018. Emergence of nonlinear laminar flow in fractures during shear. Rock Mech. Rock. Eng. 51 (11), 3635–3643.

Zimmerman, R.W., 2008. A simple model for coupling between the normal stiffness and the hydraulic transmissivity of a fracture. In: Proceedings of the 42nd US Rock Mechanics Symposium (ARMA), 08-314.

Zimmerman, R.W., Bodvarsson, G.S., 1996. Hydraulic conductivity of rock fractures. Transp. Porous Media 23 (1), 1–30.

Zimmerman, R.W., Yeo, I.W., 2000. Fluid Flow in Rock Fractures: From the Navier-Stokes Equations to the Cubic Law. Geophys. Monogr. Ser. 213–224.

Zimmerman, R.W., Chen, D.W., Long, J.C.S., Cook, N.G.W., 1990. Hydromechanical coupling between stress, stiffness, and hydraulic conductivity of rock joints and fractures. Rock Joints 571–577.

Zimmerman, R., Kumar, S., Bodvarsson, G., 1991. Lubrication theory analysis of the permeability of rough-walled fractures. In: International Journal of Rock Mechanics and Mining Sciences & Geomechanics Abstracts. Elsevier, pp. 325–331.

Zimmerman, R.W., Chen, D.W., Cook, N.G.W., 1992. The effect of contact area on the permeability of fractures. J. Hydrol. 139 (1-4), 79–96.

Zimmerman, R.W., Al-Yaarubi, A., Pain, C.C., Grattoni, C.A., 2004. Non-linear regimes of fluid flow in rock fractures. Int. J. Rock Mech. Min. Sci. 41 (3) 384.

Zoback, M.D., 2010. Reservoir Geomechanics. Cambridge University Press.

Zou, L.C., Jing, L.R., Cvetkovic, V., 2015. Roughness decomposition and nonlinear fluid flow in a single rock fracture. Int. J. Rock Mech. Min. Sci. 75, 102–118.